GRAPHENE ON NON-POLAR SIC FACETS

A Thesis
Presented to
The Academic Faculty

By

Yiran Hu

In Partial Fulfillment
of the Requirements for the Degree
Doctor of Philosophy in the
School of Physics

Georgia Institute of Technology

August 2020

GRAPHENE ON NON-POLAR SIC FACETS

Approved by:

Dr. Walter de Heer, Advisor
School of Physics
Georgia Institute of Technology

Dr. Zhigang Jiang
School of Physics
Georgia Institute of Technology

Dr. Markus Kindermann
School of Physics
Georgia Institute of Technology

Dr. Phillip N. First
School of Physics
Georgia Institute of Technology

Dr. Bernard Kippelen
School of Electrical and Computer Engineering
Georgia Institute of Technology

Date Approved: May 8, 2020

格物致知。

(Study the nature and acquire knowledge.)

The Great Learning, Book of Rites

To my parents.

ACKNOWLEDGEMENTS

I want to thank Dr. Walt de Heer for his guidance throughout the years of my graduate study. Dr. Claire Berger has been a tremendous help for my research as well as for me to fit in here in the US!

Thanks to my thesis committee, Dr. Zhigang Jiang, Dr. Markus Kindermann, Dr. Phillip First and Dr. Bernard Kippelen. Dr. Jiang and Dr. First have been very kind in helping us with the experiments and with great discussions.

Thanks to my lab mates, Dr. Vladimir Prudkovskiy, Yue Hu, Grant Nunn, Dr. Dogukan Deniz, Dr. Jean-Philippe Turmaud, Dr. James Gigliotti, Dr. John Hankinson, Xiaoyun Yang and John Indergaard. Thanks to my colleagues in the condensed matter community at GT, Dr. Xiaojian Bai, Jeremy Yang, Dr. Luwei Ge, Marcus Daum, Jason Dark, Tianhao Zhao, Dr. Martin Mourigal, Dr. Zhiling Dun, Dr. Owen Vail, Dr. Yuxuan Jiang, Dr. Hsin-Ju Wu, Dr. Di Chen, Harshavardhan Murali, Dr. Anna Miettinen, Dr. Matthew Conrad, Dr. Meredith Nevius and Dr. Kartik Kothari. I also want to thank my friends at GT, Dr. Dai Tang, Caleb Anderson, Bryan Pflueger, Dr. Shane Jacobeen, Dr. Yu-Hui Lin, Chujie Chen.

I want to also thank our collaborators at TICNN, Dr. Lei Ma, Kaimin Zhang, Peixuan Ji, Jian Zhao, Chenqian Shi. And thanks to the staff at IEN at GT, Dr. Hang Chen, Eric Woods, Devin Brown, Tran-Vinh Nguyen, Charlie Suh and Dr. Mikkel Thomas.

My friends Dr. Jingwei Liu, Ann Carter McDonald, Dr. Allen McDonald and Vlad Hrybok have offered great help throughout my life in the US.

Finally, great thanks to my parents, Qing Chen and Zhuomin Hu and my family for their support in my life!

TABLE OF CONTENTS

LIST OF TABLES

LIST OF FIGURES

LIST OF SYMBOLS AND ABBREVIATIONS

E_F	Fermi energy
AC	Armchair
aC	Amorphous carbon
AFM	Atomic force microscope
ALD	Atomic layer deposition
ARPES	Angle-resolved photoemission spectroscopy
BLG	Bilayer graphene
CCS	Confinement controlled sublimation
CMP	Chemical-mechanical polishing
CNP	Charge neutrality point
CNT	Carbon nanotube
CVD	Chemical vapor deposition
DOS	Density of states
EBE	Electron beam evaporator
EBL	Electron beam lithography
EFM	Electrostatic force microscope

EG	Epitaxial graphene
Epigraphene	Epitaxial graphene
FFM	Friction force microscope
FTF	Face-to-face
FWHM	Full width at half maximum
GNR	Graphene nanoribbon
GT	Georgia Tech
HOPG	Highly oriented pyrolytic graphite
HRTEM	High-resolution transmission electron microscopy
ICP	Inductively coupled plasma
IR	Infrared
LEED	Low energy electron diffraction
LFM	Lateral force microscope
MLG	Multilayer graphene
MR	Magnetoresistance
PID	Proportional–integral–derivative
PSPD	Position sensitive photo detector
PVD	Physical vapor deposition
qC	Quantum capacitance
RIE	Reative ion etching

RMS	Root mean squared
SEM	Scanning electron microscope
SLG	Single layer graphene
SPM	Scanning probe microscope
STM	Scanning tunneling microscope
STS	Scanning tunneling spectroscopy
SW-GNR	Sidewall graphene nanoribbon
TEM	Transmission electron microscope
TICNN	Tianjin International Center for Nanoparticles and Nanosystems
WAL	Weak antilocalization
WL	Weak localization
XPS	X-ray photoelectron spectroscopy
ZZ	Zigzag

SUMMARY

Graphene nanoribbons (SW-GNR) grown on sidewall SiC substrate facets exhibit exceptional quantized ballistic transport over $15\,\mu\mathrm{m}$ even at room temperature. For micron long ribbons, transport in these charge neutral ribbons involves a single conducting channel with a conductance of e^2/h, which to this day is not fully understood. We have therefore studied here graphene grown on SiC full wafers cut along the same crystallographic orientation as the sidewall facets. We characterize graphene growth on these non conventional (non-polar) faces and identify preferred orientation and the presence of an interface layer. Transport measurements of Hall-bar patterned graphene devices shows strong similarities with that of SW-GNR ribbons. In particular an analysis in terms of edge and bulk electronic states reveal a ballistic edge state conduction, with mean free path larger than $10\,\mu\mathrm{m}$, and a bulk conduction with a $\sim 10\,\mathrm{nm}$ mean free path. Segment quantization is also discussed. The findings in this thesis point to a new route towards future large scale high-performance electronics.

CHAPTER 1
INTRODUCTION

In 1965 Gordon Moore observed that the density of transistors in an integrated circuit was doubling roughly every two years, which has been dubbed the Moore's law [2] (Figure 1.1). As chip manufacturers today are approaching 5 nm node mass production [3], major challenges arise notably concerning heat power density. Thus, new technologies are keenly sought after to succeed the silicon technology. Ideally, the new technology provides entirely new paradigm of operation and thus can perform orders of magnitude better than silicon while leveraging the existing silicon chip fabrication technologies.

Epitaxial graphene (epigraphene) emerges as a suitable candidate for this purpose. It has exceptional electronic properties [4], and has shown great potentials for electronics [5, 6, 7, 8] as well as spintronics [9, 10]. It grows epitaxially on SiC single crystal and can be patterned and processed using conventional microelectronic fabrication techniques without being transferred to another substrate.

This thesis explores the growth, characterization and transport measurements on epigraphene grown on non-polar SiC facets. This research is the continuation of the exciting development of researches on the sidewall graphene nanoribbon on SiC [11, 12, 13, 4, 14, 15]. The findings here shines light on a new route towards the holy grail of graphene electronics research: high performance electronics with coherent ballistic transport.

1.1 Graphene

Graphene is a single sheet of carbon atoms arranged in a honeycomb lattice (Figure 1.2**a**). It's the building block of various carbon materials, including graphite that is graphene films stacked together according to the Bernal stacking order, and carbon nanotubes (CNT).

The honeycomb lattice structure is shown in Figure 1.2**b**. It's a triangular lattice with

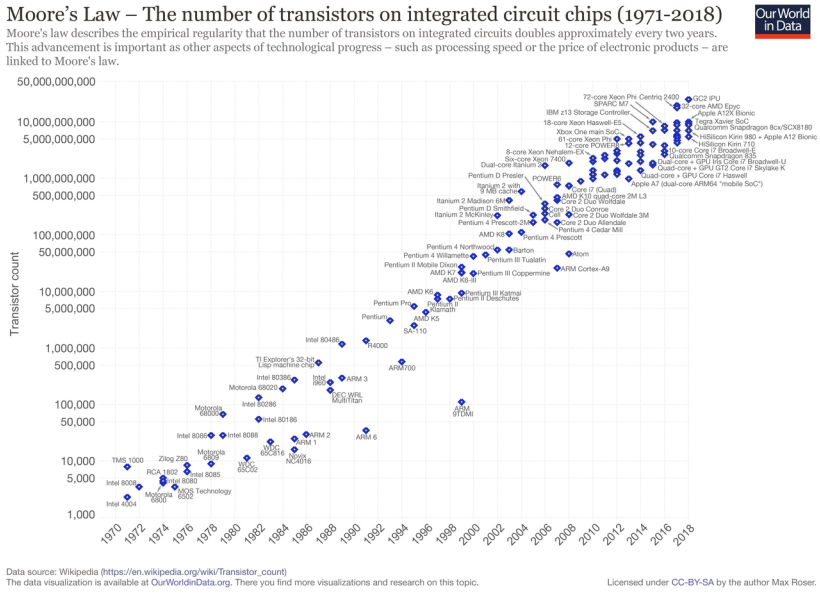

Figure 1.1: Transistor counts per chip vs. time. From Ref. [1].

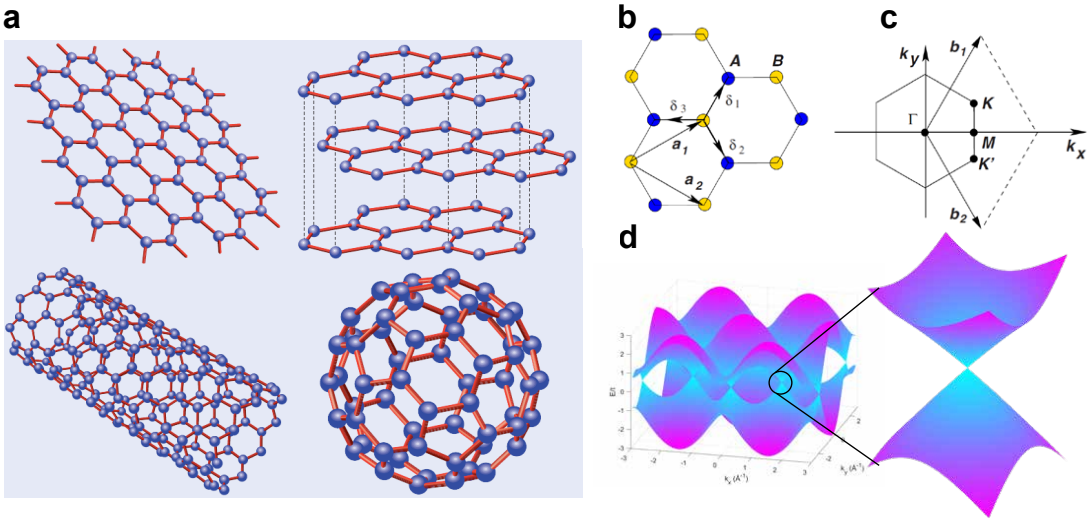

Figure 1.2: **a**, Various forms of carbon structures derived from graphene. From Ref. [16]. **b**, The crystal structure of graphene and **c**, The reciprocal space of graphene. **b** and **c** from Ref. [17]. **d**, The π bands of graphene. The band exhibits linear relationship with the wave vector near the K and K' points which are dubbed Dirac cones for it resembles the behavior a massless Dirac fermion.

two atoms in a unit cell, labeled "A" and "B". Figure 1.2**c** shows the reciprocal lattice of the triangular lattice and the first Brillouin zone is marked out by the hexagon. The high symmetry points K and K' are the corners of the first Brillouin zone. Note that each of these two points represent three identical points rotated about the Γ point by 120°. Thus both represent all the six corners of the hexagon.

A carbon atom has four outer shell electrons, s and p orbitals each hosting two. As is shown in Figure 1.2**b**, each carbon atom has three neighbors which take three of these electrons to form the σ (sp^2-sp^2) bonds. The σ bond in graphene is very strong, making graphene one of the strongest materials that we know. The other one electron forms a π bond with the neighbors giving rise to the π bands which are responsible for the electronic properties of graphene. The honeycomb lattice structure results in a special band structure, which can be derived from a remarkably simple tight binding approximation with the consideration of the p_z orbitals from the two atoms in a unit cell [18]. The resulting energy dispersion relation is

$$E_{\pm}(k) = \pm t\sqrt{3 + 2\cos \boldsymbol{k}\cdot\boldsymbol{a}_1 + 2\cos \boldsymbol{k}\cdot\boldsymbol{a}_2 + 2\cos \boldsymbol{k}\cdot\boldsymbol{a}_3}, \tag{1.1}$$

where $t \approx 2.8\,\mathrm{eV}$ is the nearest neighbor hopping term, $\boldsymbol{a}_1$ and $\boldsymbol{a}_2$ are as labeled in Figure 1.2**b** and $\boldsymbol{a}_3 = \boldsymbol{a}_1 - \boldsymbol{a}_2$. The resulting band structure is shown in the (k_x, k_y, E) plot of Figure 1.2**d**.

Eq. 1.1 can be expanded near the K and K' points. Here we expand it near the K point for example

$$E_{\pm}(\boldsymbol{q}) = \pm\hbar c^* |\boldsymbol{q}|, \tag{1.2}$$

where $c^* = \frac{\sqrt{3}at}{2\hbar} \sim 10^6\,\mathrm{m/s}$ is the electronic velocity, a is the lattice constant, and $\boldsymbol{q} = \boldsymbol{k} - \boldsymbol{K}$ is the wave vector measured from the K or K' point. As we can see, the energy is linear with respect to the momentum, forming two cone shaped bands, which is referred to as the Dirac cones as this linear dispersion relation can be described by the

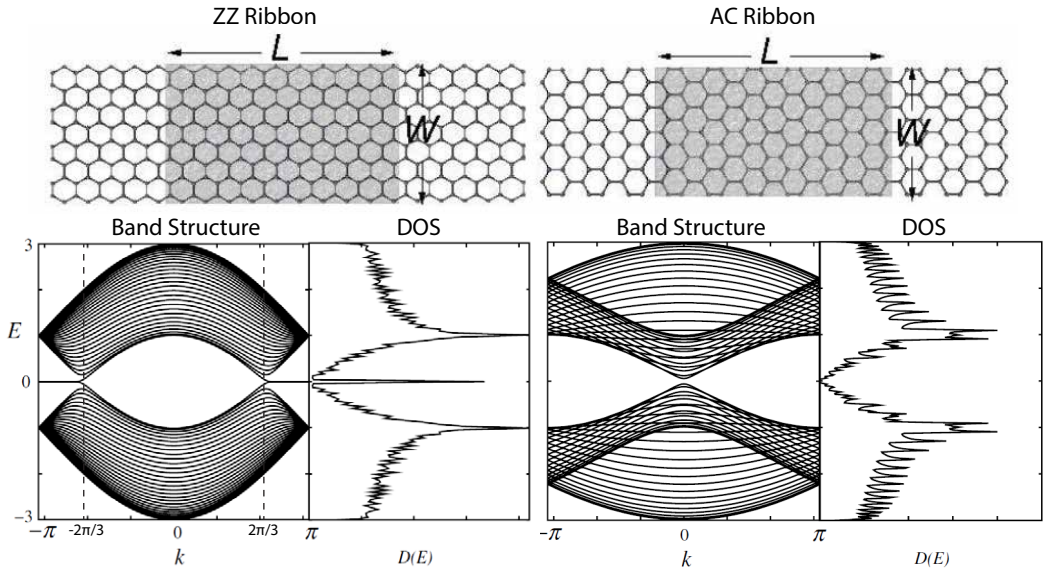

Figure 1.3: Left: Diagram of the ZZ edge, its band structure and DOS. Right: Diagram of the AC edge, its band structure and DOS. k is measured in the unit of $1/a$ where a is the lattice constant. Note that in the ZZ band structure, the $k = \pm 2\pi/3$ points correspond to the K and K' points in the 2D graphene. Edge diagram from Ref. [19]. Band structure and DOS from Ref. [20].

massless Dirac equation. When graphene is charge neutral, the Fermi energy is at the tip of the Dirac cones called the Dirac points or charge neutrality point (CNP). Thus, low energy (low temperature, low bias voltage etc.) electron behavior in a charge neutral graphene result from the energy band near the Dirac points. A number of novel phenomena have been predicted and observed near these Dirac points, including Klein tunneling, anomalous integer quantum Hall effect, etc [17]. These properties, mostly shared with carbon nanotubes have inspired a lot of researches into the possibility of graphene electronics.

Graphene nanoribbons (GNR's) have been a main research focus of graphene electronics engineering, as the width and edge of the nanoribbons can in principle be engineered to achieve various electronic band properties. The two main types of GNR edge are called the zigzag (ZZ) edge and the armchair (AC) edge (Figure 1.3). Notably, a flat band is predicted by tight-binding calculations at the CNP of the ZZ ribbon between $k = \pm 2\pi/3a$ and $k = \pm\pi/a$, which produces a high density of states at the CNP. Note that $k = \pm 2\pi/3a$ points correspond to the K/K' points of the reciprocal space of 2D graphene. The states associated with the flat band are localized near the physical edge of the ZZ ribbon. The

band continues at higher energy, as k moves away from the $\pm 2\pi/3a$ points towards 0, with a linear dispersion of the same velocity as 2D graphene. These ZZ edge states are predicted to exist for any GNR that does not have a perfect AC edge [21].

1.1.1 Graphene Production Methods

Various ways have been investigated for graphene production. Individual graphene sheets can be peeled off (exfoliated) from highly-oriented pyrolytic graphite (HOPG) using Scotch tape [22]. This method is only useful in a laboratory setting. Beside, any transfer of graphene sheets is plagued with problems such as tear, wrinkles, bubbles and various impurities trapped at the substrate/graphene interfaces [23]. Chemical vapor deposition is also used to grow graphene [24]. Usually a metal substrate (e.g. Cu) is used. The resulting film has to be transferred onto an insulating substrate for electronic applications.

Epigraphene on SiC wafers, however, is a very promising method of graphene production [25]. The silicon atoms above SiC surface have higher vapor pressure than carbon, and under a temperature above $\sim 1300\,^{\circ}$C in vacuum, silicon atoms start to sublime, leaving an excess of carbon atoms on the surface, self-arranged into graphene lattice (Figure 1.5).

1.2 Epigraphene on SiC

Epitaxial graphene (epigraphene) on SiC is a very scalable and industry-relevant graphene production method for nanoelectronics [25].

Thin graphite had been long known to form atop single-crystalline SiC surface upon annealing at high temperature [26], but not until 2004 did researchers start to try to investigate the possibility of utilizing this technique for graphene nanoelectronics [27]. Large progresses have since ensued. To date, various methods have been exploited in order to achieve high quality uniform growth [25, 28, 29].

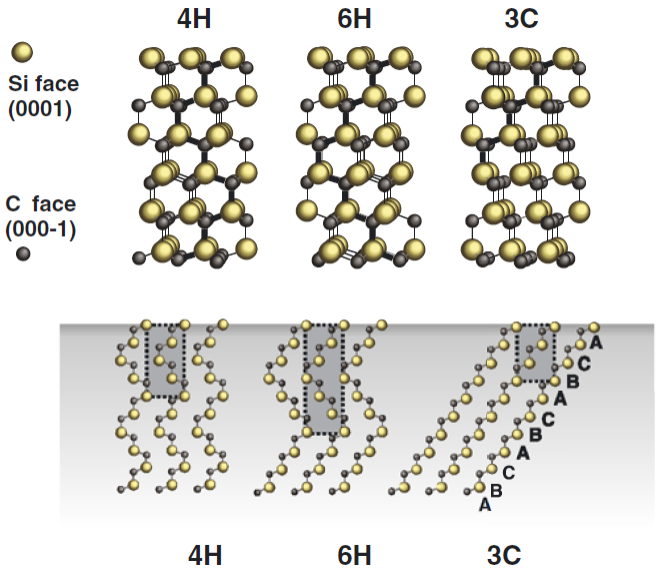

Figure 1.4: Polytypes of SiC. From Ref. [30].

1.2.1 Silicon Carbide

Silicon carbide (SiC) comes in many polytypes, the common ones being 4H (hexagonal), 6H (hexagonal), and 3C (zinc-blende). The building block of the SiC crystals is a flat bilayer of superposed Si and C atoms. As shown in Figure 1.4, the numbers in these polytype names indicate the periodicity of SiC bilayers. The SiC has two major facets called the Si (0001) face and the C $(000\bar{1})$ face as they are terminated by either Si or C atoms alone.

4H- and 6H-SiC are used in this thesis work. An spontaneous polarization exists in these polytypes, perpendicular to the Si- and C-faces. Thus, they are called polar faces. As a result of this, free standing graphene (H_2 intercalated buffer layer) on the Si-face is p-doped while the first graphene layer on top of the buffer layer is n-doped [31].

This thesis studies the non-polar facets of SiC, i.e. the facets that are not cut in these two main directions.

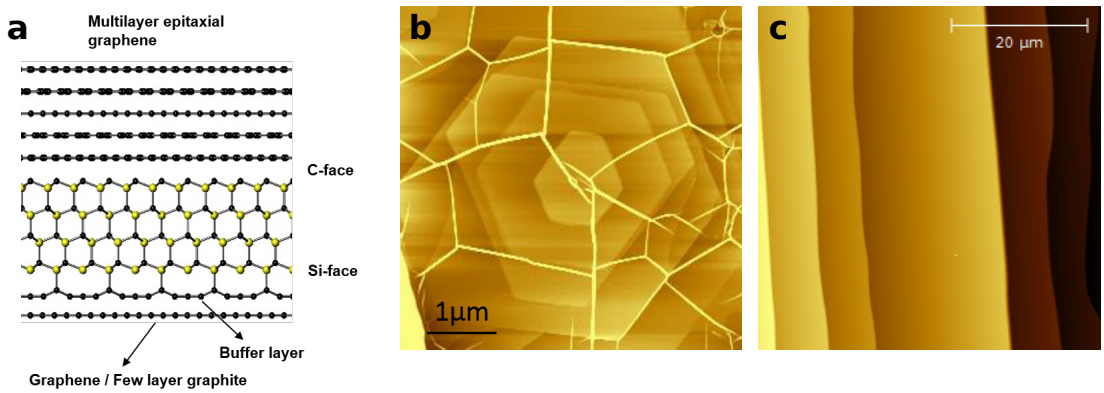

Figure 1.5: a, Schematics showing the hexagonal SiC crystal structure and the graphene growth on the two polar faces. The graphene grown on Si- and C-faces of SiC differs in their bonding with the substrate. **b**, The graphene grown on the C-face of SiC bonds weakly with the substrate. Pleats can be seen that formed during the cooling down due to different thermal expansion coefficient to release the strain. From [33]. **c**, Unlike on the C-face, the graphene grown on the Si-face bonds to the substrate and becomes an insulator, called the buffer layer. The second layer on top of that retains graphene's electronic properties but is still strained due to the influence of the substrate.

1.2.2 Epigraphene

The properties of graphene grown on SiC depends on the crystal face. It was known from the very early days of epigraphene research that the graphene properties on the so-called Si-face, ie. SiC(0001) and C-face, ie. SiC$(000\bar{1})$ differ a lot (Figure 1.5**a**) [25, 32].

The first graphene layer bonds to the Si-face, affecting the electronic properties of this layer. This layer is called the "buffer" layer since it's the first layer next to the substrate. Although the details of buffer layer's properties are still under investigation, in general, it is not conductive [34], showing a band gap [35, 36]. The second layer of graphene on Si-face is much less affected by the substrate. It is negatively charged to about $450\,\mathrm{meV}$ due to the influence of the substrate and buffer layer [31]. By controlling the growth, a single graphene layer (with the buffer layer underneath) covers the entire SiC substrates (with some bilayer islands) [25, 28]. In this case, the buffer layer doesn't contribute to the conduction, and the system behaves like a single graphene layer, showing the anomalous quantum Hall effect indicating a Berry's phase of π [37, 38]. Thus this "graphene plus buffer layer" system is referred to as "Si-face single layer graphene" (SLG) in the scope

of this thesis. Note that some literature refers to this system as "double layer" or "bilayer" graphene because it consists of two layers though in fact electronically it behaves just like a single layer. Further growth leads to more layers to form. The stacking order is Bernal stacking. Si-face graphene is notable for its relatively uniform growth on atomically flat terraces, with some residual bilayers at step edges as shown in Figure 1.5**c** [25, 28]. In recent years, progress has been made towards wafer scale growth of homogeneous graphene using polymer assisted growth [39]. Its applications in quantum resistance standard [38] and high frequency transistors [6] demonstrate its great promise.

On the C-face, graphene doesn't bond to the substrate. The resulting form of graphene retains a lot of its pristine nature and high mobility can be achieved at low charge density [40, 41]. A lot of interesting studies have been done on this surface, exploiting the high quality of graphene. Notably, high frequency field effect transistor has been realized [5], and high-quality lateral spin channel has been demonstrated [42, 9, 43] using multilayer graphene on this face as a spin channel. However, the growth rate on this face is fast and hard to control, and experiments on single layer graphene (SLG) can only be done on small patches of graphene on this surface, which is quite limiting when it comes to mass production. On the other hand, the graphene layers stack alternatively with roughly $0 - 30^\circ$ rotations. This rotational stacking preserves the graphene electronic structure in each graphene layer (explicitly not graphite). This protects the integrity of the graphene layers in the middle of the stack, that are charge neutral($< 5 \times 10^9\,\mathrm{cm}^{-2}$), have high mobility ($\sim 10^6\,\mathrm{cm}^2/\mathrm{V\,s}$), and are very much sought for optical measurements of multi layer graphene [44, 45, 46].

As noted earlier, epigraphene is probably the only form of graphene that is both high-quality and suitable for industrial production. It is consistent with existing microelectronics fabrication technologies. All these advantages make it the most likely candidate to succeed silicon.

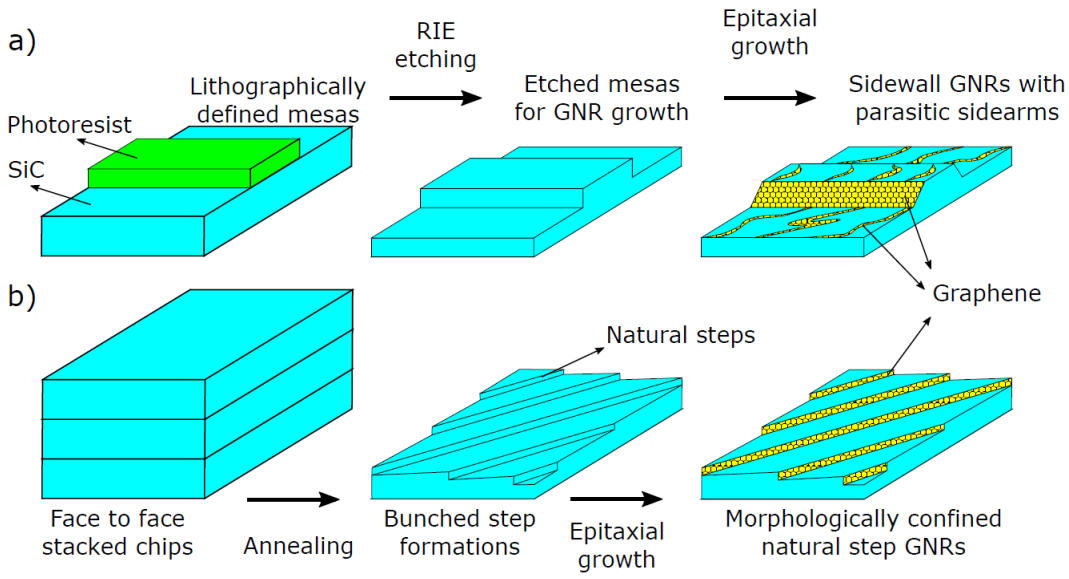

Figure 1.6: An illustration of the growth of SW-GNR's and the resulting morphology depending on the various initial surface conditions. **a**, The sample is pre-patterned with etched trenches. During the growth the trench edges and natural steps cross over each other forming a complex network of GNR's. **b**, A sample without pre-patterned trenches develop natural steps due to the wafer miscut. **a** and **b** from Ref. [15].

1.2.3 Sidewall Graphene Nanoribbons

One very promising form of graphene found in the epigraphene research is the sidewall graphene nanoribbons (SW-GNR). As shown in Figure 1.6 graphene growth starts at step edges on the Si-face. If the growth condition is controlled to confine the growth on only those step edges, GNR's are formed. As the surface of SiC Si-face usually has a miscut angle (i.e. not perfectly in the (0001) direction), steps form on the surface running perpendicular to the miscut direction and graphene grows on these steps (Figure 1.6**b**). We call these natural steps. We can also pre-pattern the steps. Trenches are etched using reactive ion etching (RIE), usually around 20 nm deep. Graphene is grown on these pre-patterned trench edges. Remarkably, the epitaxial nature of the growth is preserved on SW-GNR's, meaning that the graphene crystal orientation is the same as on Si face. Thus, edge type (AC vs. ZZ or in between) can be controlled by the step direction, as illustrated in Figure 1.7. Angle-resolved photoemission spectroscopy (ARPES) studies have been done on these pre-patterned SW-GNR's and revealed the Dirac cone of graphene (Figure 1.8**a**) and

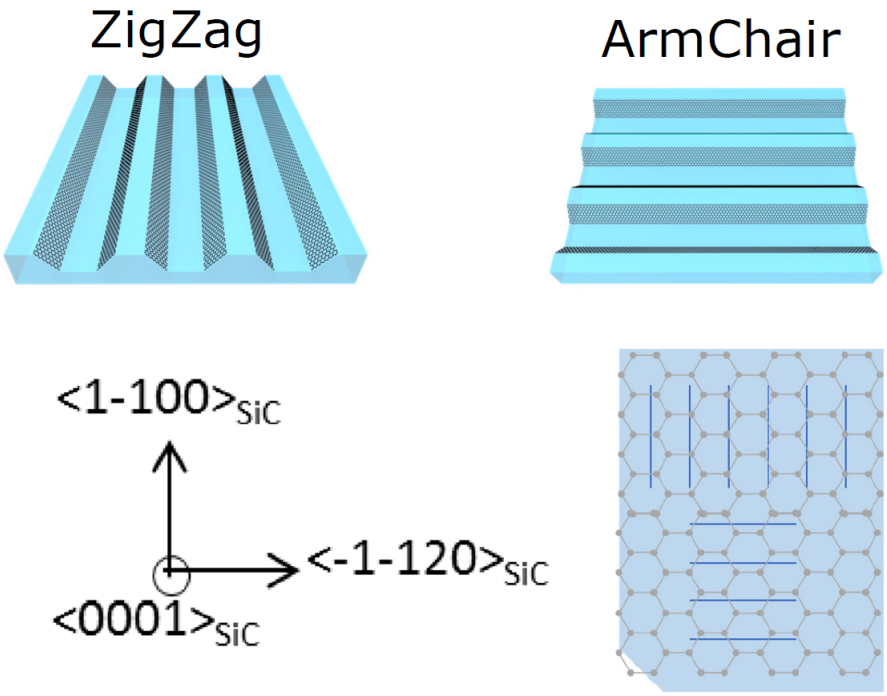

Figure 1.7: Because the SW-GNR growth is epitaxial, it is possible to control the ribbon edge type by etching trenches along either the SiC $\langle 1\bar{1}00\rangle$ or the $\langle 11\bar{2}0\rangle$ direction. From Ref. [15].

showed indication of the flat band of ZZ GNR's [50]. It also indicates that the SW-GNR is charge-neutral, which can be corroborated with STM studies [4, 51].

SW-GNR's come in various forms. They differ from each other in the edge orientation, the specific facet they grow on, the edge termination as well as the underlying SiC poly-type. Various flavors of the SW-GNR's previously investigated are shown in Figure 1.8**b**-**h**. Multiple facets were found in previous studies and a brief summary is provided in Table 1.1.

1.2.4 Ballistic Transport in SW-GNR

The strongest motivation for the work in this thesis is the exciting transport phenomena found in the SW-GNR's [13, 12, 14]. Ruan et al and Baringhaus et al reported on the exceptional ballistic SW-GNRs on SiC (Figure 1.10) [13, 4]. More specifically, the electronic transport was characteristic of a *single-channel* ballistic conductor, with conductance of e^2/h. Let's review the theory of quantum conductance briefly.

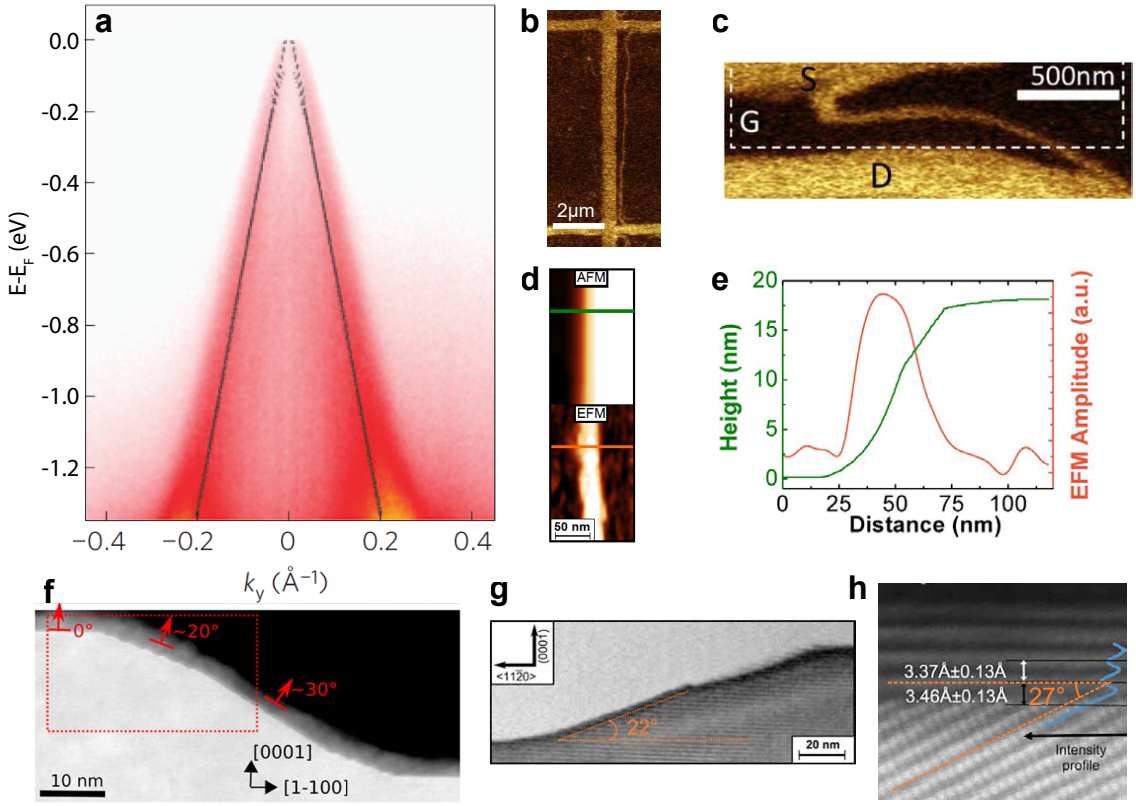

Figure 1.8: **a**, ARPES shows a clear Dirac cone for the SW-GNR in the AC direction. Note that the Fermi level is at the Dirac point. From Ref. [47]. **b**, EFM image showing a straight SW-GNR. **c**. EFM image showing a meandering SW-GNR. **b** and **c** from Ref. [13]. **d**, AFM and EFM images of an SW-GNR and **e** the corresponding profiles. The topography profile indicates two distinctive facets. **f**, **g** and **h**, HRTEM images show three different facet angles reported by three different groups. **d**,**f** and **g** from Ref. [14]. **e** from Ref. [48]. **h** from Ref. [49].

Table 1.1: Table of sidewall facet angles reported by various groups using different tools. (*Unpublished result from sample AGYHA2.)

Facet	SiC Polytype	Group	Microscopy Method	Facet Angle	Reference
$(1\bar{1}0n)$	4H	de Heer	TEM	24°	[11]
		de Heer	AFM	24°	*AGYHA2**
		Conrad & de Heer	TEM	28-30°	[48]
		First	STM	29-32°	[51]
	6H	First	STM	11-22°	[51]
$(11\bar{2}n)$	4H	de Heer	AFM	24-26°	*AGYHA2*
	6H	Tegenkamp	TEM	22°	[52]

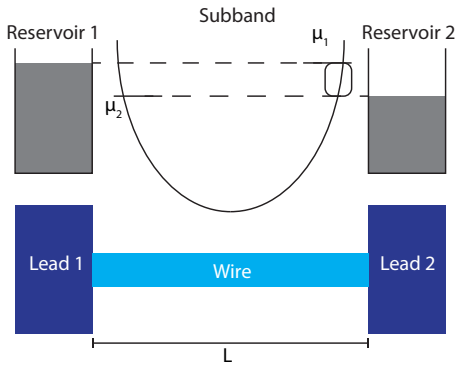

Figure 1.9: A diagram illustrating the electron transport through transmission from one lead to another through the 1D channel. The current is carried by the electronic states in the boxed region between μ_2 and μ_1 on the right side, as the states below μ_2 have equal amount of left and right moving current and cancel each other out. Adapted from [53].

The transport in a 1D mesoscopic system can be characterized by a simple band structure consideration [53]. Let's consider a 1D wire connected to two electron reservoirs on each side whose quasi-Fermi energies are μ_1 and μ_2, respectively (Figure 1.9). Let's also assume that $T = 0\,\mathrm{K}$, and $|\mu_1 - \mu_2| \ll E_F$, where the Fermi level E_F is measured with respect to the conduction band bottom. The current from reservoir 1 to 2 is carried by the electron states on the right side of the band between μ_2 and μ_1, assuming that $\mu_1 > \mu_2$ (Figure 1.9). The velocity of these electrons is proportional to the derivative of the energy band $v = \frac{1}{\hbar}\frac{\mathrm{d}E}{\mathrm{d}k}$. The time for one electron to travel a distance L ballistically from one side to the other is L/v and contribute ev/L to the current. Thus we have

$$\begin{aligned} I &= \frac{e}{L}\int_{k_{\mu_2}}^{k_{\mu_1}} \frac{1}{\hbar}\frac{\mathrm{d}E}{\mathrm{d}k}\frac{g_s g_v L}{2\pi}\mathrm{d}k \\ &= \frac{g_s g_v e}{h}\int_{\mu_2}^{\mu_1}\mathrm{d}E \\ &= \frac{g_s g_v e}{h}(\mu_1 - \mu_2) \\ &= \frac{g_s g_v e^2}{h}V \\ &= g_s g_v G_0 V, \end{aligned} \tag{1.3}$$

where g_s and g_v are the spin and valley degeneracies and we made use of the fact that

$eV = (\mu_1 - \mu_2)$. The quantum conductance $G_0 = e^2/h = (25.8\,\mathrm{k\Omega})^{-1}$. Now let's consider multiple bands. The ith band contributes a current $T_i g_{v,i} g_{s,i} \frac{e^2}{h}$ where T_i is the transmission probability. The total conductance is

$$G = \sum_i T_i g_{v,i} g_{s,i} \frac{e^2}{h}. \tag{1.4}$$

The transmission probability is a function of length of the channel L and the mean free path L_0 of the channel:

$$T = (1 + L/L_0)^{-1}. \tag{1.5}$$

We have two extreme cases: the diffusive regime ($L_0 \ll L$), and the ballistic regime ($L_0 \gg L$).

$$T \approx \begin{cases} 1 & L_0 \gg L \\ L_0/L & L_0 \ll L \end{cases}. \tag{1.6}$$

Note that in the diffusive regime, the resistance $R = G^{-1} \propto L/L_0$. Also, the number of subbands below the Fermi level is proportional to the width of the channel $M \propto W$. Thus, in a macroscopic 2D sample ($L \gg L_0$ and $W \gg \hbar c^* \pi / E_F$ for graphene), the Landauer's formula (Eq. 1.4) recovers to the classical case. On the other hand, in the ballistic regime, the conductance has a weak dependence on the distance. The resistance of a single ballistic channel is

$$R = 1/G = \frac{1}{T g_s g_v} \frac{h}{e^2} = (1 + L/L_0) \frac{1}{g_s g_v} \frac{h}{e^2}. \tag{1.7}$$

This equation has two implications: (1), the R vs. L measurement extrapolates to $\frac{1}{g_s g_v} h/e^2$ at $L = 0$; (2), the slope is $\frac{1}{g_s g_v L} h/e^2$, from which we can estimate the mean free path.

Figure 1.10**a** shows several R vs. L measurements on SW-GNR's performed in a multi-probe station equipped with four nanoscopically sharp tungsten probes [4]. All the plots extrapolate to h/e^2, indicating a single channel with spin and valley degeneracies both as 1. The virtually flat R vs. L plot in the case of line 5 in Figure 1.10**a** indicates an exceptionally

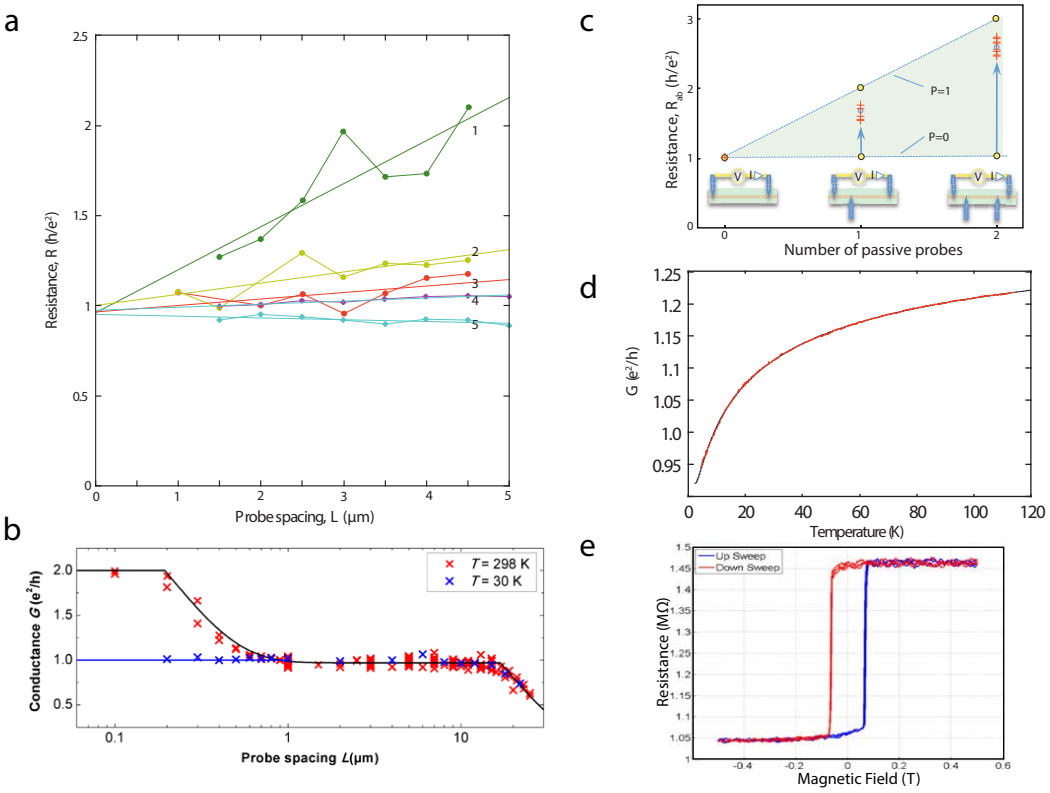

Figure 1.10: **a**, The distance dependent resistance measurement showing an essentially constant resistance value independent of the distance. **b**, Non-linear conductance decrease at critical lengths. Note that at a higher temperature, a second mode opens up below $1\,\mu\mathrm{m}$ distance. **c**, Invasive probes introduce scattering centers and increase the resistance by $\sim h/e^2$ per each probe. The crosses are measured data. The yellow filled dots are theoretical resistance values for ideal invasive ($P = 1$) and non-invasive ($P = 0$) probes. **d**, Conductance of an SW-GNR with respect to temperature. **a**-**d** from Ref. [4]. **e**, The tunnel magnetoresistance of between an SW-GNR and a cobalt contact of 38%, indicating magnetization of the SW-GNR itself. From Ref. [10].

long mean free path, while lines 1 through 4's slopes correspond to mean free paths of 4.2, 28, 16, and 58 μm, respectively.

According to Landauer's formula, in a ballistic 1D wire, a scattering center with transmission probability T_s increases the resistance by [53]

$$\Delta R = \frac{(1-T_s)}{T_s}\frac{1}{g_s g_v}\frac{h}{e^2}. \tag{1.8}$$

Thus, we expect to see the resistance of a wire increase by $\sim h/e^2$ for each invasive probe that is inserted in between the 2 measuring probes. As shown in Figure 1.10**c**, this phenomenon was also observed in SW-GNR's [4].

The total degeneracy of 1 is not expected. The ZZ-edge GNR's 0th band has a valley degeneracy of 1 while the higher bands have 2 (Figure 1.3). The spin degeneracy of 2 is not observed. It indicates that the spin degeneracy must have been lifted, so that the 0th band splits into 2 bands and only one contributes.

The temperature dependent measurements in [4] brings more interesting insights. Firstly, Figure 1.10**b** shows the length dependent conductance measurements at two different temperatures. The resistance values for the two temperatures are similar above 1 μm. However, they deviate from each other at below 1 μm, as the conductance at 30 K rises to $2e^2/h$ at about 200 nm. Fixed length ribbons were also measured and temperature dependent conductance is shown in Figure 1.10**d**. The conductance rises with respect to temperature. These observation implies that the spin degeneracy is lifted into two and forms two conduction channels. One of them is relatively stable and persists at relatively long length at low temperature. The other channel seems to be thermally activated and decays as the length increases.

The data in Figure 1.10**d** can be fitted with

$$G(T) = \alpha\frac{e^2}{h}\left(1 + 0.5\exp\left[-\left(T^*/(T-T_0)\right)^{1/2}\right]\right), \tag{1.9}$$

where $\alpha = 0.922$, $T^* = 21.5\,\mathrm{K}$, and $T_0 = 2.2\,\mathrm{K}$. This model is based on a conduction channel with constant conductance $\sim e^2/h$ with respect to temperature plus a thermally activated conductance. The characteristic activation temperature is inversely proportional the ribbon length [4]. This implies that the activation might be related to the longitudinal states in the SW-GNR.

The theoretical work by Li et al suggests the existence of a majority-spin channel with a micrometer-long mean free path and several minority-spin channels with very short mean free paths down to 1 nm in a GNR [54]. The spin switch study by Hankinson (Figure 1.10**e**) also indicates that the current in the SW-GNR spin-polarized [10]. Both these findings corroborate the speculation of the spin-dependent transport channels in SW-GNR's.

1.3 Motivation

The long mean free path at room temperature and the degeneracy lifting pose questions regarding the nature of the transport in SW-GNR's that are both interesting from a physics standpoint and relevant to application in nanoelectronics. The non-polar facet substrate on which SW-GNR's reside could play a very important role. In order to understand this single-channel transport, more information is needed about the influence of the non-polar crystal facet on the graphene. Indeed, at this moment, very little is known concerning this graphene system. On one hand, there seems to be no consensus on exactly which facet the ballistic ribbons reside on. There are studies that report various ribbon facets. In Table 1.1, I listed a few reported facet angles that graphene grows on by various groups. Notably, even on a single sidewall, there is not necessarily only one facet orientation. For example, in Figure 1.8**e**, the topography profile clearly shows a sidewall that's composed of two different facets. Some evidence seems to indicate that the ballistic transport doesn't necessarily depend on a certain facet. Indeed, it occurs even on a meandering ribbon (Figure 1.8**c**) [4].

Due to the limited width of the nanoribbons, it is very hard to apply surface science

tools, e.g. ARPES, on them. In one ARPES study, for example, very dense arrays of trenches had to be etched and SW-GNRs were grown on them in order to accumulate sufficient material for a large enough signal [47].

Also, SW-GNR's are 1D structures that cannot be patterned into networks of electronic devices. This limits the application potential of them. On the other hand, 2D graphene grown on large non-polar facets can be patterned and still retains the same electronic properties as SW-GNR's.

Thus, the idea of growing large area of graphene on these facets was conceived and has been investigated, which will be the topic of this thesis. In short, a specific facet of SiC crystal can be cut and polished. The resulting surface can facilitate large-area graphene growth using the thermal decomposition process. Various surface science tools as well as electronic transport experiments are used to characterize the samples.

It turns out, that the graphene on these non-polar facets are indeed very interesting and strongly influence by the substrate. Moreover, we found that not only large area graphene can be grown on these specially cut facets, but in some conditions very narrow nanoribbons can be grown as well due to extreme anisotropy of favorable growth direction.

1.4 Outline of the Next Chapters

I will present the main experimental techniques used in this research in Chapter 2. Chapter 3 will cover the growth and characterization of the samples while Chapter 4 focuses on the transport measurements and analysis of the samples. Chapter 5 will be the conclusion of this thesis and some outlooks are presented.

CHAPTER 2
EXPERIMENTAL METHODS

In this chapter, I will discuss the experimental methods used in this thesis. These methods can be categorized into several parts: sample growth, characterization, device fabrication and finally, electrical measurement. These are the four major phases during the life cycle of one sample.

2.1 Sample Annealing

High temperature annealing is performed in an induction coil furnace. As illustrated in Figure 2.1, a graphite susceptor crucible is placed in an vacuum chamber with a coil surrounding it. Large AC current passes through the coil, producing an alternating magnetic field, which in turn produces an induction current in the susceptor, heating it to the desired temperature. The crucible is made of graphite, because it can ensure the purity of elements in the growth environment. The graphite crucible is a simple cylindrical body with a cavity. The cap for the crucible can have a leak hole for Si vapor to escape. The crucible sits in a quartz tube and a pyrometer is used to measure the temperature through the tube. The quartz tube can either be under vacuum or filled with Ar gas.

In order to control the temperature accurately, an infrared pyrometer is used to measure the crucible temperature and provide feedback to the control program. The program adjust the output power accordingly using a PID algorithm.

2.2 Characterization Methods

We use Raman spectroscopy, atomic force microscopy (AFM), low-energy electron diffraction (LEED) and scanning electron microscopy (SEM) to characterize the samples.

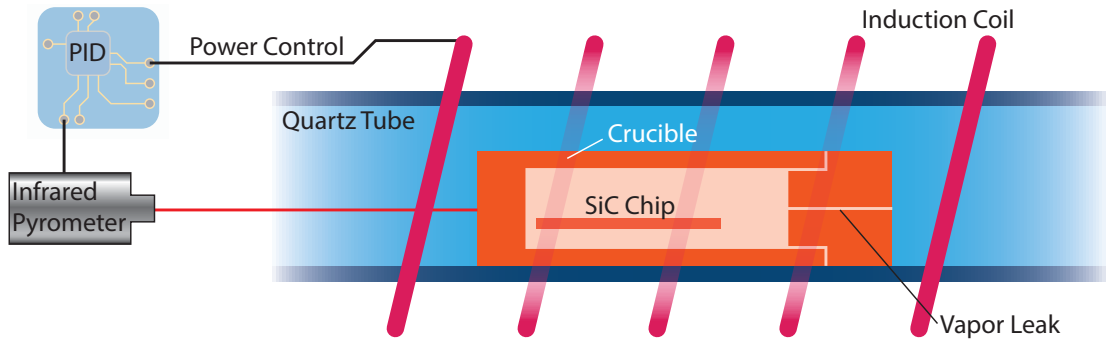

Figure 2.1: Annealing furnace setup. The graphite susceptor(crucible) is heated by a induction coil. A pyrometer takes the temperature which is used by a PID control program to determine the output power.

2.2.1 Raman Spectroscopy

Raman spectroscopy offers a non-intrusive way to quickly survey the quality of the graphene sample, including its defect level, strain, and charge density. Raman scattering is the the process of inelastic scattering of photons in a crystal by its phonons. In the Raman process, a photon excites the crystal, producing an electron-hole pair. The electron or hole then interacts with phonons in the crystal, yielding its energy. Afterwards, when they recombine, the emitted photon has an energy equal to the energy of the phonon less the original energy [55]. There is also a probability that the process gains energy instead of losing it by absorbing a thermally activated phonon but that is relatively low intensity and is not considered here [55].

Figure 2.2**d** shows two examples of the Raman spectrum of graphene. The main features are the D peak at $\sim 1340\,\mathrm{cm}^{-1}$, the G peak at around $\sim 1580\,\mathrm{cm}^{-1}$ and the 2D peak at $\sim 2680\,\mathrm{cm}^{-1}$. In order to understand the origins of these peaks, we need to look at the band structure of graphene.

The G peak results from the electron interacting with the phonon at the Γ point. During the G peak process (Figure 2.2), the incoming photon generates an electron-hole pair (blue line). The electron then gets scattered and lose some energy to produce a phonon at the Γ point (dashed line). Then the electron and hole recombine and emit a photon (red line). Notably, the excited electron doesn't have to lie in the vicinity of the π^* band. In fact,

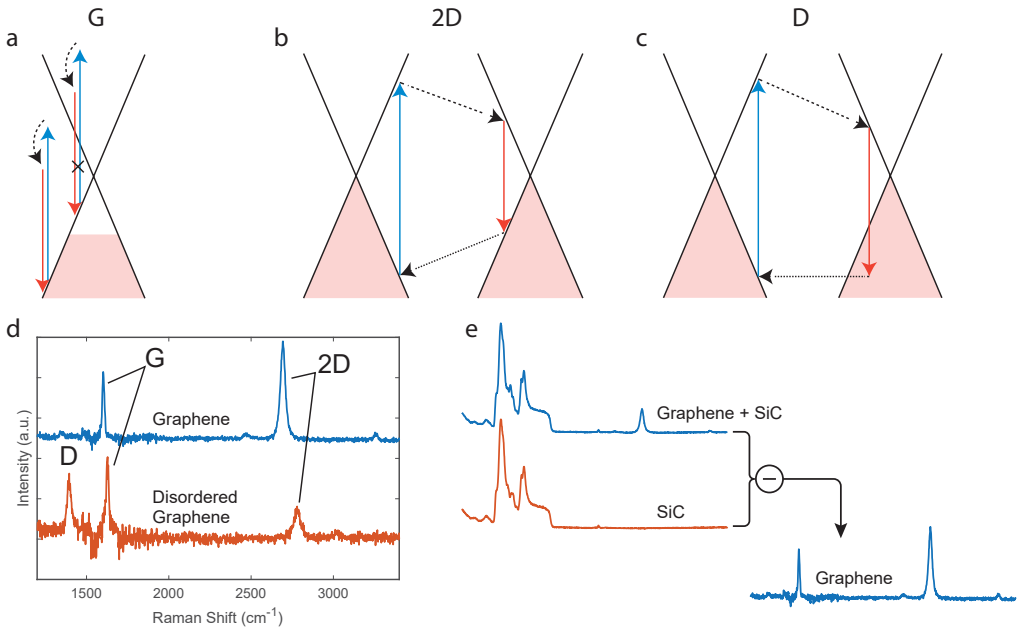

Figure 2.2: Raman processes in graphene and typical graphene Raman spectra. **a**. G peak process. Note that the excited electron doesn't have to lie in a small vicinity of the π^* band. One of the illustrated processes is crossed out because the hole doping makes the top of the π band empty, so there is no electron to excite. In the case of electron doping, similar elimination takes place due to Pauli exclusion principle. **b**. 2D peak process. c. D peak process. **a**, **b** and **c** are from Ref. [55]. Blue and red lines denote electron-hole pair generation and recombination while dashed lines denote scattering. **d**. Typical Raman spectra of graphene showing G and 2D peaks for the pristine graphene and a D peak for the disordered graphene. (Taken from sample 60YHQ4.) **e**. Because SiC has some Raman features in the range of graphene peaks, a SiC "background" spectrum is usually subtracted from the raw data to obtain a cleaner graphene spectrum.

the G peak has contribution from those electron-hole pairs with the electron's energy ε lying within $\sim \hbar\omega_L$ from the π^* band energy corresponding to the electron's wave vector $\varepsilon^{\pi^*}_{\boldsymbol{k}}$, where ω_L is the incident laser frequency. What's more interesting is the fact that the contributions from the wide range to available processes interfere destructively and produce a relatively small G peak in the case of a pristine single layer graphene (SLG). However, as the sample's doping level increases, part of the contributing processes get eliminated (see the crossed-out process in the figure). The result is that the G peak intensity increases as the doping level rises [55].

The D peak and the 2D peak are related to similar processes and their processes involve the TO phonons near the K point in the Brillouin zone [55]. Figure 2.2**b** and **c** display diagrams of the D peak and the 2D peak processes. The two processes look very similar except for a small difference in one of the inter-valley transitions.

Let's first look at the 2D peak process. As shown in Figure 2.2**b** the incoming photon produces an electron-hole pair. The electron and hole both get scattered inelastically by phonons near the K point, transferring two portions of the energy associated with the phonon to the lattice. The energy loss is represented in the figure by the slight slope in the dashed lines. As a result, the electron and hole both transition to the neighboring K′ cone and recombine, emitting a photon. The difference in energy between the original and the resulting photon is $h\Delta\nu = 2E_{TO}(\boldsymbol{q})$, where E_{TO} denotes the TO phonon energy.

The D peak process (Figure 2.2**c**) is the same as that of the 2D peak, except that one of the phonon scattering is replaced by a defect scattering. Since the scattering by a defect is elastic, there is no energy loss associated with that transition (flat dashed line in the figure). Thus the total difference in energy between the incoming and outgoing photons is $h\Delta\nu = E_{TO}(\boldsymbol{q})$. This process requires the presence of defects in the graphene lattice, 'D' meaning disorder or defects. In a perfect graphene lattice, the Raman spectrum doesn't show a D peak. And the D peak size can be used to infer the defect level in the lattice. E.g., it has been used to determine the average domain size of polycrystalline graphene

[56] since domain boundaries can scatter electrons and result in the D process.

Due to the conservation of momentum requirement in the phonon scattering process, the D and 2D processes lock in the phonons at a certain wave vector near the K and K′ points. Furthermore, the incoming photon energy determines the wave vector of the electrons and holes, and it in turn determines the wave vector of the phonon.

Kohn anomaly in graphene [57] causes the dispersion relation of the TO phonon band to be approximately linear to the wave vector relative to the K or K′:

$$E_{TO}(\boldsymbol{q}) \propto |\boldsymbol{q} - \mathbf{K}| = \Delta q. \tag{2.1}$$

As a result, there is a nearly linear dispersion relation between the excitation photon energy and the resulting D and 2D peak wave numbers. Thus, we need to note that the D and 2D peak positions relies on the specific laser wavelength, when comparing Raman spectra from difference labs. The Raman spectra presented in this work are all taken with a laser of wave length $532\,\mathrm{nm}$.

SiC has large intensity in the Raman spectrum compared to graphene. A confocal aperture in our Raman instrument helps focusing the spectral acquisition to several microns near the surface so that the SiC bulk's contribution is limited. Still, the spectra we have taken in the lab always are the superposition of Raman spectra of the graphene and its SiC substrate. To see the graphene features better, we usually do a SiC substrate Raman signal subtraction (Figure 2.2**e**). A more sophisticated method using a non-negative matrix factorization algorithm to extract a clean graphene spectrum from multiple data sets was demonstrated by Kunc et al [58].

Number of graphene layers

Raman spectroscopy can be used to differentiate single layer graphene (SLG), bilayer graphene (BLG) and multilayer graphene (MLG) for Bernal stacked graphene. Specifi-

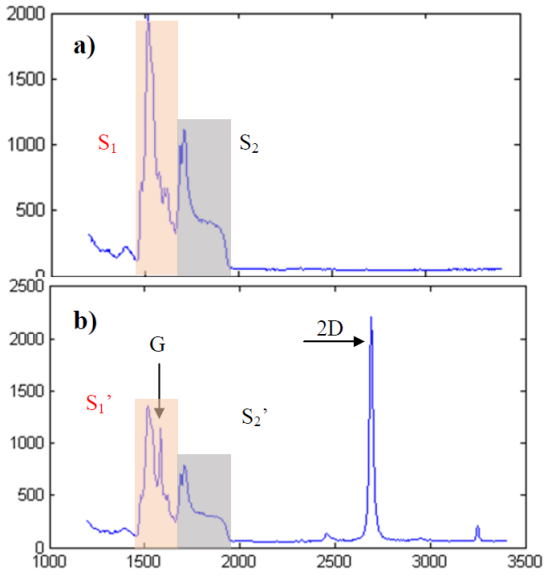

Figure 2.3: The Raman spectrum intensity in the range between 1460 cm^{-1} and 1960 cm^{-1} is divided into two parts. S_1 is the intensity between 1460 cm^{-1} to 1660 cm^{-1} and S_2 is that of 1660 cm^{-1} to 1960 cm^{-1}.

cally, because the degeneracy in the electron bands is lifted by the Bernal stacking order due to symmetry breaking, the incoming photon generates electron-hole pairs in the 2 different bands with slightly different wave vectors. Since the momentum has to be conserved in the electron-phonon process, these electrons and holes activate phonons with slightly different energies. The result is that the 2D band contains multiple components [55].

Note, however, that this multi-component feature cannot be used to identify SLG from MLG in the case of rotated stacking order. If the graphene layers are stacked without particular order, the individual sheets are electronically isolated from each other and the symmetry breaking won't necessarily happen. Thus, rotated stacked MLG sometimes appear very similar to SLG in Raman spectrum. One way to identify SLG from MLG is to use the G peak intensity.

Since each graphene layer contributes to the G peak, its intensity can be used to measure the approximate number of layers. The Raman spectrum's intensity is not absolute, so we can use the SiC background intensity as a normalization factor. A method was demonstrated in Y. Hu's thesis [33], where she used a G peak to SiC intensity ratio called G/S_2 ratio to estimate the number of layers. As shown in Figure 2.3, a Raman spectrum of pure

SiC has intensities in the two ranges S_1 and S_2. The intensities in the same two ranges in the SiC+graphene spectrum are $S_1' = S_1 + G$ and $S_2' = S_2$. We have

$$\frac{S_1'}{S_2'} = \frac{S_1 + G}{S_2}, \tag{2.2}$$

Thus

$$\frac{G}{S_2} = \frac{S_1'}{S_2'} - \frac{S_1}{S_2}. \tag{2.3}$$

This method shall be used with the caveat that G peak intensity does increase with doping level, as discussed earlier in this section. Also, SiC peak intensities may also vary from wafer to wafer and depend on the facet. In this thesis, the G/S_2 ratio is always used to compare number of layers of graphene samples within the same facet.

The Georgia Tech Epigraphene Lab uses a Horiba Jobin Yvon LabRam HR Raman spectroscope. The spacial resolution is about $1\,\mu\mathrm{m}$ in xy plane and about $5\,\mu\mathrm{m}$ in the z direction.

2.2.2 AFM

Scanning probe microscopy (SPM) is a very important tool for surface science. Generally speaking, a SPM is a nanoscopic probe attached to a scanning piezo. The probe is scanned across a sample's surface, and can sense the surface though some sensing mechanism. Depending on the different sensing technologies used, SPM's can be subdivided into several types. Atomic force microscopes (AFM), as the name suggests, use the atomic force to sense the surface.

The atomic force can be one of several types of forces usually in the van der Waals interaction range, which has a distance dependence that can be used as a feedback for distance control from the probe to the sample.

We operate the AFM in either one of two modes: the non-contact mode and the contact mode.

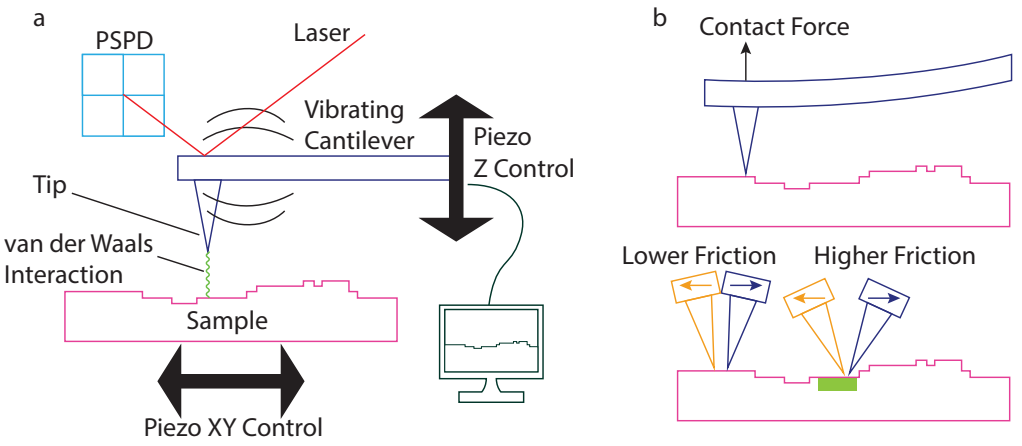

Figure 2.4: Non-contact mode and contact mode AFM/LFM. **a**, Non-contact mode AFM principle. The tip is on a vibrating cantilever near the resonant frequency, whose height is controlled by a piezo. A laser points to the cantilever and reflects onto a PSPD which reads out the vibration signal. When the tip is within van der Waals interaction range from the sample's surface, the resonant frequency is shifted a little bit. The shift is detected by the PSPD and used as a feedback to control the tip's distance from the sample's surface. As the sample gets moved by the piezo in the x-y plane, the sample's surface is traced by the piezo-controlled tip and output to the computer. **b**, In the contact mode, the contact force is used as the feedback. The contact force is measured by the amount of bending on of the cantilever, which changes the laser reflection. The lateral force can be measured in the contact mode. As the tip scans from left to right or from right to left, a lateral force drags the tip to twist in one way or another. This lateral force can be used to identify different materials based on their surface friction.

The non-contact mode works in the attractive force range. The tip cantilever is driven by a piezo to oscillate near its resonant frequency. The amplitude of the vibration is picked up through laser reflection by a position sensitive photo-detector (PSPD). The van der Waals interaction between the sample surface and the tip slightly decreases the resonant frequency, thus decreasing the vibration amplitude of the cantilever. This amplitude is used as a feedback for the AFM control to keep the tip at a certain distance from the surface.

The contact mode works with the repulsive force between the sample and the tip. As shown in Figure 2.4**b**, this force pushes on the tip and bends the cantilever beam, which is detected by the deflection of the laser. The contact mode has the advantage of being able to measure the friction force between the tip and the sample by the different laser deflection when the tip drags over the surface (Figure 2.4**b** lower half). The friction force microscopy (FFM) is can be used to identify graphene on SiC substrate, and even tell multilayer graphene from SLG [59].

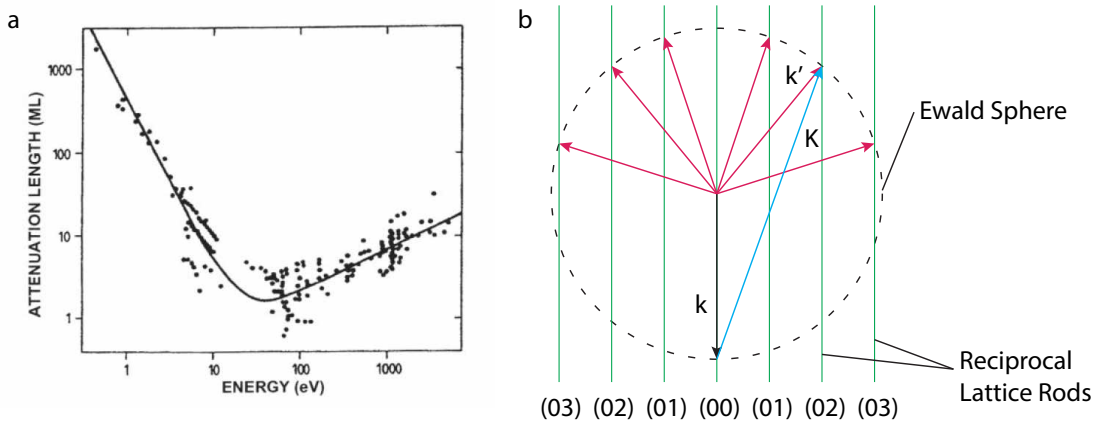

Figure 2.5: **a**, Electron attenuation depth in solids vs. electron energy, measured in number of atomic monolayers (ML). From Ref. [60]. **b**, An illustration of the von Laue condition in 2D. All the magenta arrows are allowed diffraction wave vectors. From Ref. [61].

2.2.3 LEED

Low energy electron diffraction (LEED) can be used to determine the surface 2D crystal structure of a solid. Low energy electron is used because the attenuation length minimum of electrons in a solid coincides with a wavelength on the order of the atomic spacing. As we can see in Figure 2.5**a** the attenuation length of electrons in a solid is lowest at energy ranging from 20-500 eV and the minimum length is about several monolayers of atoms (i.e. very shallow near the surface). On the other hand, the wavelength of an electron in this energy range is on the order of several Å which is on the order of the atomic spacing. These two factors allow probing the reciprocal space of the surface crystal structure of solids [61].

Diffraction in the surface or a 2D material is similar to that in the 3D crystal. The only difference is that the diffraction condition in the z direction is not required. Recall the von Laue condition for diffraction [62] and write it in only the xy components:

$$\boldsymbol{k}'_{\parallel} - \boldsymbol{k}_{\parallel} = \boldsymbol{K}_{\parallel}, \tag{2.4}$$

where $\boldsymbol{k}_{\parallel}$ and $\boldsymbol{k}'_{\parallel}$ are the xy components of the incident and outgoing wave vectors, and $\boldsymbol{K}_{\parallel}$

is the xy component of reciprocal lattice. The condition is illustrated in Figure 2.5.

When the crystal structure is modulated by a longer periodicity, the imposed periodicity may produce satellite peaks around the main diffraction peaks. Such phenomenon has been observed, for example, for the $6\sqrt{3} \times 6\sqrt{3}$R30° reconstruction of the buffer layer on the Si-face [63, 64].

The LEED experiments presented here were performed in Dr. Phillip First's LEED equipment at Georgia Tech.

2.2.4 SEM

Scanning electron microscopy (SEM) uses electron beam to probe the sample. Electrons emitted from the source are accelerated by a voltage along the z direction, focused by a set of electron lenses and moved in the xy direction by a scanning electric field. After an electron hits the surface, it can either backscatter or generate a secondary electron. These different types of electron emission from the surface can be collected by a detector and used to plot out an electronically lit image.

We mainly use the Hitachi SU8230 SEM, operating in the 1kV acceleration range and using the secondary electron for graphene imaging. It not only can provide a fast large scale imaging but also can determine relative graphene thickness. Based on my own experience comparing SEM, LFM and Raman spectra data, darker signals in SEM image usually indicates more layers of graphene. Quantitative analysis of the graphene thickness using SEM can be found in Ref. [65].

2.2.5 Other Characterization Tools

ARPES measurements were performed by V. Prudkovskiy and C. Berger in collaboration with A. Tejeda and the Soleil Synchrotron Cassiopée beam. STS measurements were done by D. Wander and A. De Cecco in the group of C. Winkelmann at CNRS-Grenoble. Landau level spectroscopy measurements were performed by T. Zhao and Y. Jiang at MagLab. The

Landau level spectroscopy data were analyzed by myself.

2.3 Fabrication

We use the common suite of microelectronics fabrication tools to fabricate the devices for electric measurements. Fabrication is like sculpting: it usually involve three major pieces: defining the pattern (lithography), removing materials (etching), and adding materials (deposition).

2.3.1 EBL

Lithography is the process of transferring a template pattern onto a material called resist. E-beam lithography (EBL) is the tool that uses electron beam to expose the E-beam resist. The resist usually is an organic film that is chemically sensitive to exposure of electron beam (e-beam). The exposure could make the resist either easier or harder to dissolve compared to the unexposed resist. A solution called developer is then used to remove the resist depending on the exposure pattern. Positive e-beam resist gets easier to dissolve after exposure while negative resist is initially easier to dissolve and gets harder to dissolve after exposure. We mainly use PMMA resist, which is a positive resist. For the negative resist, Ma-N 2403 is used.

2.3.2 RIE

Reactive ion etching (RIE) is used to etch graphene, SiC and Al_2O_3. In an RIE tool, a gas or a mixture of multiple gases are injected into a chamber in between two parallel metal plates. An ionizing high frequency AC voltage is applied on the plates and turns the gas into a plasma. Near each plate, there is a electron depletion region where a large potential drop from the plasma to the electrodes exists. Cations thus gets accelerated to hit the surface causing the etching of the material [66].

RIE is a technique that uses both chemical and physical properties of the etching gas.

The gas etchant is chosen to be able to chemically react with the target material. The plasma acceleration helps the ions to gain a higher kinetic energy to facilitate the etching process. That's why it is considered a intermediate between wet (chemical) etching and ion milling.

Some RIE systems have inductively coupled plasma (ICP) plasma sources in order to achieve higher plasma density without increasing the power of the etching [66]. These are often called ICP etcher.

We use a SAMCO RIE-1c for O_2 etching of graphene and SF_6 etching of SiC. To etch Al_2O_3, a Plasma-Therm ICP etcher is used with BCl_3 plasma.

2.3.3 PVD

Now we come to the section of adding materials. Physical vapor deposition (PVD) is the process where the material desired is vaporized and the vapor lands and deposits on the sample surface.

PVD is quite simple in principle: a material source is heated and evaporated, and the vapor condensate on the sample surface. It may be sub-divided into a several categories according to how the source material is vaporized.

EBE

Electron beam evaporation (EBE) is one of the PVD methods. Electron beam is emitted by a heated tungsten filament and then accelerated by a high voltage (~ 10kV). The beam is then guided by magnetic field to land on the material target.

We use EBE to deposit Au, Pd, Al and Al_2O_3. For Al_2O_3 deposition, we use a pure Al source, and deposit it in an oxygen environment. The oxygen pressure is kept at 5×10^{-5}mbar since higher pressure might cause the EBE to malfunction. The deposition rate is kept at ~ 0.1Å/s to allow the film to be fully oxidized.

Carbon Coater

Amorphous carbon (aC) is deposited by a carbon coater. A graphite rod is pushed against a graphite cone tip. A large current ($\sim$ A) is passed through the contact point, which concentrates a large power at the tip and evaporates carbon.

2.3.4 ALD

Chemical vapor deposition (CVD) is the process of depositing materials by means of chemical reaction from more than one species of precursors. Atomic layer deposition (ALD) is special type of CVD where the deposition is self-limiting. Instead of flowing the precursors at the same time as in traditional CVD, in the ALD process is divided into cycles of alternating precursor pulses. During each cycle, the precursors are pulsed into the reaction chamber successively. Each precursor by itself cannot form bulk deposition on the sample's surface but only leaves a single layer. This way, each cycle only deposits a single layer of the material. Hence the name atomic layer deposition. ALD is very reliable for Al_2O_3 deposition but it can also be used for a wide range of materials.

One distinctive feature of the ALD, as opposed to PVD, is that the deposition is isotropic, which means that the process can lead to the deposition on side walls as well as flat surfaces. Thus it's not ideal for lift-off process.

ALD Al_2O_3 deposition on graphene is tricky due to the lack of bonding on a smooth graphene layer with the precursors used. To mitigate the difficulty, a thin layer ($\sim 2\,\mathrm{nm}$) of seeding Al_2O_3 is usually evaporated by PVD, which can form bonds with the precursors.

We use a Cambridge NanoTech Savannah ALD. For the Al_2O_3 deposition, we use a water/trimethylaluminum (TMA) cycle at a temperature of 200-250 °C.

2.3.5 How does the pattern get transferred to the material?

We talked about lithography, etching and deposition, the three building blocks of the sample fabrication process. How do we transfer the pattern defined by lithography to the etching

and deposition?

A common way to use patterned resist to shape the deposited material is lift-off. During the lift-off process, material is deposited onto the substrate coated with patterned resist. After the deposition, the sample is immersed into a solvent to dissolve the resist, taking the material deposited on top of it off the sample. The pattern is thus defined. A successful lift-off requires that the patterned material's edge breaks off the lifted-off material. For this reason, a PMMA/MMA bilayer resist is usually used because the patterned resist edge is slightly undercut and cause the material to break off more easily.

When etching the material, we need a etching mask to selectively protect the regions we don't want to etch. Resist itself can be used as an etching mask. However, being organic, the resist sometimes gets etched at a high rate. If the resist thickness is not enough to withstand the etching. We need to resort to other etching masks. Another disadvantage of using resist as the etching mask is that the some organic resist gets hardened during the etching process and cannot be subsequently removed by solvents.

We can use the lift-off technique to fabricate the etching mask. A good etching mask choice depends on the chemical properties of the etching agent. For example, RIE with O_2 is used for etching graphene. While organic resist is also etched by O_2, Al_2O_3 is very resistant agains O_2 etching. Thus, alumina is a great choice as there is little risk of over etching and removing the etching mask all together when etching thick graphene/graphite.

2.3.6 Protective Layers

Graphene is easily doped by virtually anything: air, solvents, water [67, 68, 69]. For example, we found that with just a few minutes exposure to the air, the charge density of the graphene increase by a lot [37, 15]. Thus, researchers have been looking for ways to alleviate this problem. Generally speaking, all the methods utilized are all some kind of protective layer deposited on graphene to prevent any contaminants to get in touch with it.

Hexagonal boron nitride (h-BN) is one of the most popular protective layer for graphene

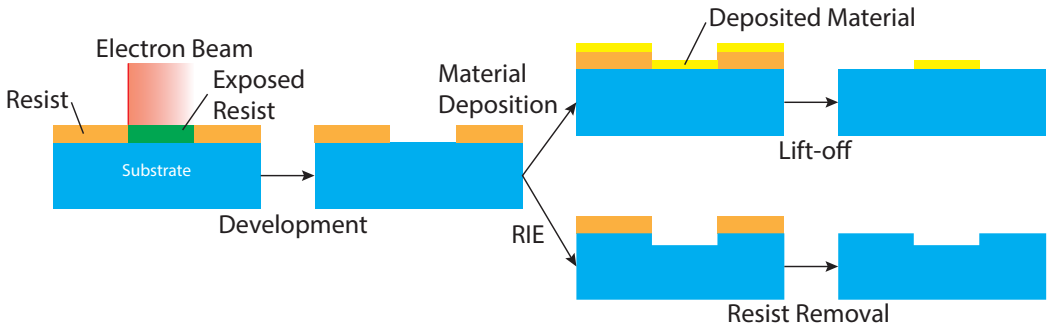

Figure 2.6: Sample fabrication process. First, the sample is spin-coated with E-beam resist. The resist then gets exposed by electron beam. In the case of a positive (negative) resist, the exposed (unexposed) part of the resist will get dissolved by the developer solution. Illustrated here is the case of the positive resist. Depending on the need, the sample is either etched or some material is deposited anisotropically. The resist is then removed. If some material is deposited, unwanted portion will be lifted-off during the removal of the resist.

because it is also a 2D material and can be layered on top of graphene with only mild interactions (van der Waals). Exfoliated h-BN/graphene/h-BN structure has been used to produce a lot of interesting experiments. As for epigraphene, it is not very feasible to exfoliate h-BN and layer it to top and we have to turn to deposition methods.

The researchers at Georgia Tech Lorraine together with the Epigraphene Group has pioneered a chemical vapor deposition method called lateral atomic deposition [70]. As a bottom up deposition technique, this method has real potential to be used in industrial production.

As the h-BN deposition method is still under development, other materials has been used for the protective layer purpose. Al_2O_3 has been used as a gate dielectric [5, 41] and tunneling barrier [10, 9, 43]. It has also been demonstrated to protect graphene from air contamination [69].

In order to contact the graphene protected underneath the protective Al_2O_3, two methods can be used. One is to use wet oxide etchant to etch Al_2O_3 [71]. The disadvantage is that the wet etch tends to undercut is rate is not controlled well.

Another method is to use the edge contact that is similar to the technique used for h-BN sandwiched graphene [72]. We etch the Al_2O_3 with RIE and expose the side of graphene. By filling that hole with the contacting metal, the metal will make contact with

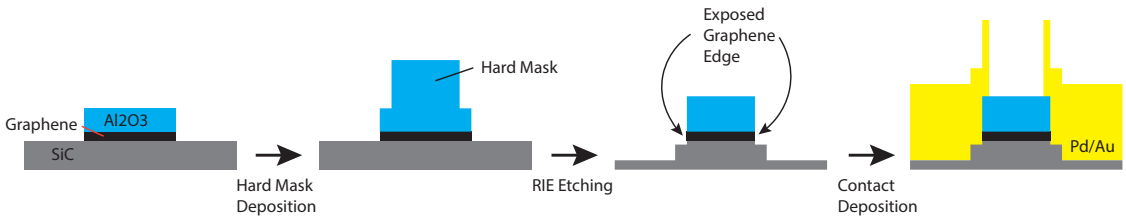

Figure 2.7: To expose the edges of the graphene covered by Al_2O_3, a hard mask of Al_2O_3 is deposited and the sample is etched under BCl_3 RIE. Then the metal contacts are deposited.

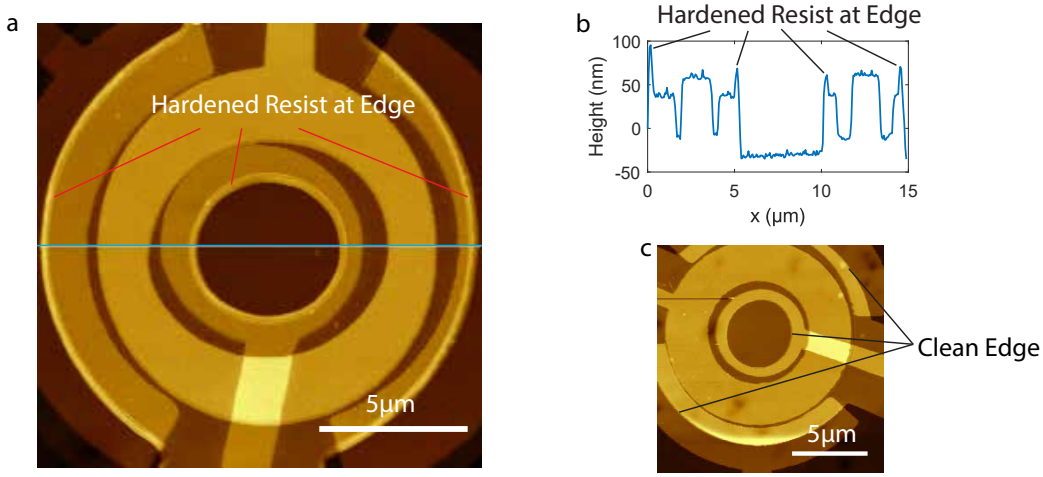

Figure 2.8: a, An AFM image showing the resist residues due to hardening by ICP-RIE. The residues cause a $\sim$ MΩ resistance. **b**, The height profile of the blue line drawn in **a**. The resist residue has a thickness of tens of nanometers. **c**, An AFM image showing a device that was etched with Al_2O_3 hard etching mask instead of resist. There is no resist residue at the edge and the contact resistance is low.

the graphene's edge. Etching masks have to be reliable and resistant to the harsh RIE process in order to expose a clean edge. As we discussed earlier, organic resist gets hardened during an RIE process, which will form resist residue at the edge of graphene (Figure 2.8). Contacts made with these edges exhibit $\sim \mathrm{M}\Omega$ contact resistance and can be unstable.

2.3.7 Process Flow

The devices presented in this thesis will typically be fabricated by either of two types of fabrication process: Hall bar process and Corbino ring process.

Hall bar process flow

The sample is coated by alumina first in an E-beam evaporator. In order to define the pattern, another layer of alumina is deposited with the pattern by means of lift-off. The structure is then etched in BCl_3 plasma in the Plasma-Therm ICP. The BCl_3 RIE etches alumina as well as graphene. An optional additional O_2 etching is conducted to remove any remaining graphene.

In order to make electric connection to the graphene device, Pd and Au contacting pads are used. The pattern is defined by exposure of PMMA in an EBL. Since the graphene layer is underneath the alumina layer, a wet etching is used to expose the covered graphene layer. The wet etching is supposed to be very mild and quick to restrict the undercut problems typical to wet etching. PMMA is resistant against alumina etchants, so the contact pattern can be directly used for wet etching purposes. A Pd and Au bilayer is evaporated on the sample using E-beam evaporation followed by lift-off. The sample is then covered by alumina again as a gate dielectric layer, on top of which a pattern of Pd and Au are evaporated as the gate electrode.

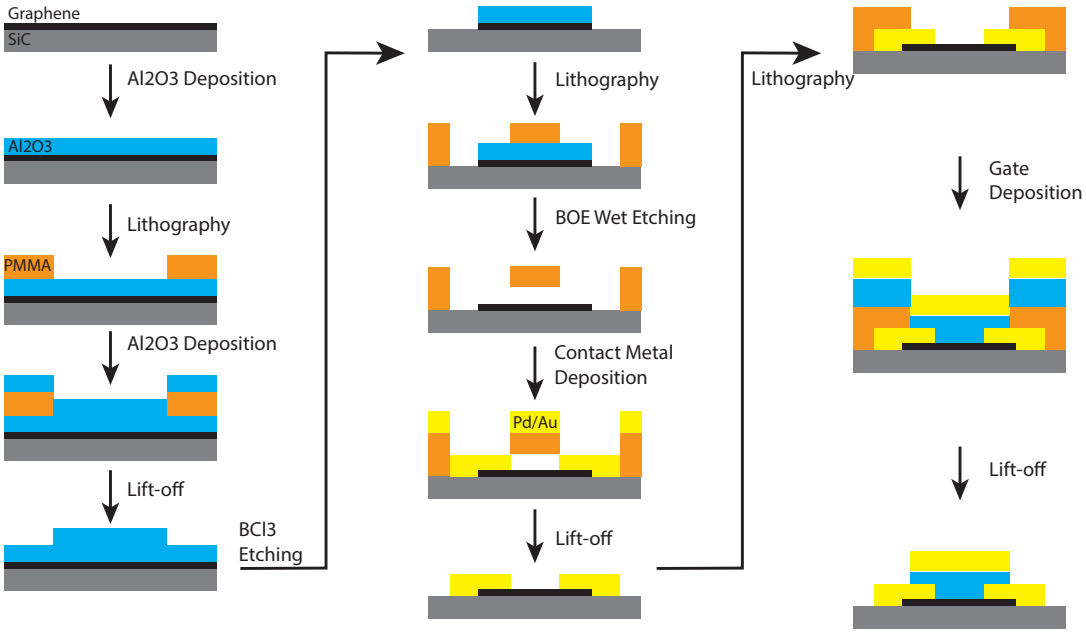

Figure 2.9: A typical process flow of a Hall bar sample.

Corbino ring process flow

The other setup is a little bit more involved for fabricating the Corbino ring because the inner electrode needs to cross over the gate without making an electric contact. In order to achieve this, we deposit the gate first, coat it with Al_2O_3 to insulate it from other contacts, and then run the contact electrode over it (Figure 2.10).

2.4 Electrical Measurements

Once the sample is fabricated, it is mounted on a chip holder, wirebonded and inserted into the cryostat for low-temperature electric measurements. We use a cryocooler that is equipped with a variable temperature insert allowing measurements in the range 1.6-423K, and with magnetic field up to 9T.

A typical electric measurement set-up is shown in Figure 2.11. An AC voltage source with frequency in the 10-30Hz range (V) is connected to the sample with a large resistor in series(R_S). The series resistor's resistance is much larger than that of the sample $R_S \gg$

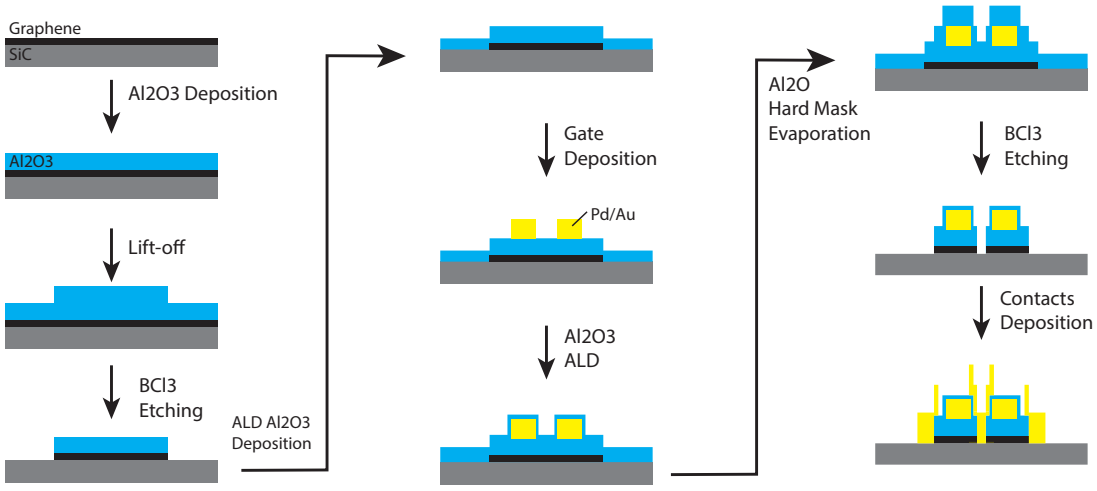

Figure 2.10: A typical process flow of a Corbino ring sample.

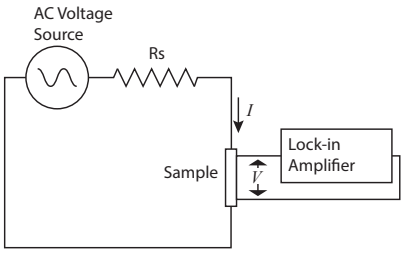

Figure 2.11: Lock-in amplifier measurement setup.

R_{Sample} so that the current in the circuit is $I \approx V/R_S$. The current is usually in the 1-100nA range to avoid electronically heating the samples. We use lock-in amplifier to measure an AC voltage on the sample (V_{Sample}). The lock-in amplifier takes the time-dependent voltage on the sample and integrates that with the reference source signal over a certain time period and normalizes the result. Thus, the reading obtained from the lock-in amplifier is the amplitude of the AC voltage on the sample at the source frequency. This way, noise in the measurement can be filtered out and the real (resistive) and imaginary (capacitive) signals are decoupled.

CHAPTER 3

GROWTH AND CHARACTERIZATION OF GRAPHENE ON NON-POLAR SIC FACETS

In this chapter, the sample growth and characterization results are presented and discussed. In this work, various SiC facets have been explored with very diverse and interesting growth patterns in terms of the characteristics of the graphene that grows on these facets. Just like on Si- and C-facets, graphene grows and behaves very differently depending on the underlying facet. In most cases, the growth is epitaxial. In addition to graphene, a graphitic interface layer is found on all the Si-side facets.

In this and the following chapters, the crystal facets are name by the corresponding epigraphene edge types (AC/ZZ) and the angle. The SiC crystal facet indexing, naming, and angle information can be found in Appendix A.

3.1 Substrate Preparation

The substrate used in this work were all cut and polished either by myself at Georgia Tech or by our collaborators at the Tianjin International Center for Nanoparticles and Nanosystems (TICNN).

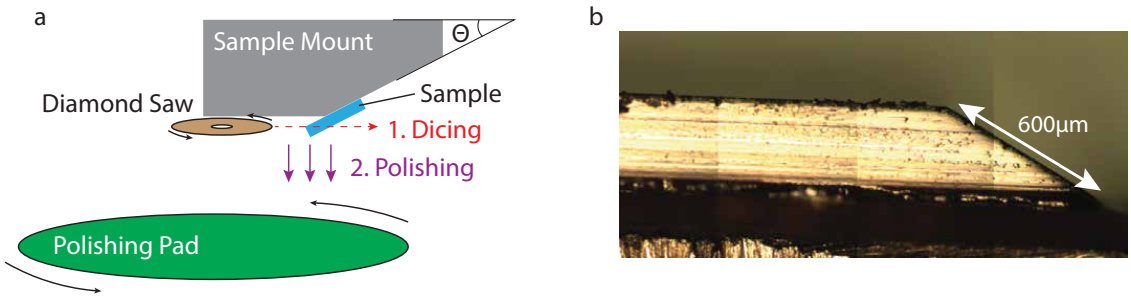

Figure 3.1: a. To cut the sample at a specific angle, we mount the sample onto a chuck with a specific angle to cut and polish. **b**. An example of a cut sample. Note that due to the thickness of the wafers, the size of the cut typically are approximately 600 µm.

At Georgia Tech substrates were taken from polar SiC wafers and cut by a diamond dicing saw. The samples were then polished in a polisher in Dr. Zhigang Jiang's lab. This method allows us to quickly produce small batches of prototyping samples to try out various SiC facet orientations. As shown in Figure 3.1**a**, an on-axis SiC sample is mounted on a chuck with the desired angle. First, the sample's edge is cut using a diamond blade. The cutting process leaves a very rough surface. Then the chuck is mounted on a South Bay Technology 155 polishing fixture and put on a South Bay Technology model 910 lapper/polisher for the polishing process.

The polishing process consists of two steps: lapping and polishing. Firstly, a series of sandpapers with decreasing particle sizes are used to take off the vast majority of material. In our case, a 180 grit size SiC sandpaper is used, followed by a 320 and then a 600. Then, a series of diamond powders with decreasing sizes, from $3\,\mu\mathrm{m}$ down to $0.1\,\mu\mathrm{m}$, are used to finish up the surface. The resulting surface has an RMS roughness of about 2.7Å (Figure 3.2**a**). As shown in Figure 3.1**b**, these samples are cut at the edge and can only allow characterization measurements but not device fabrication and electric measurements.

In order to make devices and perform electric measurements, wafers cut to the specific facets are necessary. Our collaborators at TICNN have developed the capability to cut SiC crystal rod into wafers at desired facet angles and polish these wafers.

The 4H-SiC AC facet samples presented in this thesis were all cut and polished by TICNN, expect for those in Figure 3.5**a** and Figure 3.17, which were cut and polished by myself. The substrates for the other facets presented here were all cut and polished by myself.

3.1.1 Pre-growth Annealing

The mechanically polished surface isn't yet ready for graphene growth. As shown in Figure 3.2**a**, the surface still has a lot of scratches. Pre-growth annealing is used to smooth out the surface. Because the temperature required for surface mass flow is similar to the growth

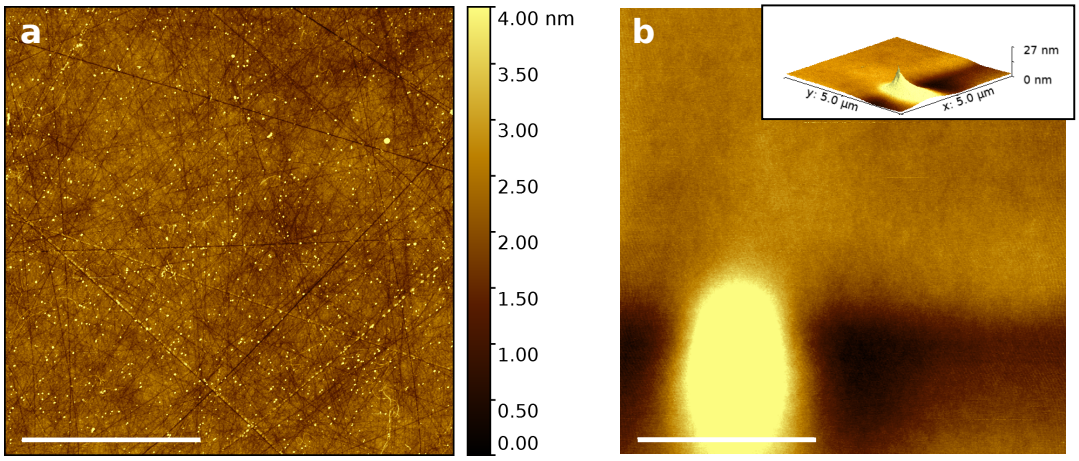

Figure 3.2: a, AFM image of the sample surface after polishing. The RMS roughness is about 2.7Å. **b**, AFM image of the sample surface after H_2 etching process. The scratches due from the polishing are gone and the RMS roughness is 0.8Å. **Inset**: a 3D rendering of the topography. Scale bar: $2\,\mu\mathrm{m}$

temperature, we need some mechanism to inhibit the growth of graphene. For this purpose, two processes can be used: H_2 etching [73] and confined annealing.

In the H_2 etching process, H_2 gas is introduced into the chamber to etch away the excessive C atoms during the annealing, thus preventing the graphene from growing. The main disadvantage of H_2 annealing is that the result is not consistent, and depends on the gas flow pattern. Specifically, I found that when the H_2 flow perpendicularly to the treated surface, the result is better. The other disadvantage is that H_2 etches the graphite crucible as well and makes it porous after a few runs.

The confined annealing uses a confinement to create a high Si vapor pressure which prevented growth. More discussion can be found in the following section. Either Ar atmosphere confinement (Ar annealing) is used or a face-to-face (FTF) annealing is used. In the FTF annealing process, two samples are stacked face to face. The tight space in between creates the confinement.

In the case of the edge samples, since the surface of interest is on the cut edge, it is impossible to stack two surfaces against each other, so H_2 etching or Ar annealing is used. In the case of wafer samples, FTF or Ar annealing is used. The surface quality produced

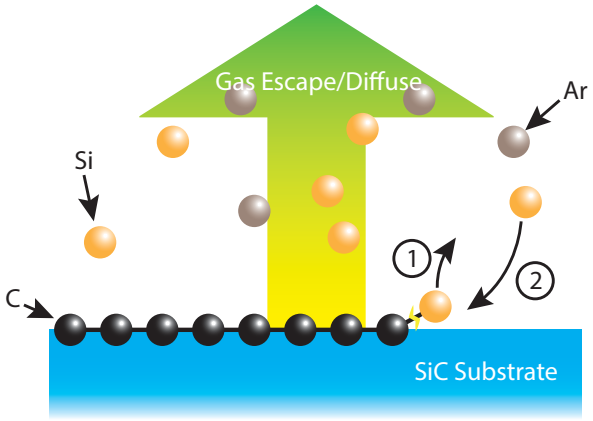

Figure 3.3: The graphene growth rate is determined by the partial pressure of the Si vapor near the surface. Microscopically, two processes compete in the regime of dynamic equilibrium: 1. a Si atom detaches from the surface and leaves an excess C atom for the graphene; 2. a Si atom in the vapor near the surface recombines onto the surface. In the process of the confinement controlled sublimation, the Si vapor escape rate is controlled by the confinement. A larger Si vapor pressure can be achieved by a small crucible leak hole or the use of Ar or both.

by these methods are similar, though H_2 etching tends to be unreliable.

A typical surface after pre-growth annealing is shown in Figure 3.2**b**. We immediately notice that the surface does not have the large terrace structure as in the case of polar faces (e.g. Figure 1.5**c**). As we will see in the Section 3.3, in the case of 4H-SiC AC 37° facet, after the surface is covered with graphene, the surface starts to form terraces (Figure 3.14), an indication of the existence of a stable facet.

The peak on the surface (Figure 3.2**b Inset**) is likely due to some impurity that pins the surface step flow [74]. The pinning effect could be utilized for pre-growth patterning as shown later in Subsection 3.3.1.

3.2 Graphene Growth

Figure 3.3 is a diagram illustrating the epigraphene growth mechanism. The decomposition of the SiC surface at an elevated temperature can be modelled as a dynamic equilibrium. In an balanced condition, the silicon atoms sublimes and deposits at the same time. Thus, the growth rate and quality is dependent on the Si vapor pressure near the sample's surface, we have three methods to control it. The first method is to use a crucible with a small leak

hole on the crucible. The leak hole is a confined diffusive path for the Si gas to escape and maintains a Si partial pressure inside the crucible. To achieve even higher partial pressure, a cap without a hole may be used. The second is the introduction of Ar gas. Ar gas is an inert gas so it doesn't react with the sample or crucible and it reduces the diffusion rate. The third is the FTF confinement discussed in the previous section.

Based on my experience, Ar annealing/growth is the most reliable method among the three. FTF confinement is more convenient than the Ar annealing since it does not involve opening and closing gas valves in the middle of the process. However, it usually produces samples that have more graphene near the chip edges because the Si vapor pressure is lower near edges. Leak hole confinement does not produce high enough Si vapor pressure and the growth rate is very high and hard to control. Ar annealing can be used to flatten the surface at a relatively low temperature ($\sim 1550\,^{\circ}$C) and to grow graphene at a higher temperature ($> 1600\,^{\circ}$C) so that both processed can be done in one run.

3.3 Characterization Results

In the following section, the SiC($\bar{1}10n$) facet is referred to as the AC facet while the SiC($11\bar{2}n$) the ZZ facet. We also studied the SiC($11\bar{2}\bar{n}$) facet which is facing towards the C-face, and is dubbed the C-side ZZ facet here. All facets discussed here are Si-side facets unless explicitly labeled C-side. SiC facet indices and facet angles and their names are listed in Appendix A.

Depending on the facet, the growth result can be very different. In general, the SiC AC facets form regular terrace/step structure (Figure 3.14) during graphene growth, while SiC ZZ facets rarely form such structures. Raman spectroscopy shows that on both facets there is a carbon-rich "interface layer", which is characterized by large D and G peak with no 2D peak. The graphene on SiC C-side ZZ facet doesn't have the carbon-rich interface layer. In all cases, there is highly strained graphene, according to Raman spectroscopy. In some cases the strain could be released via exposure to air or some chemical treatment.

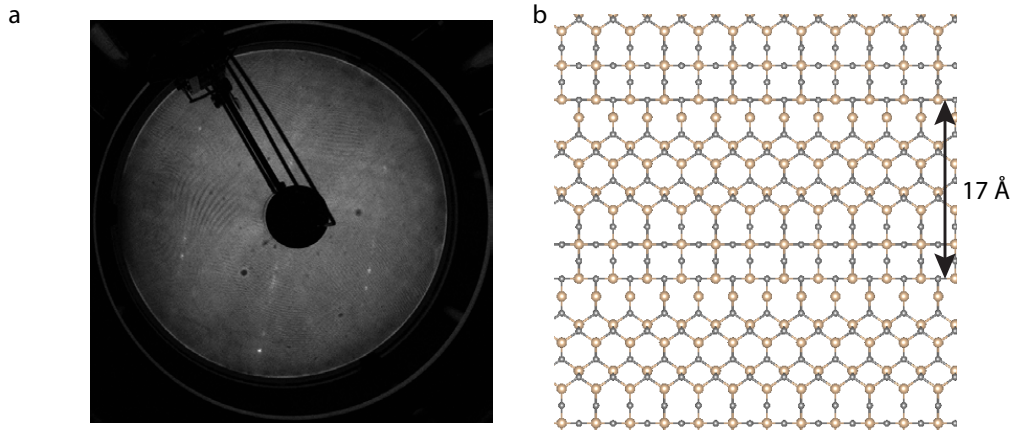

Figure 3.4: **a**, The LEED pattern taken on an interface layer sample on the 4H-SiC AC 37° facet at 76V acceleration voltage. No hexagonal graphene pattern can be discerned. The only peaks that can be seen correspond to the periodicity of the SiC facet. **b**, The surface crystal structure of the 4H-SiC AC 37° facet.

3.3.1 Graphene on the 4H-SiC AC Facet

On the 4H-SiC AC facet, much focus has been placed on 4H-SiC($\bar{1}$105) facet, which is 37° from SiC(0001) face. The surface crystal structure is shown in Figure 3.4**b**. The Wulff diagram of 4H-SiC indicates that a stable facet exists at this angle at 1480 °C [75] (See Appendix A). ARPES and STM studies on the graphene on this facet show that it is charge neutral.

Depending on the growth condition, time, and temperature, the amount of growth can be controlled. At 1600 °C with a short time (1 hour), small patches of graphene are grown on the surface, while with a longer time ($>$ 2 hours depending on the crucible condition), multi-layers are grown with a coverage over the whole surface. Raman spectroscopy is used as the main tool to identify graphene and indicate the number of layers and its quality. In general, the surface of the face after growth fall into 5 categories: (1) bare SiC, (2) graphitic interface layer, (3) highly-strained graphene monolayer, (4) less-strained graphene monolayer, and (5) graphene multilayer. Bare SiC is an area with no graphite-related characteristic peaks. I will mainly focus on the other 4 cases.

Graphitic interface layer

In this type of area, the Raman spectrum only has graphite related G peak and disorder related D peak Figure 3.5**b**. This usually indicates nano-crystalline graphite, with small grain size [56]. It is unlikely that amorphous graphite material grows on SiC with the well-controlled growth condition we have. So this phenomenon should come from the influence of the substrate, which is not unlike the situation on the Si-face graphene buffer layer. This conclusion is further corroborated by the graphene layer relaxation study presented later in this subsection: the interface layer + SLG gets relaxed into a BLG with a very small D peak in Raman spectrum (Figure 3.15).

The positions of the D and G peaks are $\sim 1380\,\mathrm{cm}^{-1}$ and $\sim 1610\,\mathrm{cm}^{-1}$, respectively. Both are blue-shifted with respect to the free-standing graphene ($\sim 1340\,\mathrm{cm}^{-1}$ and $\sim 1580\,\mathrm{cm}^{-1}$, respectively) [76]. This indicates a very large compressive strain estimated by extrapolation to be on the order of -1% in the film [77, 78].

The LEED pattern taken on an interface layer sample did not show any sign of graphene hexagonal pattern (Figure 3.4**a**). Only SiC AC facet patterns were seen.

Based on the fact that graphene growth is always accompanied by the interface layer growth and not the other way around, we can infer that the interface layer grows before graphene. As an example, the SEM image (Figure 3.5**a**) shows trapezoidal graphene patches grown in a region that is covered by the interface layer.

High-strain single layer graphene

With very carefully confined growth conditions, we can grow patches of SLG up to several tens of $\mu\mathrm{ms}$, as can be seen in the SEM image in Figure 3.5**a**. Typically the patches grow in trapezoidal or triangular shapes (depending on the growth aspect ratio) with the long edge running along the SiC$\langle 11\bar{2}0\rangle$ direction, parallel to the conventional AC direction of graphene on SiC Si-face. The trapezoid-shaped growth indicates that the growth is epitaxial, which is confirmed by LEED as shown in Figure 3.6.

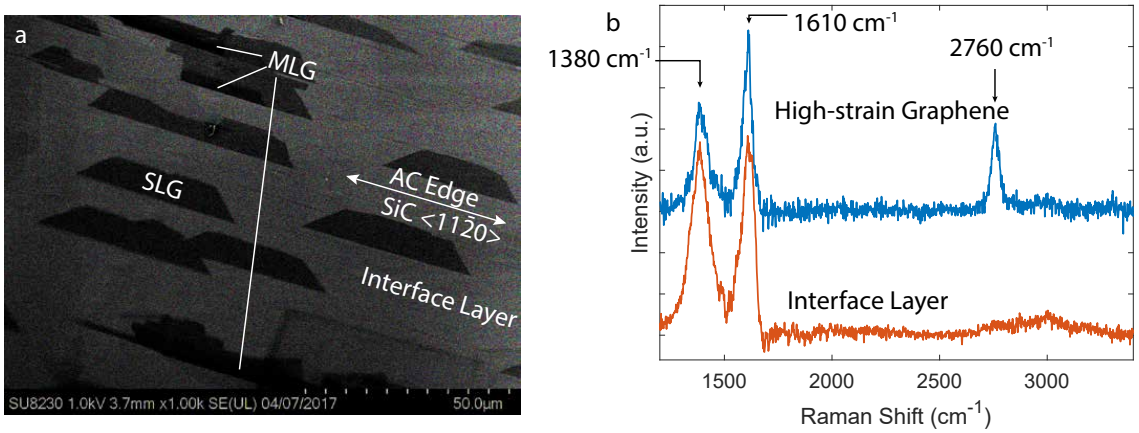

Figure 3.5: **a**, SEM image of a typical starting phase of graphene growth. High-strain graphene, which is indicated by darker area, forms shapes of trapezoids. The bottom and top edge is straight, aligning along the SiC$\langle 11\bar{2}0\rangle$ direction. The grey area outside the trapezoids is interface layer. **b**, A Raman spectrum of high-strain graphene and interface layer. Note that the 2D peak of the graphene is blue-shifted to $\sim 2760\,\mathrm{cm}^{-1}$ from $\sim 2680\,\mathrm{cm}^{-1}$ in freestanding graphene.

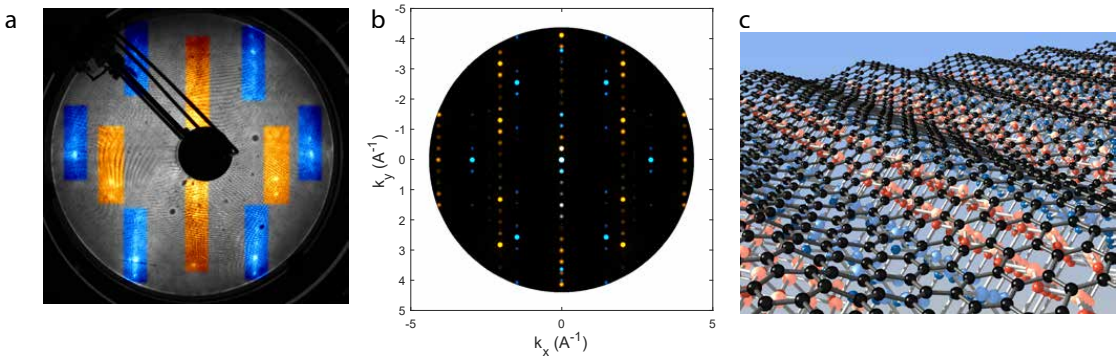

Figure 3.6: **a**, A LEED image taken on a sample with high-strain graphene growth on the 4H-SiC AC facet, at 76 V. The graphene peaks and the SiC peaks are colored by blue and orange respectively. We can see that the two sets of peaks are aligned with each other. Each graphene peak is accompanied by a line of satellite peaks. The graphene peaks and the SiC peaks align well with each other, proving the growth is epitaxial. **b**, A qualitative simulation of LEED pattern taken at 76 V acceleration voltage. The coloring scheme is the same as that in **a**. **c**, A qualitative illustration of the corrugation of graphene due to the underlying SiC pattern of the 4H-SiC AC facet. The SiC crystal is colored blue and red to indicate the periodicity of the surface supercell.

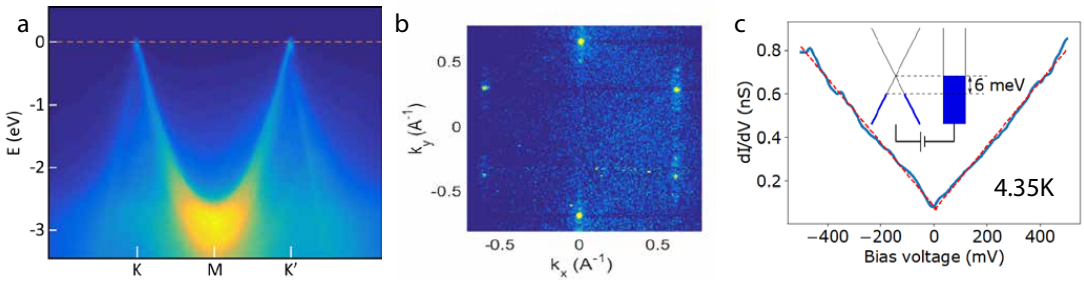

Figure 3.7: **a**, ARPES image of the high-strain graphene on the 4H-SiC AC facet, performed by V. Prudkovskiy and C. Berger in collaboration with A. Tejeda and the Soleil Synchrotron Cassiopée beam. The red line shows the zero energy level. The graphene is indeed charge neutral. **b**, Equi-energy cut of the ARPES at $E = 0\,\mathrm{eV}$ showing the six K points and some satellite points. **c**, The STS result of the same sample indicates a charge neutral graphene film, performed by D. Wander and A. De Cecco in the group of C. Winkelmann, CNRS-Grenoble.

The Raman spectrum (Figure 3.5**b**) shows a 2D peak which is heavily blue-shifted, located at $\sim 2750\,\mathrm{cm}^{-1}$ ($\sim 2680\,\mathrm{cm}^{-1}$ for free standing graphene). The 2D peak intensity lower than that of the G peak yet it's shape is relatively sharp, with a FWHM of $\sim 40\,\mathrm{cm}^{-1}$. All these features indicates a graphene film with a high compressive strain on the order of -1% [77, 78].

There is a significant D peak at $\sim 1385\,\mathrm{cm}^{-1}$. This D peak is most likely associated with the interface layer and not from the high-strain SLG. As discussed later and shown in Figure 3.11, the interface layer Raman can match the D peak in the Raman spectrum of high-strain SLG very well.

LEED measurements done on this type of graphene has hexagonal spots corresponding to graphene that is aligned with the substrate pattern (Figure 3.6**a**). The graphene pattern spots are accompanied by an array of satellite points, with that same spacing as the SiC pattern. This can be interpreted as the undulating effect from the substrate (Figure 3.6**c**). A qualitative simulation of such an effect is shown in Figure 3.6**b** and confirms the pattern found in the LEED. The undulating pattern was also seen in preliminary STM studies that is still under analysis.

ARPES measurement and STS (Figure 3.7) both show that the high-strain graphene on this facet is charge neutral. The Fermi velocity determined by ARPES is $1.04 \times 10^6\,\mathrm{m/s}$.

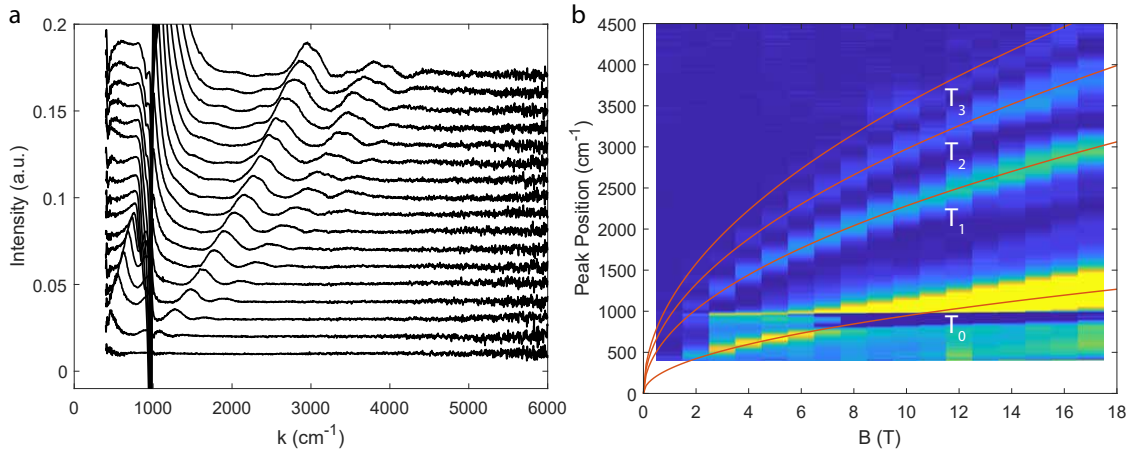

Figure 3.8: a, The Landau level spectroscopy results of high-strain graphene on the 4H-SiC AC facet, performed by T. Zhao and Y. Jiang at MagLab. **b**, The peaks in the spectra are fitted by Eq. 3.2. The fitting parameter $c^* = 1.02 \times 10^6\,\mathrm{m/s}$.

Figure 3.8 shows the Infrared (IR) spectroscopy under high magnetic fields revealing the Landau levels developed in the high-strain graphene. The Landau level in SLG has energy [44]

$$E_n = \mathrm{sgn}(n) c^* \sqrt{2e\hbar B|n|}, \tag{3.1}$$

where c^* is the Fermi velocity of graphene. The selection rule dictates that transition only happens between the Landau levels $L_{-n} \to L_{n\pm1}$, which corresponds to

$$\Delta E_{T_n} = c^* \sqrt{2e\hbar B}(\sqrt{n} + \sqrt{n+1}), \tag{3.2}$$

labeled T_n in Figure 3.8**b** [44]. The peaks were fitted with Eq. 3.2 and the fitting parameter $c^* = 1.02 \times 10^6\,\mathrm{m/s}$, which is in agreement with the ARPES measurements.

There are at least two types of highly-strain SLG found on the 4H-SiC AC facet, with very subtle difference in their Raman spectra as shown in Figure 3.9. I named them type I and type II. These two types are not exhaustive and there might be more different types. Apart from Raman spectroscopy, I haven't found other reliable techniques to tell the difference.

In summary, the high-strain graphene grows epitaxially on top of the interface layer. It

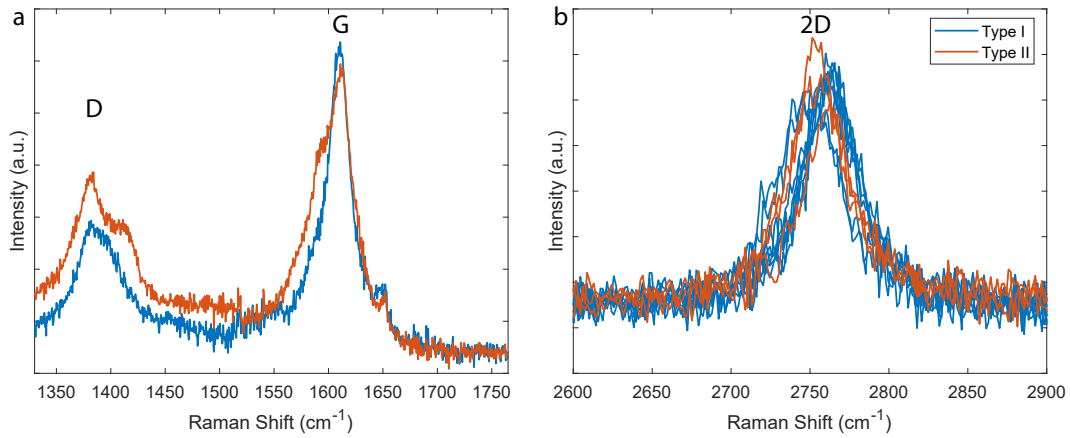

Figure 3.9: a, The D and G peaks and **b**, 2D peak of comparisons of type I and type II high-strain graphene. The two types have very subtle difference in their G and D peaks while virtually no difference in their 2D peaks.

is highly compressively strained, undulated by the substrate periodicity, and charge neutral.

Low-strain graphene

Low-strain graphene can be identified with Raman on the 4H-SiC AC 37° facet (Figure 3.10**b**). The G peak is low compared to the SiC spectrum. Using G/S_2 ratio introduced in subsection 2.2.1, we can differentiate SLG from BLG or MLG. The G and 2D peaks are at $\sim 1581\,\mathrm{cm}^{-1}$ and $\sim 2689\,\mathrm{cm}^{-1}$, respectively. They are only slightly blue-shifted compared to those of freestanding graphene, whose G and 2D peaks are at $\sim 1580\,\mathrm{cm}^{-1}$ and $\sim 2680\,\mathrm{cm}^{-1}$, respectively, indicating a $\sim -0.1\%$ strain [77]. The 2D peak has a FWHM of about $29\,\mathrm{cm}^{-1}$, which is very narrow. On a closer look at the G peak, we can notice that there is a smaller side-peak on the blue-shifted side. Lorentzian function fitting reveals the side-peak position to be $1616\,\mathrm{cm}^{-1}$, very close to the G peak position of the graphitic interface layer ($\sim 1615\,\mathrm{cm}^{-1}$).

There is also a significant D peak in this spectrum, similar to the case of highly strained graphene. Its position is at $1394\,\mathrm{cm}^{-1}$, which does not correspond to half of 2D peak position ($\sim 1345\,\mathrm{cm}^{-1}$)*. However, as is the case of the G peak, its position is quite close to that of the graphitic interface layer ($\sim 1386\,\mathrm{cm}^{-1}$). These facts suggest that the interface

*The D peak position and half of that of the 2D peak should agree within $\sim 10\,\mathrm{cm}^{-1}$ [55].

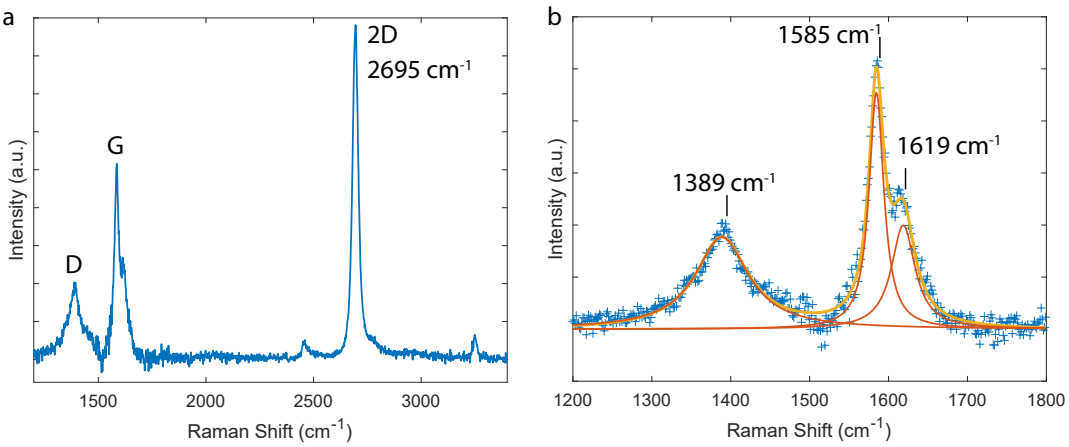

Figure 3.10: **a**, Raman spectrum of a low-strain graphene monolayer on the 4H-SiC AC facet. **b**, A zoomed-in look at the D and the G peaks. The G peak contains a secondary peak that might be associated with the interface layer. The D peak's position at $1389\,\mathrm{cm}^{-1}$ deos not correspond to the half of the 2D peak's position. Thus, it most likely is associated with the interface layer instead of the monolayer.

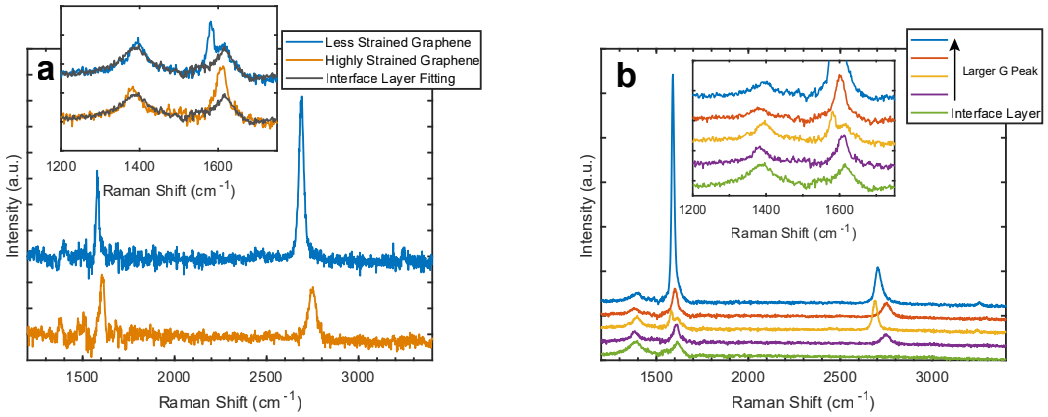

Figure 3.11: Raman spectra of 4H-SiC AC facet graphene and interface layer component analysis. **a**, Raman spectra of the high-strain graphene and the low-strain graphene with the interface layer component subtracted. **Inset**: The fitting of the interface layer spectrum to the 2 original spectra before the subtraction. **b**, Spectra of graphene of different G peak intensities and different amounts of strain as indicated by the blue-shifted 2D peaks. The spectra are taken from various samples. G peak intensity is a rough indication of number of layers. **Inset**: A zoomed in view of the same plot onto the D and G peaks. Notice that the D peak size is more or less the same for all the spectra despite their differences in number of layers and strain.

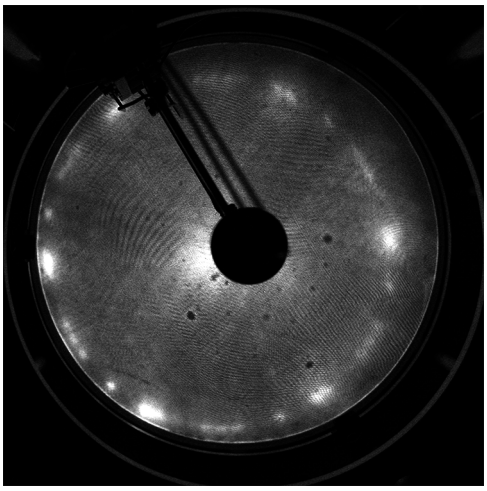

Figure 3.12: LEED pattern of a low-strain graphene sample on the 4H-SiC AC facet taken at 70V acceleration voltage, showing the rotated orientations of graphene.

layer persists after the first layer is grown, just like the buffer on the SiC(0001) face, and that the observed D peak and the G side-peak come from the interface layer underneath, not from the graphene layer on top.

To confirm this hypothesis, I matched the D-peak range spectra of the interface layer to those of highly-strained and less-strained graphene, and then subtracted the interface component from each spectrum. The procedure is similar to that used for SiC background subtraction illustrated in Figure 2.2**e**. As is shown in Figure 3.11**a**, the match is quite good, and the subtracted spectra only contain very small D peaks.

As another evidence, in Figure 3.11**b**, Raman spectra of different G peak integral intensities are plotted. The G peak integral intensity is a very reliable indicator of number of layers. We can see that as the G peak gets larger, the D peak intensity does not increase with increasing number of layers. This means that the D peak doesn't come from the graphene layers.

The LEED pattern of low-strain graphene indicates a rotated stacked graphene pattern, as shown in Figure 3.12. Unlike the LEED pattern on high-strain graphene (Figure 3.6**a**), the pattern in Figure 3.12 doesn't show the substrate's surface structure.

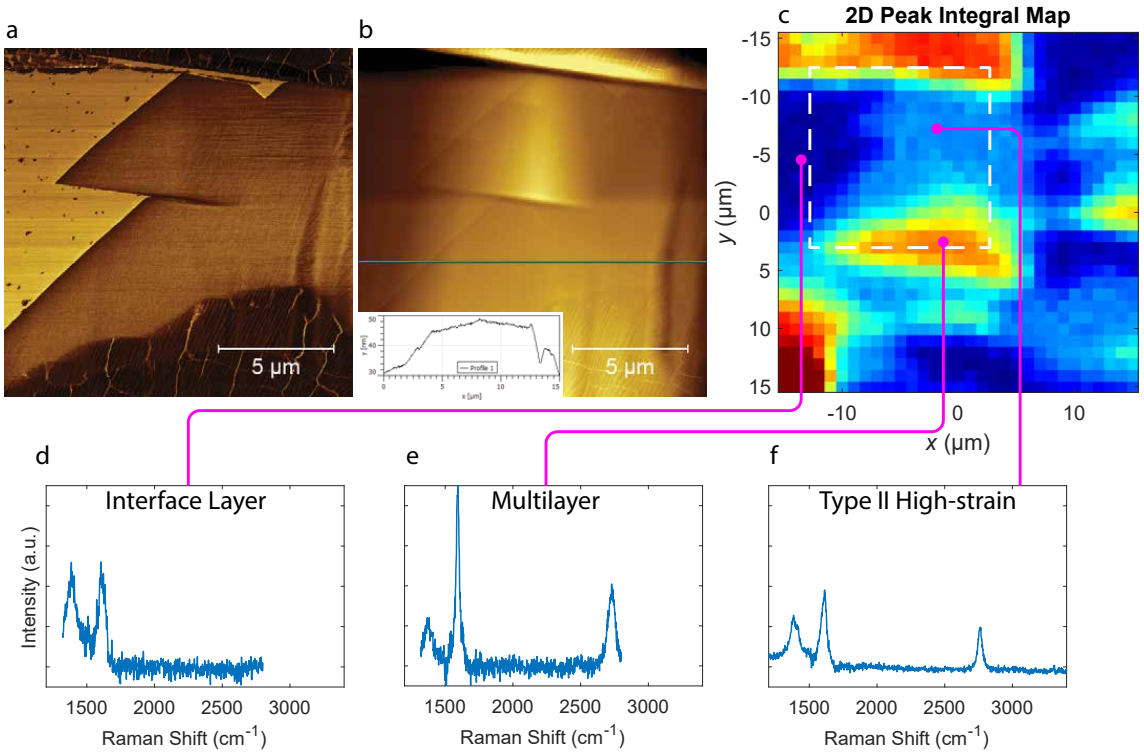

Figure 3.13: Topography, FFM and Raman mapping at the same location. **a**, FFM image that contains interface layer, type II high-strain graphene and multilayer graphene. **b**, The topography of the same region, with the line profile in the bottom left inset. **c**, A Raman spectroscopy 2D peak integrated intensity mapping at the same area. The dashed line square indicates the FFM scan region. **d**, **e** and **f**, Raman spectra of the interface layer, multilayer and type II high-strain graphene.

Multilayer graphene

Multilayer graphene (MLG) areas are identifiable by a large G peak in the Raman spectrum (Figure 3.11**b** blue line) and they appear much brighter in microscope with top light source or much darker with bottom light source as each graphene layer reflects significant amount of light [79].

A word on SiC surface morphology

Let us now take a look at Figure 3.13, which contains AFM topographe, FFM images and Raman spectrum mapping of the same area. The area contains type II high-strain graphene, interface layer, and multilayer graphene (see the Raman spectra in Figure 3.13**d**, **e** and **f**).

Note that the multilayer region at the bottom of the FFM image have larger and more

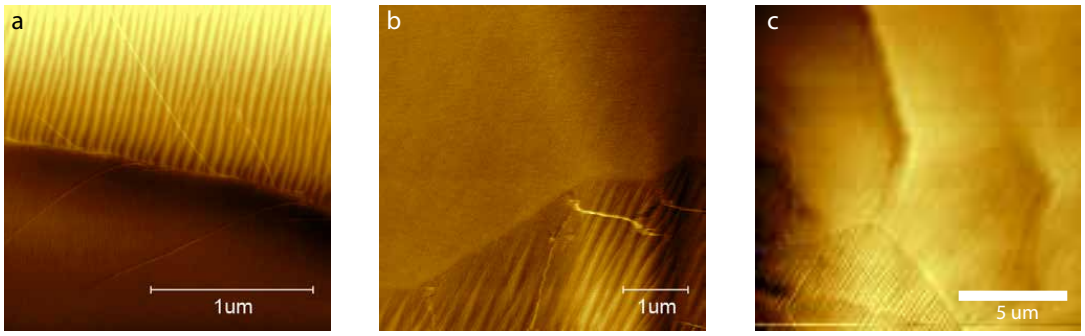

Figure 3.14: **a**, Low-strain monolayer graphene, **b**, type II high-strain graphene and **c**, type I high-strain graphene next to multilayer graphene. Note that in all cases, the terraces on the multilayer side are wider and more distinct.

distinct terraces while the SiC in the SLG and interface layer region do not have such structure. Upon a closer look, the SLG region actually has very small terraces. This phenomenon is seen in multiple samples and doesn't not seem to have an exception. The small terrace feature doesn't only apply to the type II high-strain graphene, but also has been seen in the cases of type I high-strain graphene and low-strain graphene (Figure 3.14).

Graphene layer relaxation

As mentioned previously, the first layer (interface layer) on this facet is highly strained and has no 2D peak in Raman, and the second layer may also be strained. It is similar to the situation of the buffer layer and SLG grown on the Si-face of SiC. And we found that, just as the buffer layer can be relaxed from the substrate by intercalation of hydrogen [80], the interface layer + SLG system can be relaxed from the substrate as well, through exposure to acetone and isopropyl alcohol consecutively. The mechanism is unclear and needs to be studied further. As discussed earlier, the highly strained SLG can be further categorized into 2 types, Type I and Type II, which differ from each other in their Raman spectra. Type I graphene relaxes through exposure to chemicals while Type II hasn't been found to become relaxed.

Quite interestingly, the 2D peak became asymmetric, with a obvious small shoulder on the left side. It turns out, that we can fit the peak with 4 Lorentzians (Figure 3.15**c**), a

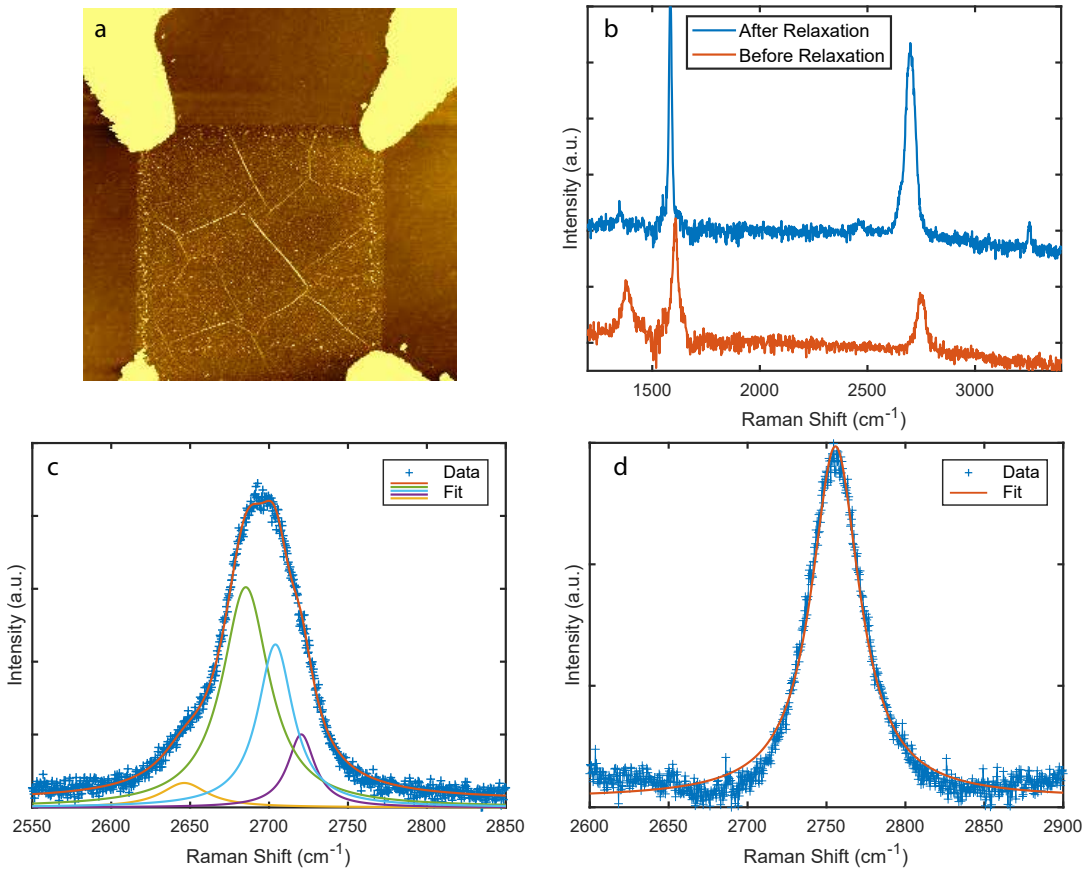

Figure 3.15: a, An AFM image showing a type I high-strain graphene after relaxation. Note that pleats show up in the film, likely due to the relaxation process. **b**, Spectra comparison of the same patch of graphene before and after it was released from the substrate. Note that the D peak decreased significantly in size, and the blue-shift amounts of the G and 2D peaks were both reduced. **c**, Spectrum of the 2D peak of the same sample with higher resolution. It can be fitted with 4 Lorentzian components. **d**, Spectrum of a strained graphene 2D peak. Unlike the peak in **c**, this peak is symmetric and can be fitted with a single Lorentzian.

criterion for bilayer graphene [55]. That means that the interface layer underneath the SLG is indeed structurally a graphene layer, and it is strongly influenced by the substrate.

Pre-growth patterning

Early on we found that the surface scratches and holes could initiate growth. In a lot of cases, graphene growth is denser near the large scratches, where graphene patches seem to stem from the scratches. On the other hand, a nearly defect-free surface will see growth occurring randomly and the density of SLG patches is not enough to cover the surface without multilayer growth. For example, as shown in Figure 3.5**a**, some MLG already

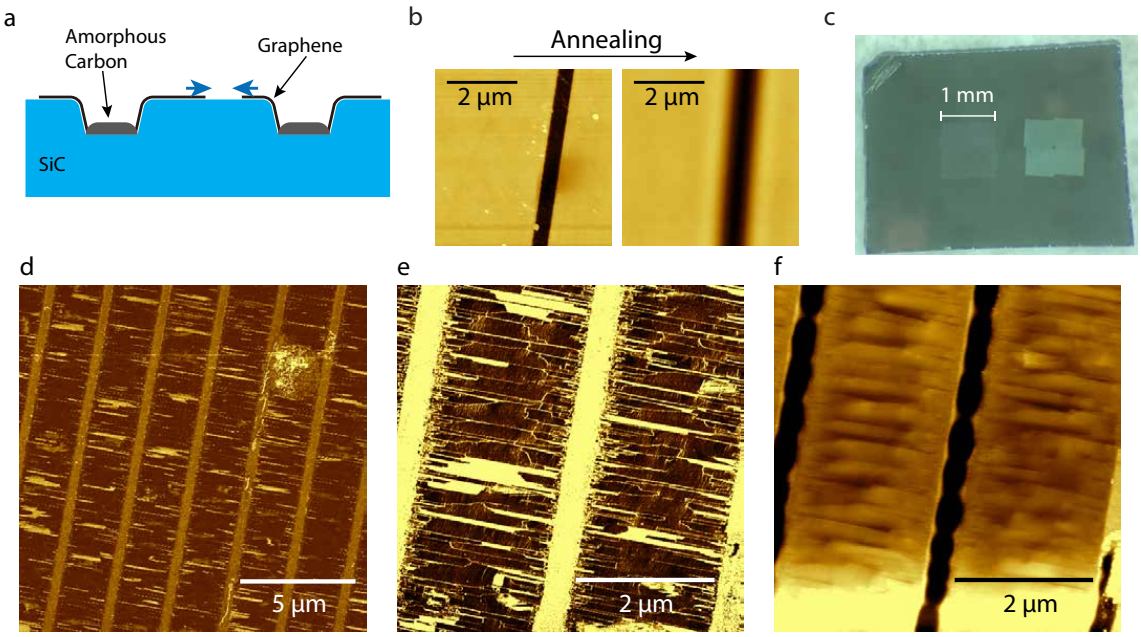

Figure 3.16: **a**, An illustration of pre-growth patterned seeding trenches. We etch trenches in SiC and fill it with amorphous carbon (aC). The purpose of aC is to pin the step flow and prevent the trenches from being flattened out by annealing. **b**, Trenches without aC deposition gets flattened/smoothed by high temperature annealing and cannot act as growth seeds. **c**, Pre-growth patterning allows homogeneous growth over a large area. **d**, FFM of the growth seeded by the trenches. **e** and **f** FFM and topography images of a smaller area in **d**. The growth has very high density of individual patches with very small size for each patch, in contrast with the sparse and large patches seen in e.g. Figure 3.5**a**.

starts to grow while only a small portion of the surface is covered by SLG. Thus, we had the idea to pattern and etch trenches into SiC pre-growth and use these as growth seeds.

The process is illustrated in Figure 3.16**a**. We etch trenches into SiC substrate and fill them with amorphous carbon (aC). The aC will pin the step flow and prevent the trenches from being flattened by high temperature. This effect of aC was discussed by Palmer et. al [74]. After growth, these patterned trenches seed graphene growth and form a large area of homogeneously grown densely packed graphene SLG patches.

This type of large area growth can be used for large area characterization probes such as LEED, ARPES and spectroscopy. Indeed, the LEED, ARPES and Landau level spectroscopy results presented in Figure 3.6**a** were all taken on samples thus prepared.

Graphene on the 4H-AC 30° facet

In addition to the 37° facet angle, 30° was also investigated. The researches previously done on AC SW-GNR's indicate that this is also a stable facet [47, 48]. The growth is similar to that on the 37° facet. The graphene is compressively strained, with slightly lower strain than that on the 37° facet, as indicated by the blue-shifted 2D peak at 2737 cm^{-1} (Figure 3.17**a**). There is a large D peak, which may be associated from the interface layer (Figure 3.17**b**). As the FFM and topography images shown in Figures 3.17**c**, **d** suggest, the graphene patches are shaped in partly trapezoidal stripes.

3.3.2 Graphene on the 4H-SiC ZZ Facet

Giuseppe Nicotra et al [81] reported transmission electron microscopy study on SW-GNR's on the 4H-SiC ZZ facets and found various facet angles. Statistics of these different facet angles is provided in their report and a majority of samples show facets at angles of $27°$ and $29°$. Knowing this, we studied samples cut at an angle of $30°$.

The graphene grows on this facet in the shape of long patches running along the SiC $\langle 1\bar{1}00\rangle$ direction, and is compressively strained (Figure 3.18). There also is the interface

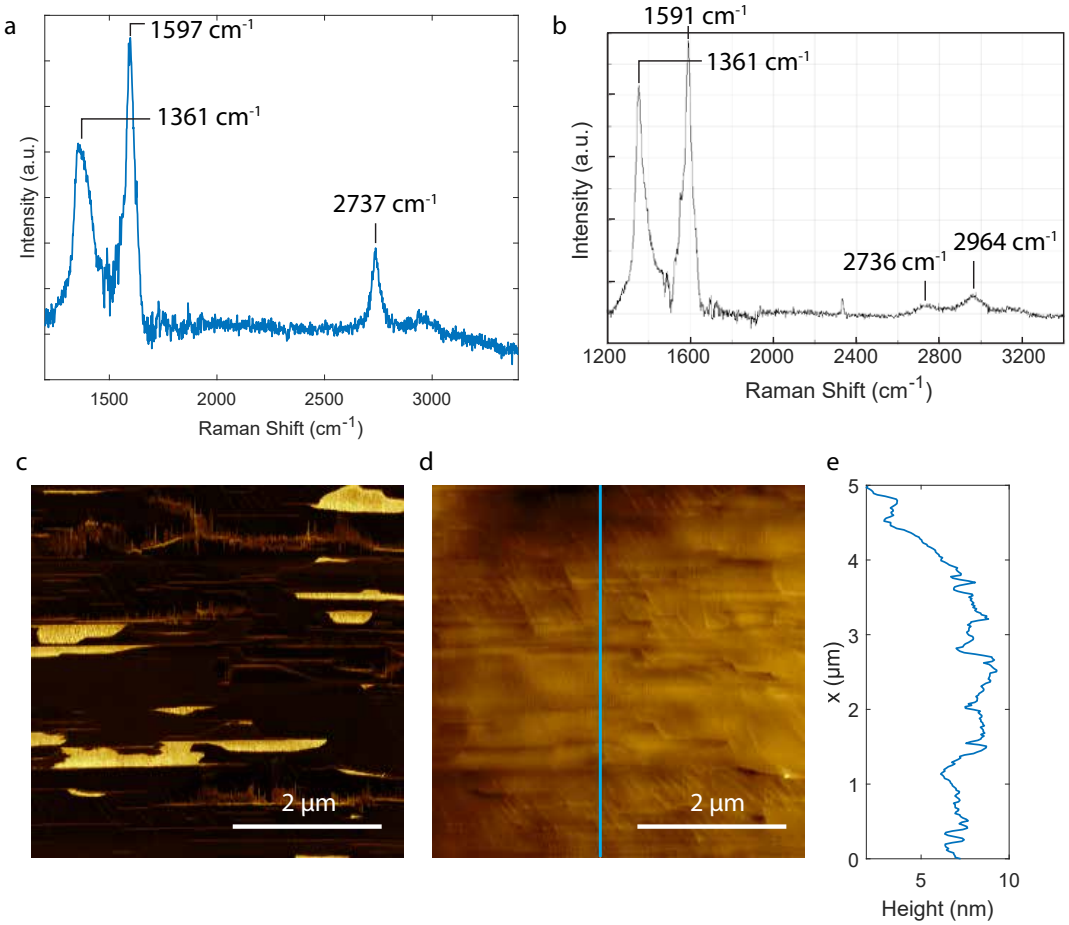

Figure 3.17: Graphene and interface layer on the 4H-SiC AC 30° facet. **a**, Raman spectrum of the graphene. **b**, Raman spectrum of the interface layer. **c**, FFM and **d**, topography of the graphene on this facet. **e**, The height profile of the line scan shown in **d**.

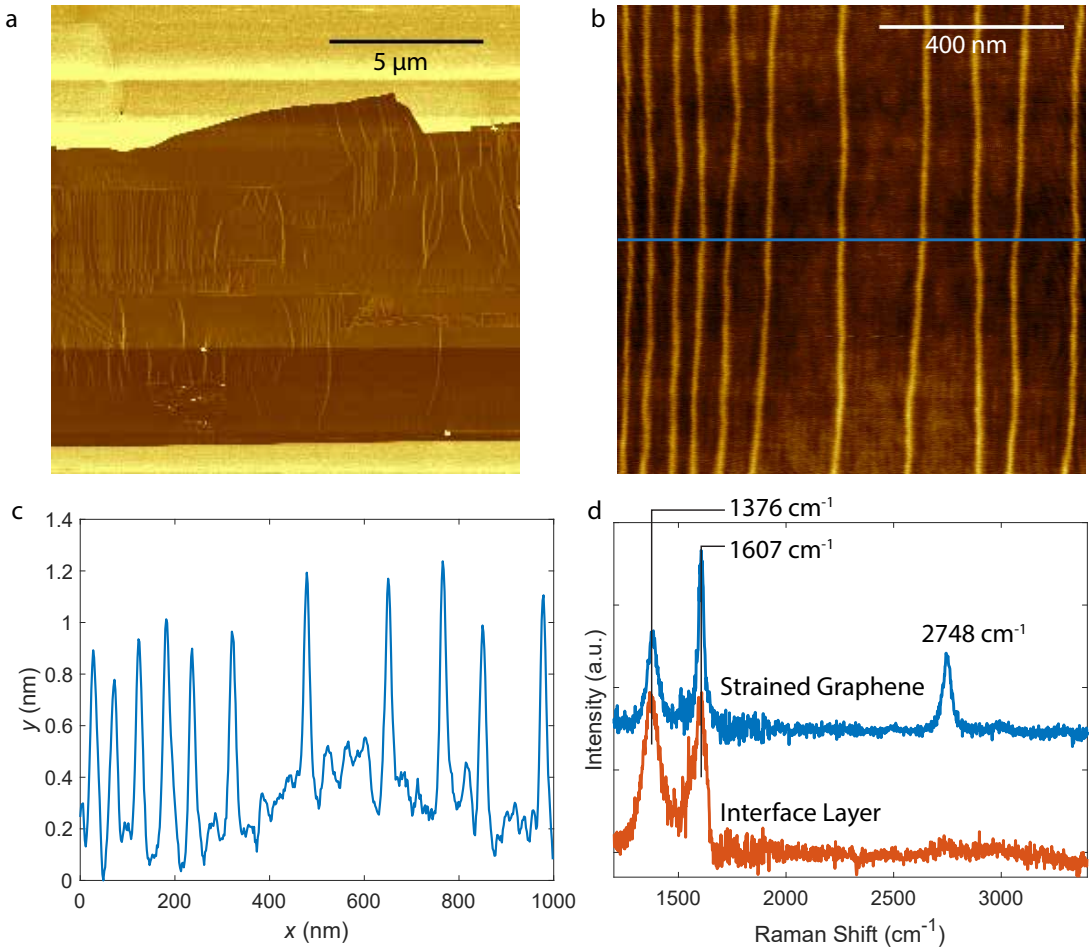

Figure 3.18: **a**, Frictional force microscopy image of a patch of graphene grown on the SiC ZZ face. The darker region is the graphene. The bright region is interface layer. The lines running across the graphene area are pleats. **b**, A small area topography image taken in the graphene region, showing pleats that run perpendicular to the $\langle 1\bar{1}00 \rangle$ direction (AC direction). **c**, The topography profile corresponding to the line in **b**. **d**, Spectra of the strained graphene layer and the interface layer.

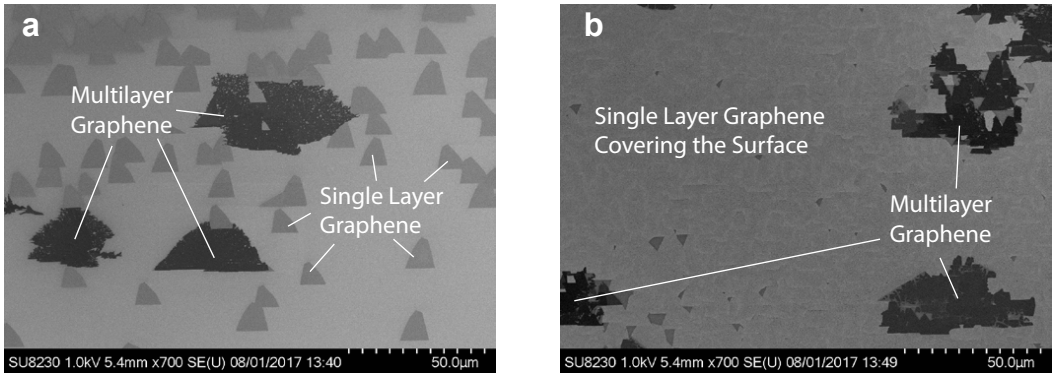

Figure 3.19: **a**, SEM image showing graphene growth in triangular shapes on the 4H-SiC C-side ZZ facet. **b**, SEM image showing triangular shaped graphene patches joind together to form large area of graphene monolayer.

layer, as determined by showing only D and G peaks in its Raman spectrum (Figure 3.18**d**). Interestingly, the graphene on this surface has pleats, usually an indication of the release of strain. Despite these pleats, the graphene is still compressively strained as indicated by the 2D peak which is blue-shifted to $\sim 2748\,\mathrm{cm}^{-1}$. The pleats mainly run perpendicular to the SiC$\langle 1\bar{1}00\rangle$ direction, indicating an asymmetry of strain in the film.

3.3.3 Graphene on the 4H-SiC C-Side ZZ Facet

On the 4H-SiC C-side ZZ facet, graphene growth is vastly different from that on the faces towards Si face. Instead of elongated patches, triangular patches of graphene grow on this face, as can be seen in Figure 3.19**a**. We also see that these triangles are similar in size and share the same orientation with their bottom edges running along the SiC$\langle\bar{1}100\rangle$ direction. This implies that they have the same crystal orientation. Interestingly, as growth continues, these triangles merge together to form a larger area of graphene but with little over-growth (Figure 3.19**b**). Steps are found at the edges of triangles. The step heights varies around 1.5 nm (Figure 3.20**a**).

In Figure 3.21, Raman spectroscopy results are shown. Triangular shape can be easily seen in the 2D peak area map in Figure 3.21**b Inset**. Raman spectrum in such a graphene area possesses a single high 2D peak and no D peak (Figure 3.21**a**). Also in the line map

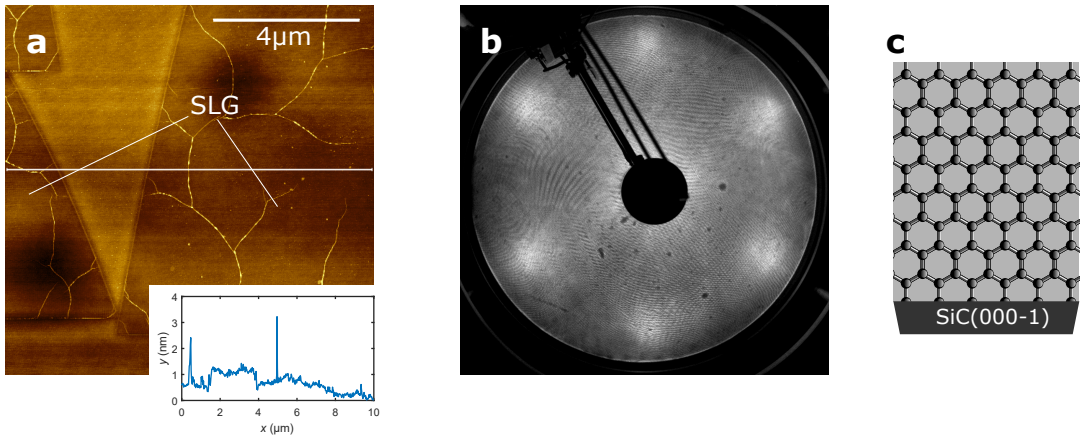

Figure 3.20: AFM images and LEED pattern of graphene on the 4H-SiC C-side ZZ facet. **a**, AFM image showing graphene patches. Inset: topography profile corresponding to the line in the AFM image. The graphene area is lower than the non-graphene area by about 6Å. **b**, LEED image of the graphene showing broad peaks. Broad diffraction peaks indicate disorder in the real space. Since the Raman spectra show very small amount to disorder (Figure 3.21), the disorder seen in LEED might be due to corrugation of the graphene film on the surface. The hexagonal orientation of the peaks proves that the growth is epitaxial and the graphene lattice orientation is indicated in **c**.

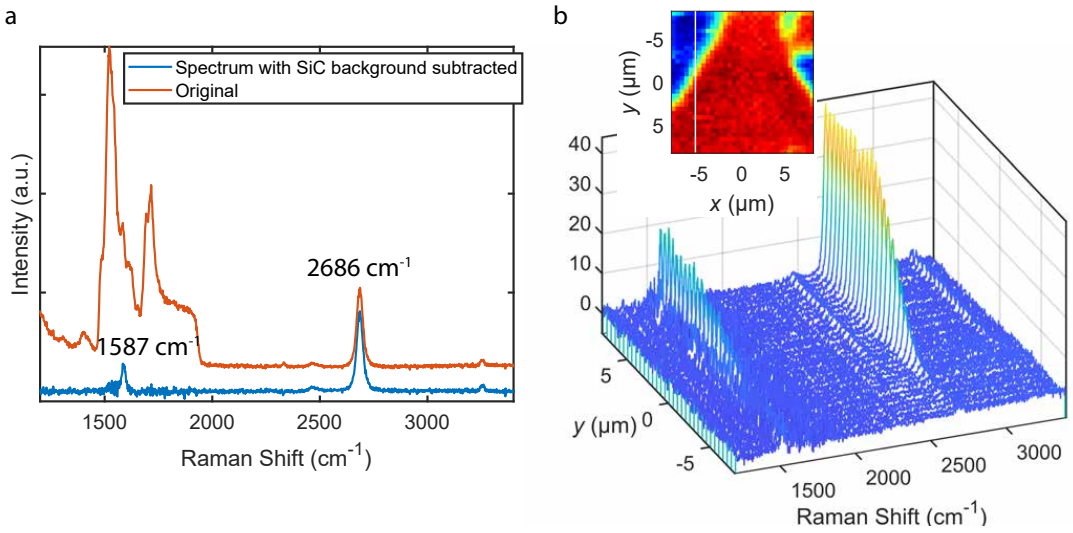

Figure 3.21: **a**, A typical Raman spectrum of the graphene on the 4H-SiC C-side ZZ facet. The spectrum reflects almost pristine graphene features: a high and thin 2D peak, and a non-existent D peak. **b**, A line map of spectra showing the uniformity of the film. Inset: the 2D peak area of a spectroscopy map; the vertical line indicates the line map of from which **b** is taken.

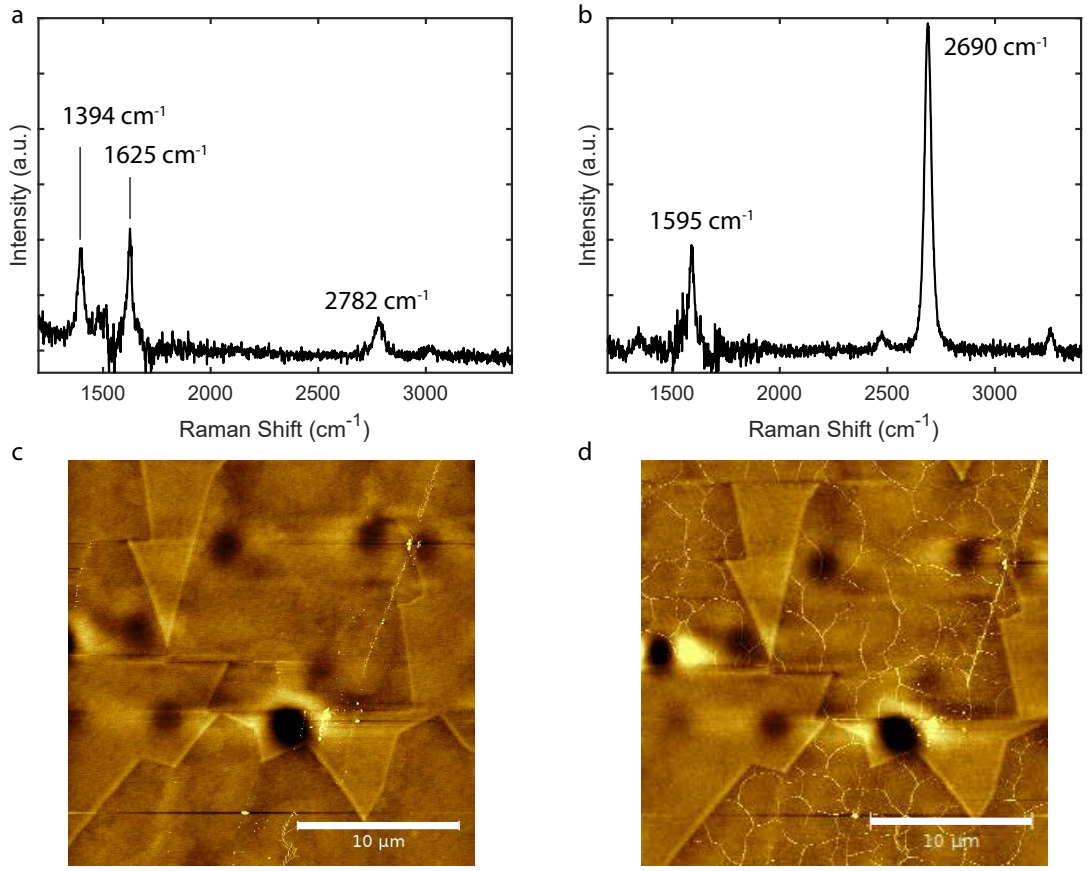

Figure 3.22: The relaxation of graphene on the 4H-SiC ZZ C-side facet. **a**, Raman spectrum of the graphene on the 4H-SiC ZZ C-side facet taken immediately after the sample was exposed in air. The strong blue-shift of the 2D peak indicates a large compressive strain in the film. **b**, Raman spectrum of the same sample after one day exposure to air. The strain is released. **c**, **d**, AFM images of the same sample at the same exact place, just after exposure to air and on the next day, respectively. Pleats appeared only in the latter, confirming the releasing of strain observed in **a** and **b**.

spectroscopy plot in Figure 3.21**b**, we can see the Raman spectra across such a region are quite uniform in terms of peak positions and intensities. Notably, outside the graphene triangles Raman spectroscopy doesn't show any graphitic interface layer as seen on Si-side facets.

The graphene on this facet is initially compressively strained. The exposure to air caused the strained graphene to relax. In Figure 3.21c and d, two spectra taken at the same position but different times are shown. We notice that a few hours after the graphene growth, the spectrum indicates a highly strained graphene film, with the G peak at 1625 cm^{-1} and 2D peak at 2782 cm^{-1} (Fig. 3.22**a**). The D peak is also present at 1392 cm^{-1}, half the

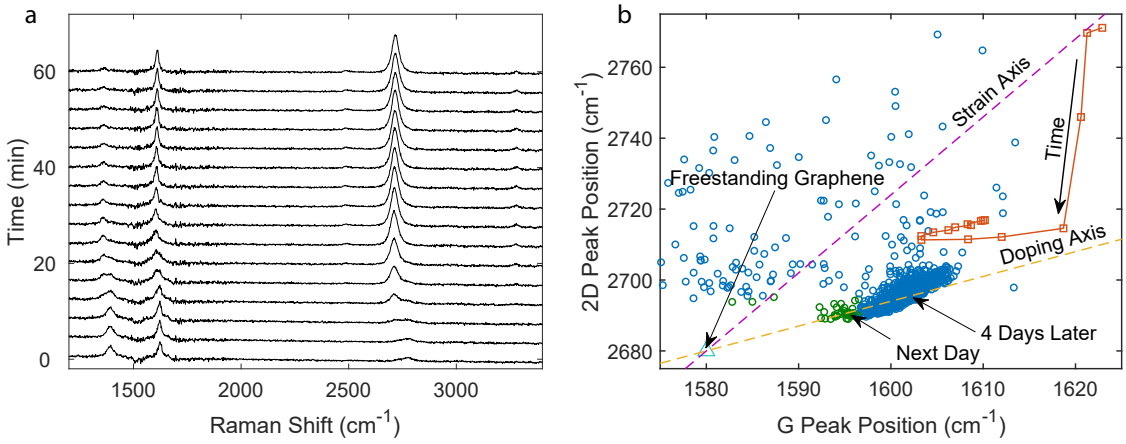

Figure 3.23: a, A sequence of spectra taken apart from each other by 10 min intervals, showing the evolution of the three peaks: the blue-shift of the 2D and the G peaks decreased, while the D peak gradually disappeared. **b**, Relation between the positions of the G and the 2D peaks, evolving over time. The red line with square marks are positions from **a**. The rest of the data are from 2 spectroscopy maps done a few days later. The dashed lines indicate the 2 axes corresponding to the blue-shift caused by doping and strain, respectively [77]. The initial blue-shift thus is clearly due to the strain but not doping.

value of 2D peak, as expected. This matching of D and 2D peak positions means that this D peak comes from the same film as 2D peak, not from some carbon-rich layer underneath. After one day, however, the Raman spectrum at the same location turned into one that is very close to a free-standing graphene spectrum (Figure 3.22**b**). The G peak is at 1595 cm^{-1} and 2D peak at 2690 cm^{-1}. D peak is barely seen. Such transition is not limited to only this spot, but quite universal over the sample. Topographically, the originally strained layer has no pleats (Figure 3.22**c**). After one day in air, pleats can be seen in the films, an indication of the release of compressive strain.

The evolution of G and 2D peak positions with time is plotted in Figure 3.23. Notably, in Figure 3.23**b**, we can see the blue-shift was originally due to the strain, but a few days later came from doping.

The film relaxation process can be prevented or slowed down by a protection Al_2O_3 layer on top of it.

Both Raman spectra and AFM images confirm that the graphene film underwent some sort of relaxation transition during the time of about one night. A strongly strained film turned into a relaxed one. Unless otherwise stated, the results discussed in this section are

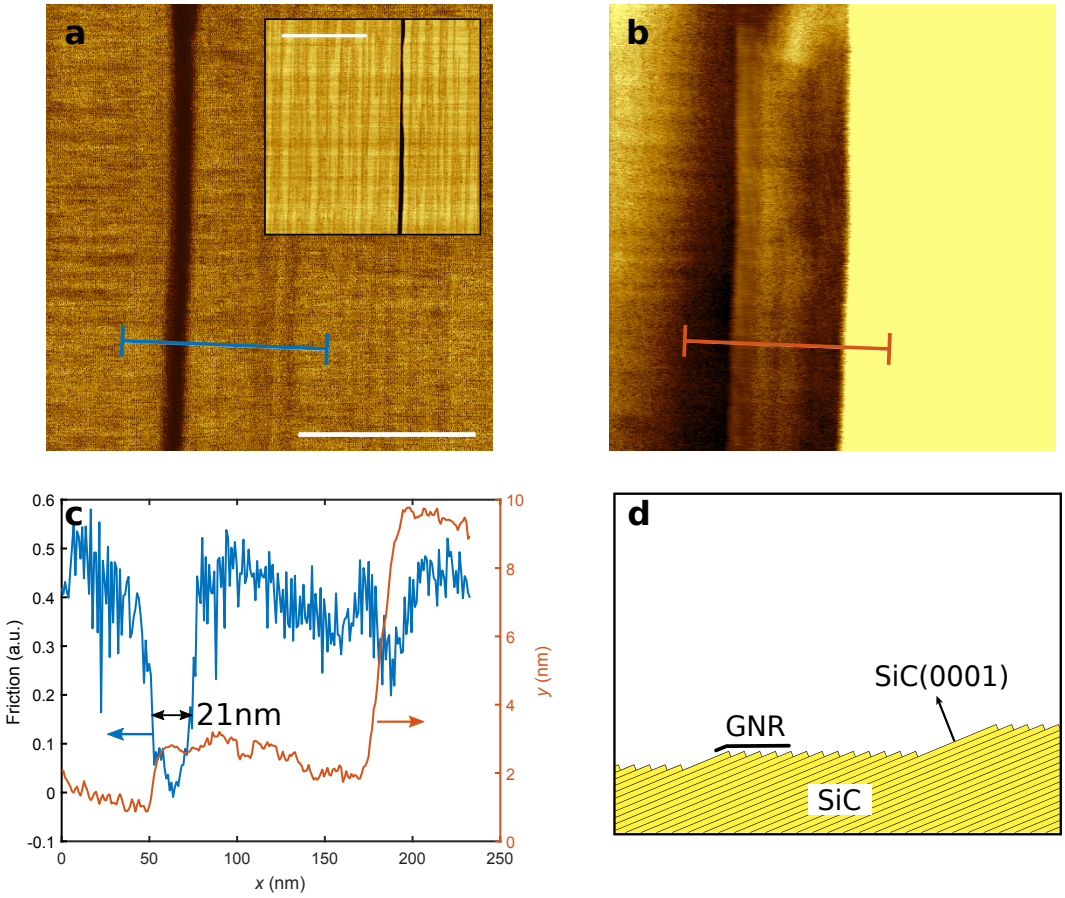

Figure 3.24: a, Frictional force microscopy image of a GNR on the 6H-SiC ZZ facet, at an angle of 22° from the Si-face and **b**, the corresponding topography image (scale bar: 200 nm). The inset in (**a**) is a larger scale frictional force microscopy image showing a straight continuous ribbon at least 5 µm long (scale bar: 2 µm). **c**, The frictional force and topography profiles along the lines in (**a**) and (**b**). We can see that the GNR lies on the 6H-SiC ZZ facet, right next to a step consisting of the 6H-SiC(0001) facet. d, An illustration of the growth of GNR next to a step.

from the relaxed film, including Figure 3.19.

3.3.4 Graphene Nanoribbons Growth on Non-polar Facets

It turns out, interestingly, that in some conditions the graphene growth appears to be highly anisotropic in different directions, leading to patches with very high aspect ratios, sometimes even nanoribbons.

I found such type of growth behavior in two of the facets investigated: 6H-SiC ZZ 22° facet and 4H-SiC AC 37° facet.

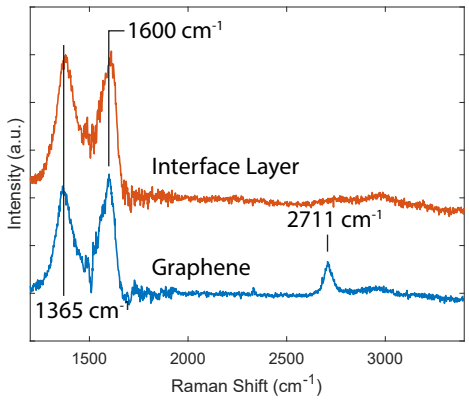

Figure 3.25: Raman spectrum of the graphene and graphitic interface layer grown on the 6H-SiC ZZ 22° facet.

Figure 3.24 shows the FFM image of the nanoribbon growth on the 6H-SiC ZZ 22° facet. We can see a very narrow and straight ribbon. The profile of the topography indicates that the steps are at around 22° relative to the cut facet. That mean the surface is occasionally restructured into small SiC(0001) steps. We find graphene nanoribbons grown next to the SiC(0001) steps. This structure is illustrated in the schematics shown in Figure 3.24d. Note that the width of this ribbon is only 21 nm while the length is more than 5 µm. The Raman spectrum taken of graphene on this facet is shown in Figure 3.25. The graphene is compressively strained, and also has a large D peak. The D peak can also be attributed to a graphitic interface layer also shown in the figure.

Similar growth pattern was found on the 4H-SiC AC 37° facet. Figure 3.26 shows a FFM image of such a ribbon. The width of the ribbons on this sample is generally larger than that on the 6H-SiC ZZ facet. The surface morphology is quite different from that of the 6H-SiC ZZ facet (Figure 3.24). As we can see, the topography image and the corresponding profile show a wavy surface, with no sign of the SiC(0001) facets. However, the error signal image from the same FFM scan (Figure 3.26**d**) indicates the seemingly continuous surface underneath the graphene area in fact consists of very dense arrays of terraces.

The capability of growing nanoribbons directly on non-polar facets brings the advantage in doing 1D transport experiments without having to cause roughened edge due to the etching process [82], just like SW-GNRs.

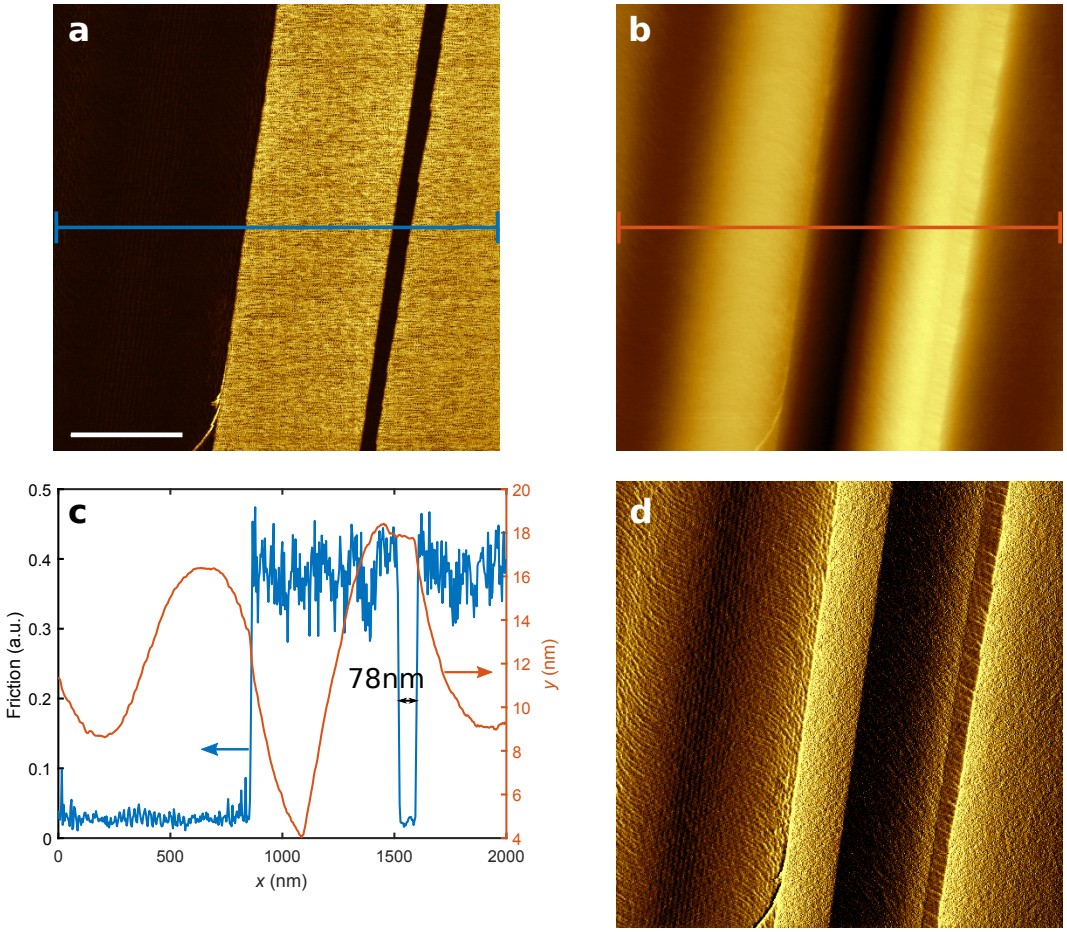

Figure 3.26: **a**, Frictional force microscopy image of a GNR grown on the 4H-SiC AC facet at an angle of 37° with respect to the Si-face and **b**, the corresponding topography image (scale bar: 500 nm). **c**, The profiles of the frictional force and the topography, along the lines shown in **a** and **b**. **d**, Error signal image showing the dense array of terraces that constitutes the wavy surface seen in **b**.

CHAPTER 4

TRANSPORT MEASUREMENTS

In this chapter, measurements and analyses are presented on the transport of the low-strain graphene samples on the 4H-SiC AC 37° facet.

4.1 Sample TMYH30 Hall Bar

Sample TMYH30 is a 4H-SiC AC 37° facet sample, taken from a doped SiC wafer cut and polished at TICNN. This sample was annealed in Ar atmosphere at 1550 °C for 1800s to flatten the surface and then at 1650 °C for 7200s (also in Ar) for graphene growth. Raman spectroscopy indicates low strain graphene. There is a significant D peak that is associated with the interface layer as was discussed in Subsection 3.3.1 and Figure 3.11. Thus, the D peak doesn't mean the graphene is disordered. The LEED pattern suggests a rotated stacked layer (Figure 3.12). Thus, the orientation of the graphene is not certain. The graphene is low-strain SLG according to the Raman spectrum (Figure 4.1**a**). The device fabrication process illustrated in Figure 2.9 was used to produce Hall bars on this sample.

As shown in Figure 4.1**c**, the device is contacted by Pd+Au electrodes and covered by

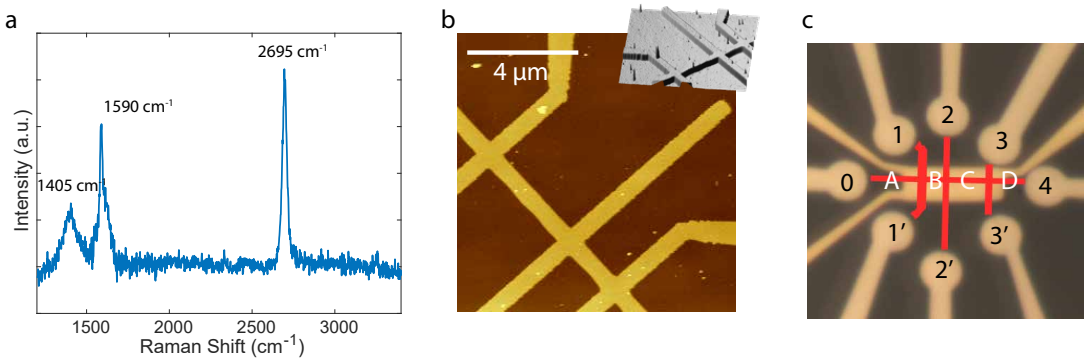

Figure 4.1: a, Raman spectrum of sample TMYH30, indicating a low-strain graphene. **b**, Aluminum coated Hall bar device. Inset: 3D rendering of the AFM image. **c**, Optical microscope image of the final device.

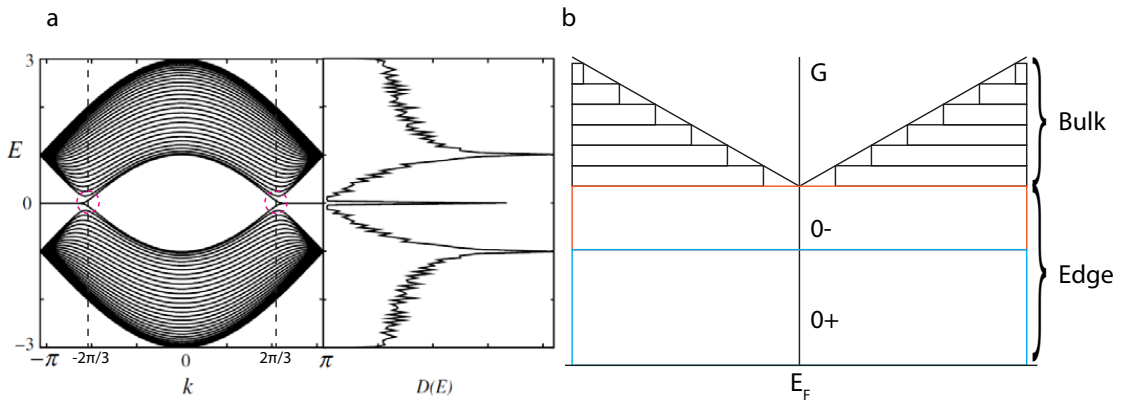

Figure 4.2: a, The band structure and DOS of a ZZ GNR. The wave vector k is measured in the unit of $1/a$. We speculate that the transport phenomenon observed here is due to the edge states located near the K/K' points which are circled out. From Ref. [20]. **b**, The proposed model of transport in the Hall bar. The model is based on that from Ref. [4].

a gate made of 30 nm of Al_2O_3 dielectric and Pd+Au on top. The Hall bar consists of 3 transverse arms and in total has 8 leads which are labeled as shown in Figure 4.1**c**. We use the following notation for the resistance measurements:

$$R_{ij,kl} = V_{kl}/I_{ij}, \tag{4.1}$$

where I_{ij} is the current injected from contact i to contact j and V_{kl} is the voltage measured from contact k to contact l.

Figure 4.2 is a zoomed-in picture of the ZZ band structure calculated by the tight-binding model. As we can see there is a large density of states associated with a flat band at zero energy. This band is dubbed the 0th band. We believe the transport phenomenon observed here is due to the edge states near the K/K' ($k = \pm 2\pi/3a$) points.

The transport in this sample can be explained by a transport model illustrated in Figure 4.2: edge conduction and bulk conduction. According to the Landauer formula (Eq. 1.4), the transport in a 1D device can be described by the transmissions in multiple channels.

Let's separate the edge band from the other bulk bands:

$$G = G_B + G_E = \sum_{\text{bulk}} T_B e^2/h + \sum_{\text{edge}} T_E e^2/h, \tag{4.2}$$

where the edge conductance G_E has two components: 0^- and 0^+. The energy levels in a graphene ribbon with length L and width W are [4]

$$E_{n,m} = \pm \hbar c^* \sqrt{(n\pi/W)^2 + (m\pi/L)^2}. \tag{4.3}$$

For a ribbon with width $0.7\,\mu\text{m}$, the first bulk band's energy minimum is 3 meV which is equivalent to 34K. This means that below this temperature at CNP, the bulk bands' contribution to the conductance can be neglected.

Recall from Chapter 1 and Eq. 1.7 that the resistance is proportional to the length of the segment in the diffusive regime, or constant plus a small linear term with respect to the length in the ballistic regime. As will be shown later in this section, the transport measurements are consistent with the bulk transport being in the diffusive regime and the edge states being ballistic.

The gate voltage V_G is used to adjust the charge density n_s in the sample. The sample is electron doped so a negative gate voltage was used to bring the Fermi level to CNP. The V_G value shown in the figures are offset by the gate votlage of CNP:$V'_G = V_G - V_{G,CNP}$. Specifically, more bulk states are filled up as V_G moves away from the charge neutrality point (CNP). Thus, the conductance is a function of V_G in terms of the bulk conductance portion, while the edge conduction stays constant (see also Figure 4.2**b**). We have

$$G(V_G) = G_B(V_G) + G_E. \tag{4.4}$$

Figure 4.3 shows the conductance of segment D (see Figure 4.1**c** for the labeling) of the Hall bar with respect to the applied magnetic field. The resistance of this segment is

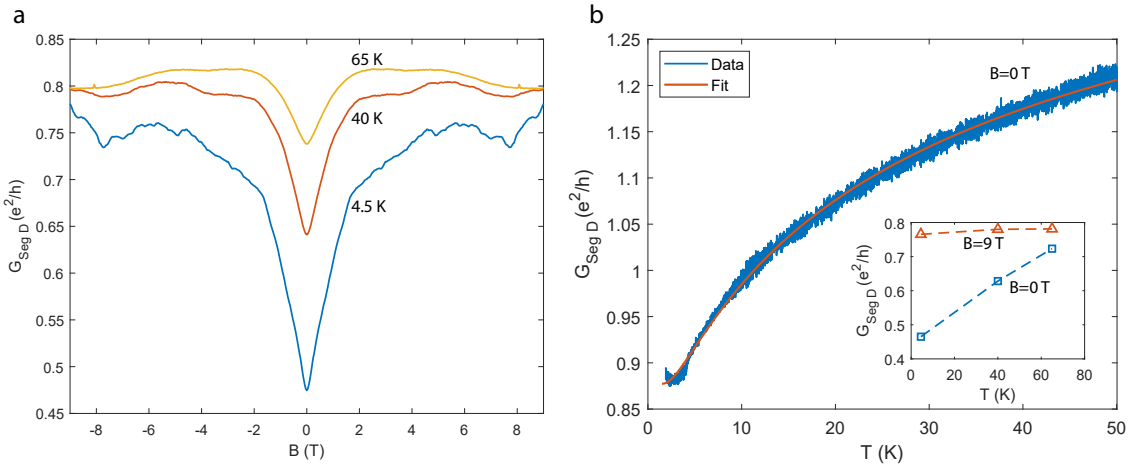

Figure 4.3: a, A positive magneto-conductance measured at CNP results in the "V" shape that was seen in nanoribbons and nanotubes. The large width of the "V" cannot be explained by weak (anti)localization effect. **b**, The temperature dependence plot at $V_G' = 0.71\,\mathrm{V}$ ($\sim 7 \times 10^{11}\,\mathrm{cm}^{-2}$ electron doped) reveals a plateau at about $0.85e^2/h$. The data is fitted by Eq. 4.8. Inset: the conductance vs. temperature at CNP as extracted from **a** at $B = 0\,\mathrm{T}$ and $B = 9\,\mathrm{T}$.

calculated by taking the average of the voltages on two arms (3 and 3') on both sides of the segment:

$$G_{\text{seg D}} = \left(\frac{R_{40,43} + R_{40,43'}}{2} \right)^{-1}. \tag{4.5}$$

The prominent feature seen in this figure is the "V" shaped positive magneto-conductance. Similar features have been long observed in CNT's and GNR's [4, 83, 84]. It is suspected that a magnetically induced transport channel is involved in this "V" shaped magneto-conductance.

Can we attribute the positive magneto-conductance to weak localization (WL) or weak antilocalization (WAL)? In the WL regime, quantum coherence increases the probability that an electron gets reflected. A magnetic field that destroys the phase coherence suppresses the phenomenon. In graphene, the suppression of electron backscattering due to the pseudospin conservation called weak antilocalization (WAL) results in a weak field negative magneto-conductance [85]. This phenomenon was observed in epigraphene and was an evidence of the chiral electrons [86]. In our sample, the conductance increases up

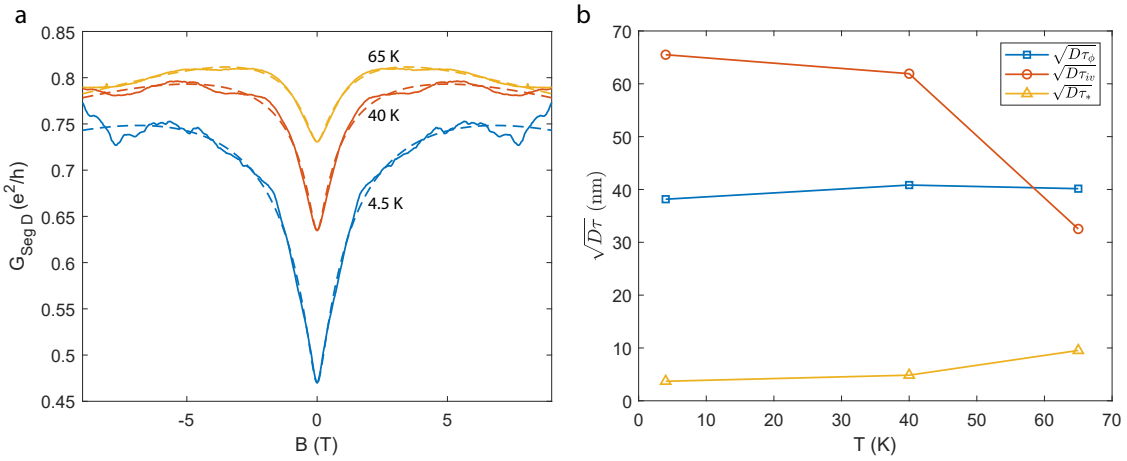

Figure 4.4: a, The magneto-conductance data fitted with WAL (Eq. 4.7). **b**, The three fitting parameters with respect to temperature.

to a magnetic field of about 2-3T. This means a very short phase-coherent length:

$$L_\phi = \sqrt{\frac{h}{eB_c}} \approx 40\,\mathrm{nm}, \tag{4.6}$$

where $B_c \approx 2\,\mathrm{T}$ is the critical magnetic field to destroy the coherent back scattering [53]. Quantitatively, we can adopt the WAL formula [85, 86]

$$\rho(B) - \rho(0) = \\ -\frac{e^2\rho^2}{\pi h}\left[F\left(\frac{2\tau_\phi}{\tau_B}\right) - F\left(\frac{2}{\tau_B(\tau_\phi^{-1} + 2\tau_{iv}^{-1})}\right) - 2F\left(\frac{2}{\tau_B(\tau_\phi^{-1} + \tau_{iv}^{-1} + \tau_*^{-1})}\right)\right], \\ F(z) = \ln z + \Psi\left(1/2 + 1/z\right),\ \tau_B = \frac{\hbar}{2eDB}, \tag{4.7}$$

where $\Psi(x)$ is the digamma function and, D is the diffusion constant for the electrons, τ_ϕ is the phase relaxation time and τ_{iv} is the inter-valley relaxation time and $\tau_*^{-1} = \tau_w^{-1} + \tau_z^{-1}$ is the sum of the intra-valley scattering and the trigonal warping induced relaxation rate. Using this equation to fit the magneto-conductance in Figure 4.3, we get the fit shown as dashed lines in Figure 4.4**a**. The fitting parameters with respect to the temperature is plotted in Figure 4.4**b**. The phase coherent length $\sqrt{D\tau_\phi}$ is indeed about 40 nm.

However, multiple evidences indicate WAL is not the cause of the positive magneto-conductance. As noted in Ref. [85], when $\tau_{iv} > \tau_\phi > \tau_*$, which is the case for the parameters found at 40K and 4.5K (Figure 4.4**b**), the MR displays neither WL nor WAL behavior. Also, as we will see in Section 4.2, the weak localization peak is missing in the Corbino ring measurements. What's more, the positive magneto-conductance in various GNR studies cannot be explained by weak localization [4, 83, 84]. All these evidences point to an origin for the positive magneto-conductance from the edge conduction. Furthermore, the conductance as a function of temperature fit very well with the model described in Ref. [4], (see the following discussion on Figure 4.3**b** and Ref. [4]), which doesn't involve weak localization. In summary, weak localization, though very tempting, is likely not the cause of the positive magneto-conductance observed in our sample.

Weak (anti)localization cannot explain the positive magneto-conductance ("V" shape). While the origin of this "V" shape that has been observed in various carbon systems [4, 83, 84] is still unclear, we speculate that the magnetic field has a similar effect as the temperature. Notably, the magnitude of the "V" shape decreases with increasing temperature (Figure 4.3**a**). Also, at high magnetic fields, the temperature activation phenomenon is weaker than at low field (Figure 4.3**b** inset).

The temperature dependent conductance measurement is very reminiscent of the result from Ref. [4]. To illustrate the similarity, we can use the model from Ref. [4] to fit the temperature data:

$$G(T) = \alpha \frac{e^2}{h} \left(1 + \beta \exp\left[-\left(T^*/(T - T_0)\right)^{1/2}\right]\right), \tag{4.8}$$

to fit the data we have. As is shown in Figure 4.3**b**, the model fits very well, with $\alpha = 0.88$, $\beta = 0.86$, $T^* = 33.29\,\mathrm{K}$, and $T_0 = 1.17\,\mathrm{K}$.

Eq. 4.8 resembles the Mott's variable range hopping (but originates from a different source) in 1D case [87] in parallel to a constant conductance. As discussed in Section

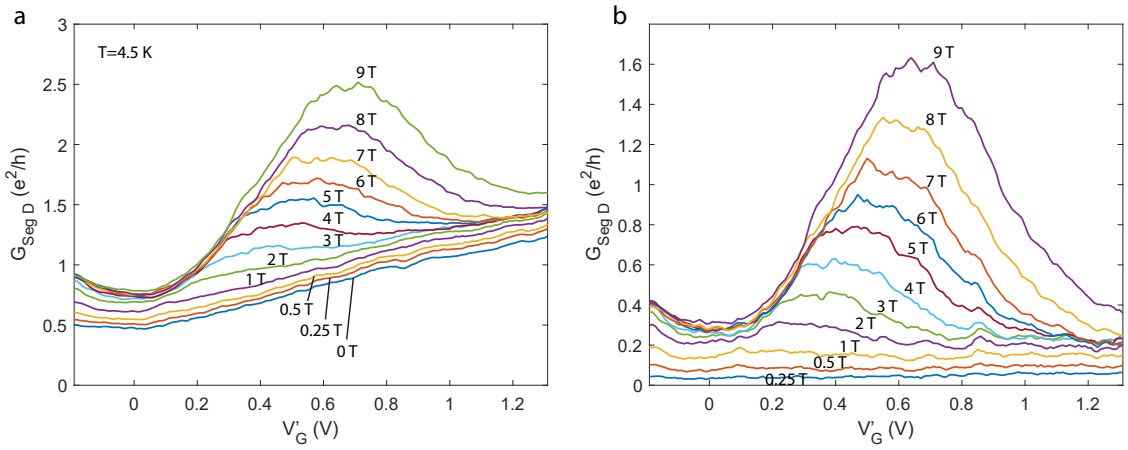

Figure 4.5: a, Vg sweeps at various magnetic fields from 0T to 9T at $T = 4.5$K. **b**, The same conductance with a baseline from 0T subtracted.

1.2.4, this formula indicates a thermally activated transport channel. The power $1/2$ in the $(T^*/(T - T_0))^{1/2}$ term is related with the dimension. Specifically, a power of $1/(d + 1)$ is present for d-dimension variable range hopping. d values with 0 to 2 are all tried and the 1-dimension case fits the best. Remarkably, the constant conductance channel can be readily seen in Figure 4.3**b** as the conductance reaches a plateau at $T < 4$K, which was not seen in Ref. [4]. In Ref. [4], this formula is attributed to the constant 0^+ channel conductance plus the 0^- conductance due to thermally activated longitudinal modes (i.e. $E_{1,0}$ in Eq. 4.3). Using the arguments made in that reference, we find a charge carrier lifetime $\tau = 4\pi\hbar/k_B T^* = 2.9 \times 10^{-12} s \approx 0.8L/c^*$. This means that the carrier lifetime is on the order of the transit time just like the case in Ref. [4].

These measurements point to a transport model for the edge states that consists of two components 0^+ and 0^- (see Figure 4.2). The plateau indicates the first channel that doesn't change with temperature. On top of this channel, there is another channel that is activated by temperature or by magnetic field. Note, that at high magnetic field, the second channel doesn't vary with temperature as much (Figure 4.3**b** inset).

With this model in mind, let's examine the conductance vs. gate voltage plot as shown in Figure 4.5. The turn-on of the 0^- channel as magnetic field increases is visible as a constant offset between the different lines shown in Figure 4.5**a**. Note that the magneto-

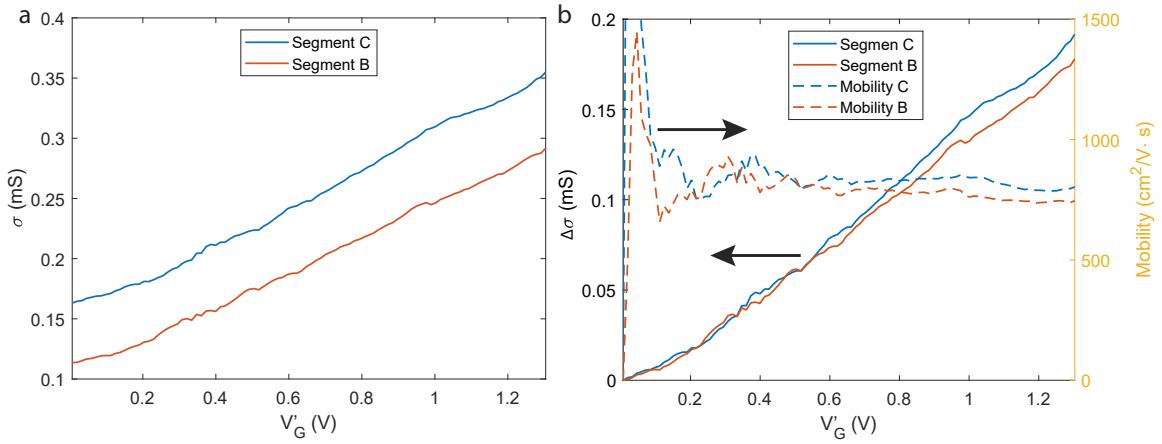

Figure 4.6: a, Sample TMYH30 conductivity vs. V_G taken at $T = 12\,\mathrm{K}$ and $B = 0\,\mathrm{T}$. The conductivities calculated for the two segments have a constant difference. **b**, Conductivity calculated with the 0th channel conductance subtracted and the mobility calculated.

conductance $G(V_G, B) - G(V_G, B = 0\,\mathrm{T})$ is constant with varying V_G at $B < 2\,\mathrm{T}$: the curves for these small magnetic fields are parallel to each other. To illustrate this point better, Figure 4.5**b** shows the same measurements but with a baseline at $B = 0\,\mathrm{T}$ subtracted, showing the difference of conductance vs. gate voltage $\Delta G(V_G, B) = G(V_G, B) - G(V_G, B = 0\,\mathrm{T})$. As we can see, all the lines below 2T are completely flat. Based on this evidence and Eq. 4.4, we can conclude that the "V" shaped increase of the magneto-conductance is purely due to the 0^- channel, and not from the bulk states.

The bumps in the conductance (minimum in resistance) at $B > 2\,\mathrm{T}$ are attributed to the Shubnikov–de Haas oscillation, as that gate voltage of the bumps correspond to the plateau in the Hall resistance as shown in Figure 4.8**a**.

The presence of the edge channel is also confirmed by the conductivity calculations for segments B and C shown in Figure 4.6. Figure 4.6**a** shows the conductivity vs. V_G calculated from 4-point conductance:

$$\sigma_{\mathrm{B/C}} = \frac{W}{L} G_{\mathrm{Seg\ B/C}} = \frac{W}{L} R^{-1}_{04,12/23}. \tag{4.9}$$

For a diffusive conductor, the resistance is proportional to the length of the channel and we expect that the conductivity values calculated for the two segments to be equal. However,

the conductivity values for the 2 segments shown in Figure 4.6**a** are different from each other by a constant amount throughout the varying gate voltage. Now, according to Eq. 4.4, the conductance change due to changing gate voltage is from the bulk states. Thus, if we take the difference of the conductance from the conductance at charge neutrality (CNP),

$$\Delta G(V_G) = G(V_G) - G_{\mathrm{CNP}}, \tag{4.10}$$

this ΔG is purely due to the bulk conduction and is diffusive. We calculate the conductivity using ΔG and get the plot shown in Figure 4.6**b**. Indeed, the two curves overlap through out the V_G range. The mobility is calculated as described later and plotted here. This proves that the bulk conduction is in the diffusive conduction regime while the edge conduction is not. The resistance values of the two segments at CNP can be used to estimate the mean free path of the edge channel. If we assume only one of the edge channels is contributing at 12K, using Eq. 1.7, we can estimate the mean free path to be on the order of $10\,\mu\mathrm{m}$. The mean free path of the bulk transport (calculated in the end of this section), on the other hand, is much lower $\sim 9\,\mathrm{nm}$.

The ballistic nature of the edge transport measured at CNP can also be seen in Figure 4.7. Recall in Chapter 1 we discussed that an invasive probe breaks the ribbon into two segments and increases the resistance by $\frac{(1-T_s)}{T_s}\frac{1}{g_s g_v}h/e^2$ (Eq. 1.8). Similarly, each transverse arm in a Hall bar can be viewed as an invasive probe: it introduces scattering. Thus, we expect to see that the resistance increases by a certain quantity for each segment, no matter how long it is. Remarkably, as shown in Figure 4.7**b** and **c**, we observe this phenomenon regardless of the segment length at $B = 9\,\mathrm{T}$. We can also see in Figure 4.7**c** the equivalence of temperature and magnetic field, as the low field measurements at $T = 65\,\mathrm{K}$, are similar to the high field ones at $T = 4.5\,\mathrm{K}$. This suggests that both can turn on the 0^- channel.

The fluctuations shown in Figure 4.7**d** are due to quantum interference as the Fermi wavelength changes with the gate voltage. The reproducible overlapping fluctuations measured on the opposite edges indicate that quantum coherence is at least maintained across

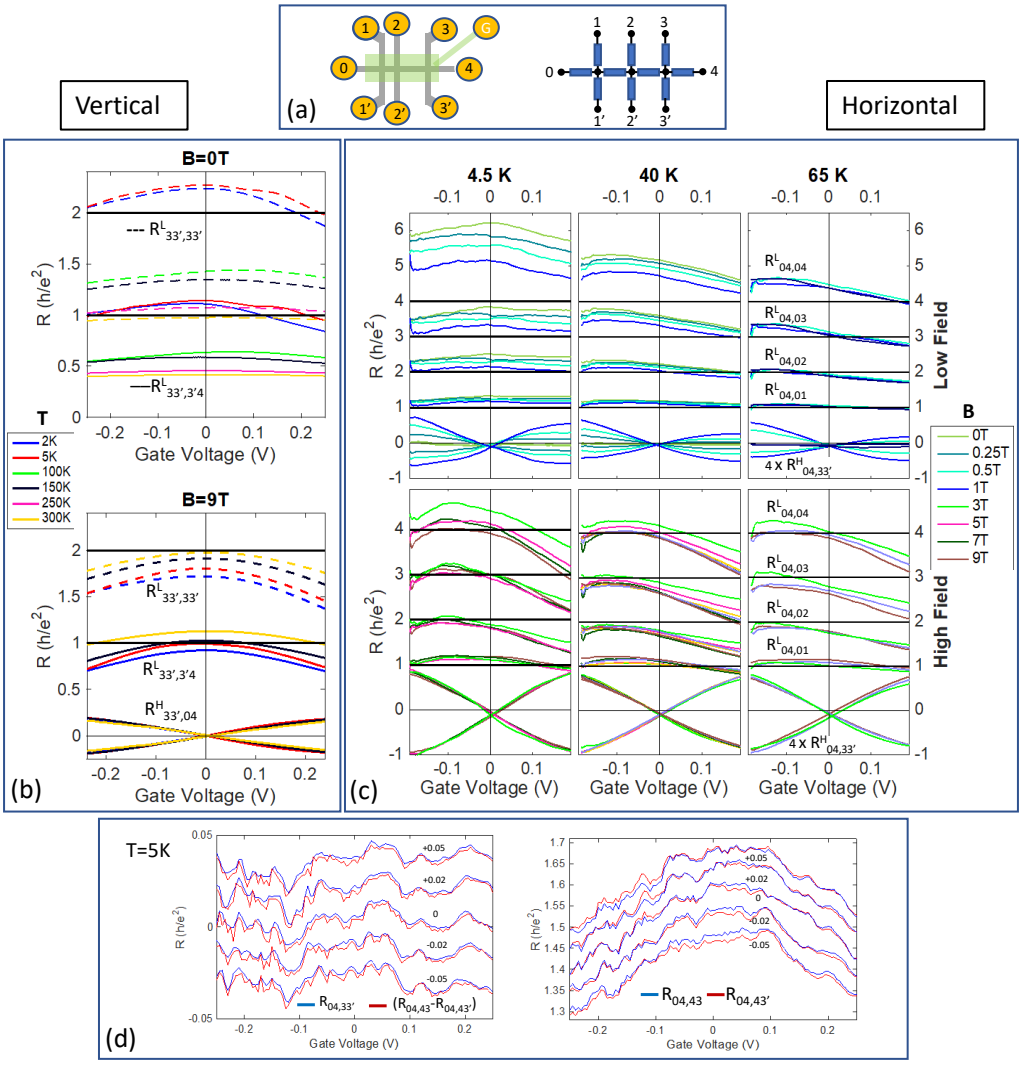

Figure 4.7: A set of plots that show the equivalence of Hall bar segmentation and scattering centers in 1D transport. Here we label $R_{ij,kl} = V_{kl}/I_{ij}$. **a**, The Hall bar diagram showing all the contact labels on the left. The Hall bar broken into a network of resistors on the right. **b**, The resistances measured along the "vertical" direction, as the current flows along the 3 to 3' contacts. **c**, The resistances measured along the "horizontal" direction, as the current flows along the 0 to 4 direction. Note that all the Hall resistances are displayed with a $4\times$ factor for better visibility. **d**, Resistance measurements showing the consistent fluctuations indicating quantum coherence. The gate voltage is measured with respect to the CNP V'_G.

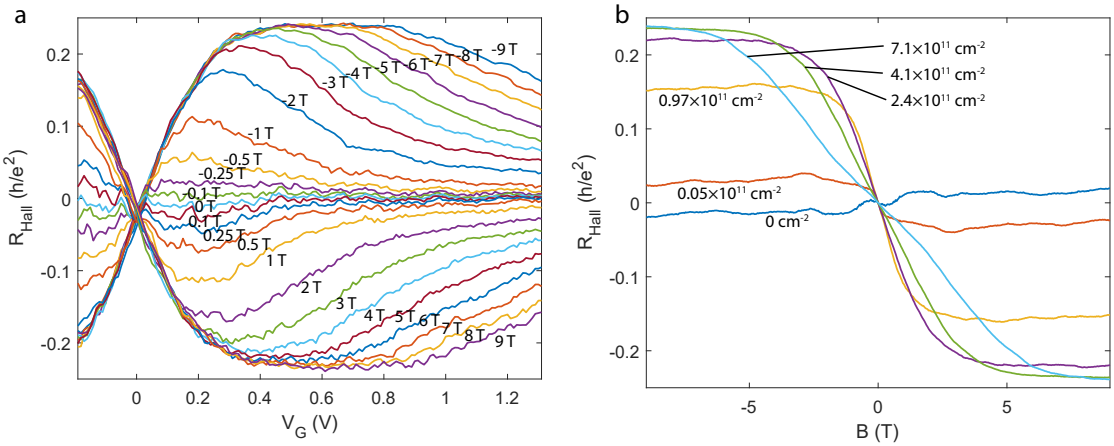

Figure 4.8: **a**, Hall resistances vs. gate voltage V_G. **b**, Hall resistance vs. magnetic field.

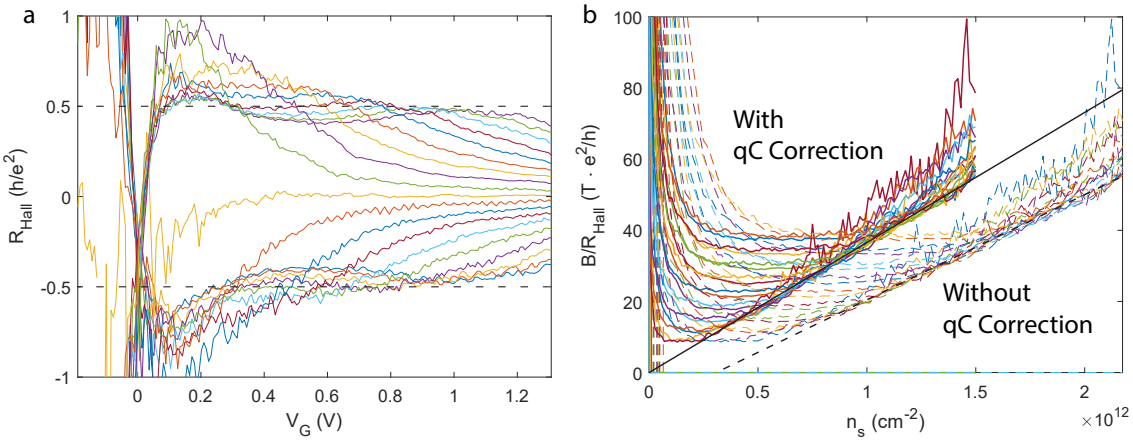

Figure 4.9: **a**, Hall effect with corrected current. **b**, B/R_{Hall} plot with respect to the charge density, calculated with and without qC correction.

the sample's width ($0.7\,\mu\mathrm{m}$).

Figure 4.8 shows two plots of the Hall resistance measurements. We can see the plateaus are at $\sim \frac{1}{4}h/e^2$. This value seems to indicate a bilayer graphene. However, the existence of the edge conductance channel actually provides a current with out Hall effect, which reduces the current flowing through he bulk by roughly half and results in the seemingly bilayer Hall plateaus.

In SLG, the Hall plateau appears at [88]

$$R_{Hall} = \frac{1}{2+4n} h/e^2. \tag{4.11}$$

Its 0th Hall plateau is thus at $\frac{1}{2}h/e^2$. Our value at $\frac{1}{4}h/e^2$ seems to indicate a bilayer. However, we speculate that the edge conduction "steals" part of the current, effectively short out the bulk conduction. Note that in Figure 4.8**a**, all the lines extend from the CNP and follow the same curve. This universal curve is manifest in Figure 4.8**b** as plateaus at lower than quantum hall resistance values. This phenomenon is not expected in BLG and can only be explained by a 0th channel that takes part of the current and has no Hall effect. Thus, the seemingly small Hall resistance is a result from miscounting the current. To account for that current loss, we use a parallel resistance model. We take the resistance of the Hall bar at the CNP, which is close to that of the 0th channel, and use that to calculate the current flowing through the edge channel. We thus get the corrected Hall effect shown in Figure 4.9**a**. Here indeed, the Hall plateaus recover to the $\frac{1}{2}h/e^2$.

From Figure 4.6 we can estimate the mobility of the bulk states. With an appropriate charge density we can estimate the bulk mean free path. The charge density n_s can be calculated with the gate voltage by [89]

$$V_G = \frac{\hbar c^* \sqrt{\pi n_s}}{e} + \frac{e n_s}{C_G}, \tag{4.12}$$

where the first term is the quantum capacitance (qC) correction and C_G is the geometrical capacitance of the gate. These parameters are determined through the quantum Hall measurements by requiring that the B/R_{Hall} vs. n_s lines all extend to the origin, as shown in Figure 4.9**b**. The mobility is calculated using this charge density and plotted in Figure 4.6**b**. From the mobility, we get the mean free path for the bulk $L_{0,bulk} \approx 9\,\mathrm{nm}$ at $n_s = 10^{12}\,\mathrm{cm}^{-2}$.

4.2 Corbino Ring Measurements

The Corbino ring consists of a conducting ring with electrodes contacting it inner and outer rims. Thus, the sample is a conductor without edges, allowing us to study the bulk

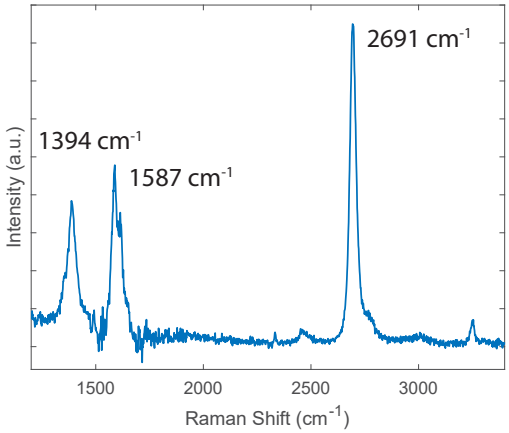

Figure 4.10: Raman spectrum of sample TSYH4.

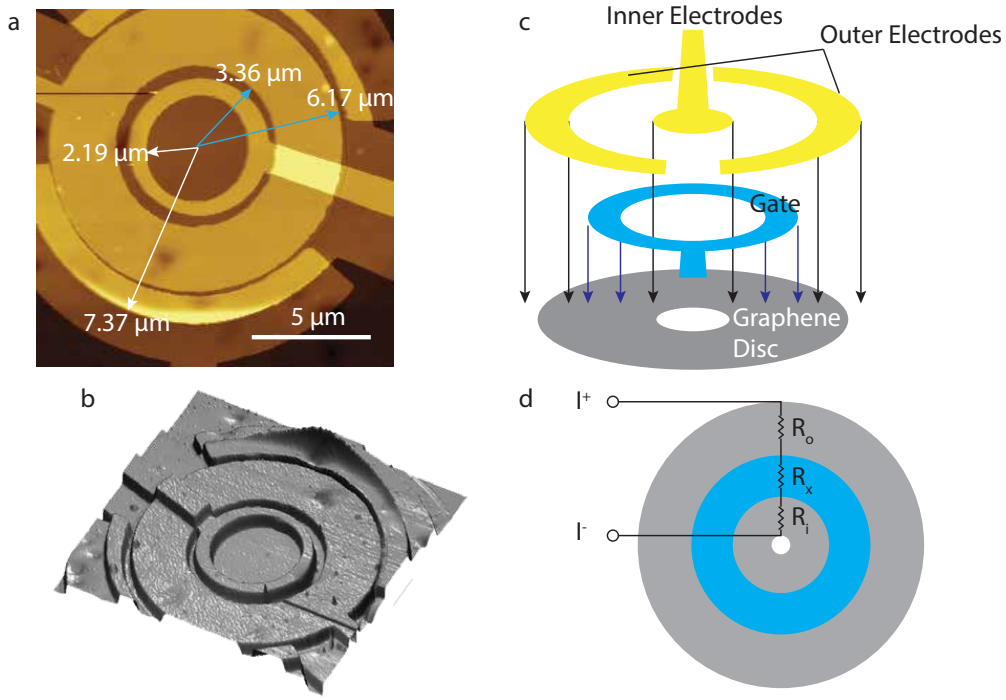

Figure 4.11: **a**, AFM image of the Corbino ring device. **b**, A 3D rendering of the AFM data shown in **a**. **c**. An illustration of the three-layer structure of the Corbino ring device. Since we cannot use back gate, the top gate has to be sandwiched between graphene and the electrodes, with Al_2O_3 isolation layers on both sides. **d**, The Corbino ring can be modeled as three resistors in series. Here, only R_x is controlled by the gate while the outer ring R_o and the inner ring R_i are not.

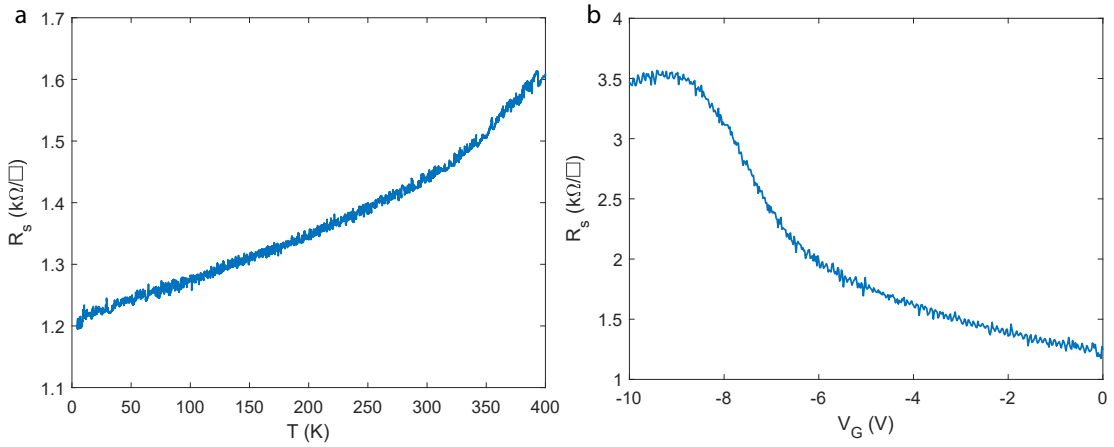

Figure 4.12: a, Sheet resistance as defined in Eq. 4.16 vs. temperature at zero gate voltage and zero magnetic field. **b**, The gate voltage sweep at $T = 4.4\,\mathrm{K}$ and $B = 0\,\mathrm{T}$ was used to identify the CNP at around -9.5V.

transport alone. By comparing the transport in the Corbino ring and that of the Hall bar, we can further separate the transport phenomena of the edge from those of the bulk.

The substrate of sample TSYH4 was cut and polished by TICNN. The chip was first annealed at 1525 °C for 1800s to flatten the surface and then graphene was grown at 1660 °C for 7200s and again at 1660 °C for 5400s. Between the two 1660 °C growth procedures, the sample was taken out from the chamber for characterization. The sample has low-strain graphene as indicated by Raman spectra shown in Figure 4.10. Corbino ring structures were fabricated with the process that is describe in Figure 2.10. The resulting structure is shown in Figure 4.11**a**, **b**. As is illustrated in Figure 4.11**c**, the gate is sandwiched in between graphene and the electrodes with Al_3O_3 on both sides. Edge contacts were used for the electrodes (Figure 2.7).

Since only part of the ring is covered by the gate, we can divide it into three resistors in series (Figure 4.11**d**). Because the Corbino ring does not allow 4 point measurements, here we neglect the contact resistance of the Pd/Au edge contacts. R_x is the ring under the gate and can be tuned by the gate voltage; R_i and R_o are the inner and outer ring resistances, respectively. The ring resistance is

$$R = \frac{R_s}{2\pi} \ln \frac{r_2}{r_1}, \tag{4.13}$$

where R_s is the sheet resistance, and r_1 and r_2 are the ring's inner and outer radius, respectively. Thus, the total resistance is

$$R = \frac{R_s(0)}{2\pi} \ln \frac{r_{g,1} r_{r,2}}{r_{r,1} r_{g,2}} + \frac{R_s(V_G)}{2\pi} \ln \frac{r_{g,2}}{r_{g,1}}, \tag{4.14}$$

where $r_{r,\nu}$ and $r_{g,\nu}$ stand for the inner ($\nu = 1$) and outer ($\nu = 2$) radii of the Corbino ring and the gate ring, respectively. Note that R_s is a function of the gate voltage and and the portion of the ring outside of the gate has a constant $R_s(0)$. We can estimate $R_s(0)$ by measuring the resistance of the device at zero gate voltage:

$$R(V_G = 0) = \frac{R_s(0)}{2\pi} \ln \frac{r_{r,2}}{r_{r,1}}. \tag{4.15}$$

Using this zero gate voltage sheet resistance and Eq. 4.14, we can estimate R_s under non-zero gate voltages. The data presented here are processed using the formula:

$$R_s = 2\pi \left(\ln \frac{r_{g,2}}{r_{g,1}} \right)^{-1} \left(R - \frac{R_s(0)}{2\pi} \ln \frac{r_{g,1} r_{r,2}}{r_{r,1} r_{g,2}} \right), \tag{4.16}$$

where R is the measured resistance.

Figure 4.12**a** is the temperature dependent sheet resistance plot. In contrast to sample TMYH30 Hall bar (Figure 4.3**b**), the resistance increases with temperature. At $T < 200\,\mathrm{K}$, the increase is approximately linear, which can be attributed to the scattering due to acoustic phonons [90]. The non-linear behavior at higher temperatures is attributed to higher energy phonon mode(s) [90].

Because we cannot measure the Hall effect on the Corbino ring, the maximum resistance point was used to identify the CNP. Figure 4.12**b** is a plot of the gate sweep of the device at 4K and zero magnetic field. The CNP can be reached at around $V_G = -9.5\,\mathrm{V}$.

Figure 4.13**a** shows the resistance vs. magnetic field measurements of the Corbino ring at the charge neutrality point as well as at the electron doped side. In contrast with the

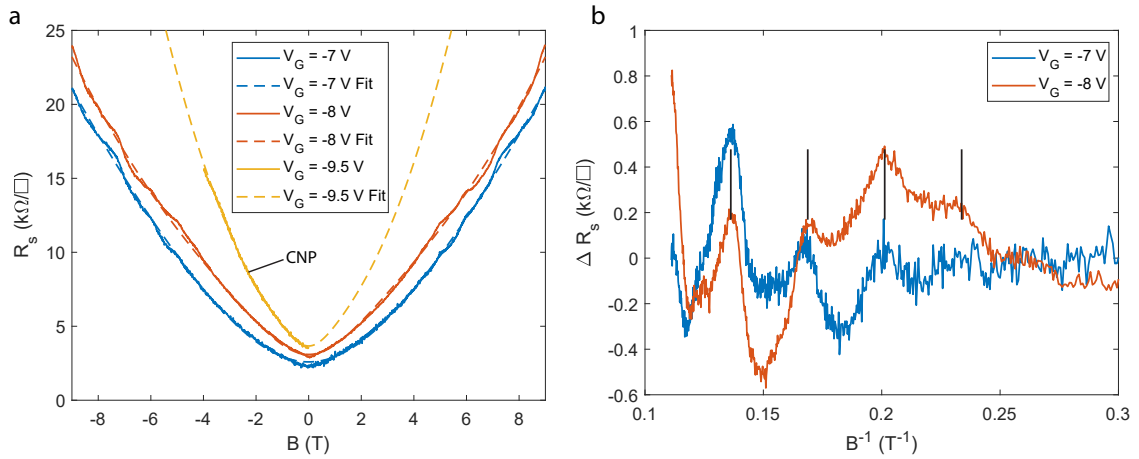

Figure 4.13: **a**, The resistivity of sample TSYH4 Corbino ring with respect to magnetic field. The data is fitted using the two-carrier model Eq. 4.19. **b**, The residue resistance plotted with respect to $1/B$ reveals weak but visible Shubnikov–de Haas oscillation.

result from TMYH30 shown in Figure 4.3**a**, all the Corbino rings have clear positive magnetoresistance at all gate voltages measured. In the Drude model, in the Corbino geometry, we expect a quadratic magnetoresistance because the current has a transverse component due to Lorentz force. Starting from the Drude model, we have

$$\boldsymbol{j} = en_s\boldsymbol{v} = \frac{en_s\mu}{1+(\mu B)^2}\left(\boldsymbol{E} + \mu\boldsymbol{E}\times\boldsymbol{B}\right), \tag{4.17}$$

where $\boldsymbol{j}$ is the drift current, $\boldsymbol{v}$ is the drift velocity and μ is the carrier mobility. Taking out the longitudinal component of the current from Eq. 4.17, we get

$$\rho = |E|/j_{\parallel} = \frac{1+(\mu B)^2}{en_s\mu}, \tag{4.18}$$

where $j_{\parallel}$ is the current density along the electric field direction. In our sample, the curve cannot be fitted with the simple quadratic form. Rather, a consideration of two-carrier model can fit quite well. We arrive at the two carrier model formula by considering two carrier types each with their own mobility values and add up their contributions to the total

current density. We have

$$\rho_{tc} = \left(\frac{en_{s1}\mu_1}{1+(\mu_1 B)^2} + \frac{en_{s2}\mu_2}{1+(\mu_2 B)^2} \right)^{-1}. \tag{4.19}$$

Here carriers 1 and 2 can be electrons and holes. We used Eq. 4.19 to fit the data which is indicated by dashed lines in Figure 4.13**a**. The fitting parameters can give us a hint of the charge density and mobility of the carriers. The charge density is on the order of $10^{11} - 10^{12}\,\mathrm{cm}^{-2}$ and the mobility is the on the order of $1000 - 6000\,\mathrm{cm}^2/\mathrm{V}\cdot\mathrm{s}$.

The residual resistance left from the fit is plotted in Figure 4.13**b** with respect to $1/B$. SdH oscillations can be observed and we can estimate the charge density by the periodicity of the peaks in $1/B$ [91]:

$$n_s = \frac{4e}{h\Delta\left(1/B_i\right)}, \tag{4.20}$$

where $\Delta\left(1/B_i\right)$ is the periodicity. Using Eq. 4.20, we obtain an estimation for the charge density at $V_G = -7\,\mathrm{V}$ to be $3.0 \times 10^{12}\,\mathrm{cm}^{-2}$, which corroborate the number obtained by the fitting of Figure 4.13**a**. Using this charge density and the sheet resistance, we estimate the mobility to be $\mu \approx 936\,\mathrm{cm}^2/\mathrm{V}\cdot\mathrm{s}$.

During the magnetic sweep at the CNP, the large gate voltage caused the gate to break down, thus the termination at $B = -4\,\mathrm{T}$.

The transport data of the Corbino rings can be explained by the Drude model very well. There is no "V" shaped magneto-conductance. The conductance decreases with increasing temperature. These results contrast with those observed in the Hall bar sample and indicates that the transport in the Hall bar sample is indeed governed by a combination of edge and bulk transport.

4.3 Summary

The two samples presented here are both on 4H-SiC AC 37° facet and both low-strain graphene. With both the Hall bar and the edgeless Corbino ring, the edge state's contri-

bution can be singled out by comparison. Indeed, while we observed the same type of transport behaviors in the Hall bar sample with respect to temperature and magnetic field as those observed in SW-GNR's earlier [4, 14, 13], those behaviors were not seen in the Corbino rings. The model consisting of a long mean free path channel 0^+, a thermally activated channel 0^- in addition to the bulk conduction channels can explain the measurements very well.

CHAPTER 5
CONCLUSION

In this thesis, graphene grown on the non-polar SiC facets are investigated, motivated by the exceptional transport phenomenon discovered earlier [4].

Growth of graphene on various facets has been investigated. In most cases, the growth is epitaxial, despite the lack of hexagonal symmetry on the non-polar facets.

The graphene grown on the 4H-SiC AC 37° facet comes in at least four different types. The outcome of the growth can be controlled by carefully tuning the growth condition. Both high-strain and low-strain graphene were found on this facet. High-strain graphene is charge neutral according to ARPES and STS studies. While the high-strain graphene has a LEED pattern aligned with the underlying crystal structure indicating an epitaxial growth, low-strain graphene's orientation cannot be determined by the LEED pattern at this point.

The growth on 4H-SiC ZZ facet results in large stripes of graphene patches. The graphene on this surface has pleats running perpendicular to the $\langle 1\bar{1}00\rangle$ direction.

Graphene grown on the 4H-SiC C-side ZZ facet forms large triangular patches. These triangular patches merge together and form large area SLG up to several hundred microns in size. The graphene is highly strained and has a very small 2D peak in its Raman spectrum. After exposure to air, the strain is reduced and its Raman spectrum indicates a pristine graphene with low strain.

A graphitic interface layer between graphene and the SiC is found on all Si-side non-polar facets. The 4H-SiC C-side ZZ facet doesn't have an interface layer but the graphene initially is highly strained and resembles the interface layer.

On the 6H-SiC ZZ facet, high-aspect-ratio GNR's are grown with widths on the order of 20 nm and lengths up to several micrometers. According to the FFM image, the ribbons grow next to a step in the direction of (0001).

Transport measurements were done on low-strain graphene samples on the 4H-SiC AC facet. The Hall bar measurements suggests the same type of transport mechanism as that observed in Ref. [4] while these transport behaviors are not present in the edgeless Corbino ring devices. These evidences indicate that the edge conduction is really the key to understanding the transport in SW-GNR's as well as the Hall-bar on non-polar facets.

5.1 Future Research

Graphene grown on non-polar SiC facets is a very promising direction for the future of epigraphene electronics research. Much remains to be done.

The structural characterizations presented here are only preliminary. It would be interesting to perform STM and micro-LEED studies to reveal the orientation of the low-strain graphene on the 4H-SiC AC 37° facet. Non-invasive probe potentiometry can be employed to measure the ballistic channel's potential drop [92]. It would be interesting to see if it can reveal the difference between the edge and the bulk.

The graphitic interface layer is universal to all Si-side facets investigated in my thesis. What is the physical structure of the interface layer? How similar are these interface layers on different facets? Is its effect on the doping level of the SLG similar to that of the buffer layer on the Si face [31]? To answer these questions, more characterizations need to be done on the interface layer. Specifically, structural information can be obtained by STM and TEM, while XPS can reveal the information of its bond with he substrate.

Though various facet angles were investigated here for growth, transport measurements were only done on one of them. Transport measurements on the other facets are yet to be performed.

The coherent edge state may be tuned by local gates. This allows complex networks of graphene ribbons to be controlled by multiple gates. This thesis opens the door to a variety of device possibilities to be explored in future research, and will have a major impact on graphene electronics.

Appendices

APPENDIX A

SIC FACETS AND FACET ANGLES

AC and ZZ SiC facets are named by the epigraphene edge type grown on the Si-face, as shown in Figure A.1**a**. The facet indices and their facet angles are listed in Table A.1. The calculations are based on SiC crystal constants obtained from Ref. [93]. The Wulff diagrams for 4H- and 6H-SiC are shown in Figure A.2.

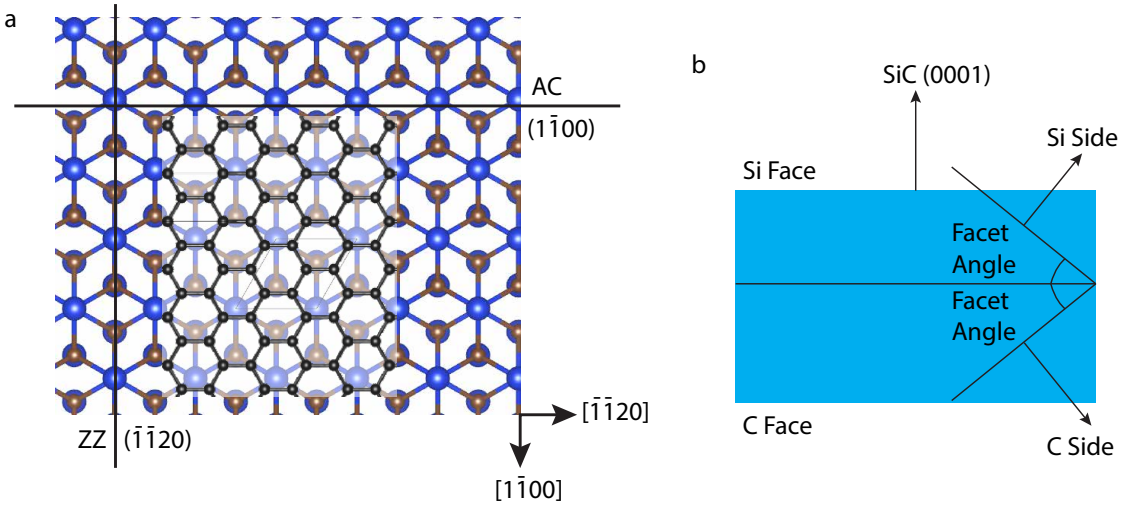

Figure A.1: a, SiC facet indices and their names (AC/ZZ) and the directions indices. The sizes of SiC and graphene are not to scale in this image. Note that the facet is perpendicular to the direction of the same index. **b**, The facet angles listed in Table A.1 are measured from the polar facet.

Table A.1: SiC facet indices and corresponding facet angles in degrees.

	4H		6H	
n	$(1\bar{1}0n)$	$(11\bar{2}n)$	$(1\bar{1}0n)$	$(11\bar{2}n)$
1	75.14°	81.29°	80.00°	84.18°
2	62.04°	72.96°	70.57°	78.49°
3	51.47°	65.31°	62.11°	73.01°
4	43.29°	58.49°	54.79°	67.83°
5	37.00°	52.54°	48.59°	63.01°
6	32.13°	47.40°	43.37°	58.57°
7	28.29°	42.99°	39.00°	54.51°
8	25.22°	39.21°	35.32°	50.83°
9	22.72°	35.95°	32.20°	47.49°
10	20.65°	33.13°	29.55°	44.47°
11	18.91°	30.68°	27.26°	41.75°
12	17.43°	28.54°	25.28°	39.29°
13	16.16°	26.66°	23.56°	37.06°
14	15.06°	24.99°	22.04°	35.04°
15	14.10°	23.51°	20.70°	33.21°
16	13.25°	22.19°	19.51°	31.53°
17	12.50°	21.00°	18.44°	30.01°
18	11.82°	19.93°	17.48°	28.61°
19	11.22°	18.96°	16.61°	27.33°
20	10.67°	18.07°	15.82°	26.15°
21	10.17°	17.26°	15.11°	25.06°
22	9.72°	16.52°	14.45°	24.05°
23	9.30°	15.84°	13.85°	23.12°
24	8.92°	15.21°	13.29°	22.25°
25	8.57°	14.63°	12.78°	21.44°
26	8.25°	14.09°	12.30°	20.69°
27	7.94°	13.59°	11.86°	19.98°
28	7.66°	13.12°	11.44°	19.32°
29	7.40°	12.68°	11.06°	18.70°
30	7.16°	12.27°	10.70°	18.12°

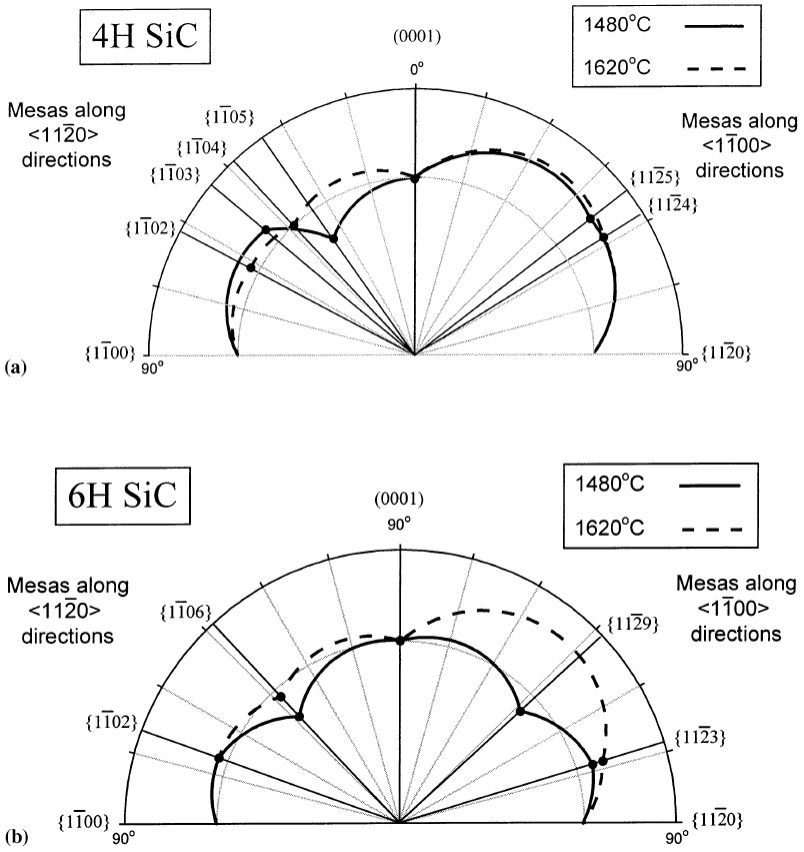

Figure A.2: Wulff diagrams for 4H- and 6-SiC. Reprinted from Ref. [75].

REFERENCES

[1] M. Roser, *Moore's Law Transistor Count 1971-2018*, https://ourworldindata.org/uploads/2019/05/Transistor-Count-over-time-to-2018.png, [Online; accessed 17-April-2020], 2019.

[2] G. E. Moore, "Cramming more components onto integrated circuits," *Proceedings of the IEEE*, vol. 86, no. 1, pp. 82–85, 1998.

[3] A. Shilov, *TSMC: 5nm on Track for Q2 2020 HVM, Will Ramp Faster Than 7nm*, https://www.anandtech.com/show/15016/tsmc-5nm-on-track-for-q2-2020-hvm-will-ramp-faster-than-7nm, [Online; accessed 17-April-2020], 2019.

[4] J. Baringhaus, M. Ruan, F. Edler, A. Tejeda, M. Sicot, A. Taleb-Ibrahimi, A.-P. Li, Z. Jiang, E. H. Conrad, C. Berger, *et al.*, "Exceptional ballistic transport in epitaxial graphene nanoribbons," *Nature*, vol. 506, no. 7488, pp. 349–354, 2014.

[5] Z. Guo, R. Dong, P. S. Chakraborty, N. Lourenco, J. Palmer, Y. Hu, M. Ruan, J. Hankinson, J. Kunc, J. D. Cressler, *et al.*, "Record maximum oscillation frequency in c-face epitaxial graphene transistors," *Nano letters*, vol. 13, no. 3, pp. 942–947, 2013.

[6] Y.-M. Lin, C. Dimitrakopoulos, K. A. Jenkins, D. B. Farmer, H.-Y. Chiu, A. Grill, and P. Avouris, "100-ghz transistors from wafer-scale epitaxial graphene," *Science*, vol. 327, no. 5966, pp. 662–662, 2010.

[7] Y.-M. Lin, A. Valdes-Garcia, S.-J. Han, D. B. Farmer, I. Meric, Y. Sun, Y. Wu, C. Dimitrakopoulos, A. Grill, P. Avouris, *et al.*, "Wafer-scale graphene integrated circuit," *Science*, vol. 332, no. 6035, pp. 1294–1297, 2011.

[8] J. Moon, D Curtis, S Bui, M Hu, D. Gaskill, J. Tedesco, P Asbeck, G. Jernigan, B. VanMil, R. Myers-Ward, *et al.*, "Top-gated epitaxial graphene fets on si-face sic wafers with a peak transconductance of 600 ms/mm," *IEEE Electron Device Letters*, vol. 31, no. 4, pp. 260–262, 2010.

[9] B. Dlubak, M.-B. Martin, C. Deranlot, B. Servet, S. Xavier, R. Mattana, M. Sprinkle, C. Berger, W. A. De Heer, F. Petroff, *et al.*, "Highly efficient spin transport in epitaxial graphene on sic," *Nature Physics*, vol. 8, no. 7, pp. 557–561, 2012.

[10] J. H. Hankinson, "Spin dependent current injection into epitaxial graphene nanoribbons," PhD thesis, Georgia Institute of Technology, 2015.

[11] M. Sprinkle, M. Ruan, Y. Hu, J Hankinson, M. Rubio-Roy, B. Zhang, X. Wu, C. Berger, and W. A. De Heer, "Scalable templated growth of graphene nanoribbons on sic," *Nature nanotechnology*, vol. 5, no. 10, pp. 727–731, 2010.

[12] M. Ruan, Y. Hu, Z. Guo, R. Dong, J. Palmer, J. Hankinson, C. Berger, and W. A. De Heer, "Epitaxial graphene on silicon carbide: Introduction to structured graphene," *MRS bulletin*, vol. 37, no. 12, pp. 1138–1147, 2012.

[13] M. Ruan, "Structured epitaxial graphene for electronics," PhD thesis, Georgia Institute of Technology, 2012.

[14] J. Baringhaus, "Mesoscopic transport phenomena in epitaxial graphene nanostructures: A surface science approach," PhD thesis, Leibniz Universität Hannover, 2015.

[15] D. Deniz, "Fabrication of arrays of ballistic epitaxial graphene nanoribbons," PhD thesis, Georgia Institute of Technology, 2018.

[16] A. C. Neto, F. Guinea, and N. M. Peres, "Drawing conclusions from graphene," *Physics World*, vol. 19, no. 11, p. 33, 2006.

[17] A. C. Neto, F. Guinea, N. M. Peres, K. S. Novoselov, and A. K. Geim, "The electronic properties of graphene," *Reviews of modern physics*, vol. 81, no. 1, p. 109, 2009.

[18] P. R. Wallace, "The band theory of graphite," *Physical review*, vol. 71, no. 9, p. 622, 1947.

[19] I. Kleftogiannis, I. Amanatidis, and V. A. Gopar, "Conductance through disordered graphene nanoribbons: Standard and anomalous electron localization," *Physical Review B*, vol. 88, no. 20, p. 205 414, 2013.

[20] K. Wakabayashi, Y. Takane, M. Yamamoto, and M. Sigrist, "Electronic transport properties of graphene nanoribbons," *New Journal of Physics*, vol. 11, no. 9, p. 095 016, 2009.

[21] A. Akhmerov and C. Beenakker, "Boundary conditions for dirac fermions on a terminated honeycomb lattice," *Physical Review B*, vol. 77, no. 8, p. 085 423, 2008.

[22] K. S. Novoselov, D Jiang, F Schedin, T. Booth, V. Khotkevich, S. Morozov, and A. K. Geim, "Two-dimensional atomic crystals," *Proceedings of the National Academy of Sciences*, vol. 102, no. 30, pp. 10 451–10 453, 2005.

[23] D. Purdie, N. Pugno, T Taniguchi, K Watanabe, A. Ferrari, and A. Lombardo, "Cleaning interfaces in layered materials heterostructures," *Nature communications*, vol. 9, no. 1, pp. 1–12, 2018.

[24] Y. Zhang, L. Zhang, and C. Zhou, "Review of chemical vapor deposition of graphene and related applications," *Accounts of chemical research*, vol. 46, no. 10, pp. 2329–2339, 2013.

[25] W. A. De Heer, C. Berger, M. Ruan, M. Sprinkle, X. Li, Y. Hu, B. Zhang, J. Hankinson, and E. Conrad, "Large area and structured epitaxial graphene produced by confinement controlled sublimation of silicon carbide," *Proceedings of the National Academy of Sciences*, vol. 108, no. 41, pp. 16 900–16 905, 2011.

[26] A. Van Bommel, J. Crombeen, and A Van Tooren, "Leed and auger electron observations of the sic (0001) surface," *Surface Science*, vol. 48, no. 2, pp. 463–472, 1975.

[27] C. Berger, Z. Song, T. Li, X. Li, A. Y. Ogbazghi, R. Feng, Z. Dai, A. N. Marchenkov, E. H. Conrad, P. N. First, *et al.*, "Ultrathin epitaxial graphite: 2d electron gas properties and a route toward graphene-based nanoelectronics," *The Journal of Physical Chemistry B*, vol. 108, no. 52, pp. 19 912–19 916, 2004.

[28] K. V. Emtsev, A. Bostwick, K. Horn, J. Jobst, G. L. Kellogg, L. Ley, J. L. McChesney, T. Ohta, S. A. Reshanov, J. Röhrl, *et al.*, "Towards wafer-size graphene layers by atmospheric pressure graphitization of silicon carbide," *Nature materials*, vol. 8, no. 3, p. 203, 2009.

[29] Y. Yang, G. Cheng, P. Mende, I. G. Calizo, R. M. Feenstra, C. Chuang, C.-W. Liu, C.-I. Liu, G. R. Jones, A. R. H. Walker, *et al.*, "Epitaxial graphene homogeneity and quantum hall effect in millimeter-scale devices," *Carbon*, vol. 115, pp. 229–236, 2017.

[30] A. Winkelmann, B. Schröter, and W. Richter, "Electron diffraction methods for the analysis of silicon carbide surfaces and the controlled growth of polytype heterostructures," *Journal of Physics: Condensed Matter*, vol. 16, no. 17, S1555, 2004.

[31] J Ristein, S Mammadov, and T. Seyller, "Origin of doping in quasi-free-standing graphene on silicon carbide," *Physical review letters*, vol. 108, no. 24, p. 246 104, 2012.

[32] C. Berger, E. H. Conrad, and W. A. de Heer, "Epigraphene: Epitaxial graphene on silicon carbide," *arXiv preprint arXiv:1704.00374*, 2017.

[33] Y. Hu, "Production and properties of epitaxial graphene on the carbon terminated face of hexagonal silicon carbide," PhD thesis, Georgia Institute of Technology, 2013.

[34] J.-P. Turmaud, "Variable range hopping conduction in the epitaxial graphene buffer layer on sic(0001)," PhD thesis, Georgia Institute of Technology, 2018.

[35] K. Emtsev, F Speck, T. Seyller, L Ley, and J. D. Riley, "Interaction, growth, and ordering of epitaxial graphene on sic {0001} surfaces: A comparative photoelectron spectroscopy study," *Physical Review B*, vol. 77, no. 15, p. 155 303, 2008.

[36] M. Nevius, M Conrad, F Wang, A Celis, M. Nair, A Taleb-Ibrahimi, A Tejeda, and E. Conrad, "Semiconducting graphene from highly ordered substrate interactions," *Physical review letters*, vol. 115, no. 13, p. 136 802, 2015.

[37] J. M. Palmer, "Pre-growth structures for high quality epitaxial graphene nanoelectronics grown on silicon carbide," PhD thesis, Georgia Institute of Technology, 2014.

[38] A. Tzalenchuk, S. Lara-Avila, A. Kalaboukhov, S. Paolillo, M. Syväjärvi, R. Yakimova, O. Kazakova, T. Janssen, V. Fal'Ko, and S. Kubatkin, "Towards a quantum resistance standard based on epitaxial graphene," *Nature nanotechnology*, vol. 5, no. 3, p. 186, 2010.

[39] M. Kruskopf, D. M. Pakdehi, K. Pierz, S. Wundrack, R. Stosch, T. Dziomba, M. Götz, J. Baringhaus, J. Aprojanz, C. Tegenkamp, *et al.*, "Comeback of epitaxial graphene for electronics: Large-area growth of bilayer-free graphene on sic," *2D Materials*, vol. 3, no. 4, p. 041 002, 2016.

[40] X. Wu, Y. Hu, M. Ruan, N. K. Madiomanana, J. Hankinson, M. Sprinkle, C. Berger, and W. A. De Heer, "Half integer quantum hall effect in high mobility single layer epitaxial graphene," *Applied Physics Letters*, vol. 95, no. 22, p. 223 108, 2009.

[41] Z. Guo, "Mono-layer c-face epitaxial graphene for high frequency electronics," PhD thesis, Georgia Institute of Technology, 2014.

[42] P. Seneor, B. Dlubak, M.-B. Martin, A. Anane, H. Jaffres, and A. Fert, "Spintronics with graphene," *MRS bulletin*, vol. 37, no. 12, pp. 1245–1254, 2012.

[43] T. Maassen, J. J. van den Berg, N. IJbema, F. Fromm, T. Seyller, R. Yakimova, and B. J. van Wees, "Long spin relaxation times in wafer scale epitaxial graphene on sic (0001)," *Nano letters*, vol. 12, no. 3, pp. 1498–1502, 2012.

[44] M. Orlita, C. Faugeras, P. Plochocka, P. Neugebauer, G. Martinez, D. K. Maude, A.-L. Barra, M. Sprinkle, C. Berger, W. A. De Heer, *et al.*, "Approaching the dirac point in high-mobility multilayer epitaxial graphene," *Physical review letters*, vol. 101, no. 26, p. 267 601, 2008.

[45] M. Orlita, C. Faugeras, R Grill, A Wysmolek, W Strupinski, C. Berger, W. A. de Heer, G. Martinez, and M. Potemski, "Carrier scattering from dynamical magnetoconductivity in quasineutral epitaxial graphene," *Physical review letters*, vol. 107, no. 21, p. 216 603, 2011.

[46] J Maysonnave, S Huppert, F Wang, S Maero, C Berger, W De Heer, T. B. Norris, L. De Vaulchier, S Dhillon, J Tignon, *et al.*, "Terahertz generation by dynamical photon drag effect in graphene excited by femtosecond optical pulses," *Nano letters*, vol. 14, no. 10, pp. 5797–5802, 2014.

[47] J Hicks, A Tejeda, A Taleb-Ibrahimi, M. Nevius, F Wang, K Shepperd, J Palmer, F Bertran, P Le Fevre, J Kunc, *et al.*, "A wide-bandgap metal–semiconductor–metal nanostructure made entirely from graphene," *Nature Physics*, vol. 9, no. 1, p. 49, 2013.

[48] I. Palacio, A. Celis, M. N. Nair, A. Gloter, A. Zobelli, M. Sicot, D. Malterre, M. S. Nevius, W. A. De Heer, C. Berger, *et al.*, "Atomic structure of epitaxial graphene sidewall nanoribbons: Flat graphene, miniribbons, and the confinement gap," *Nano letters*, vol. 15, no. 1, pp. 182–189, 2014.

[49] G. Nicotra, Q. M. Ramasse, I. Deretzis, A. La Magna, C. Spinella, and F. Giannazzo, "Delaminated graphene at silicon carbide facets: Atomic scale imaging and spectroscopy," *ACS nano*, vol. 7, no. 4, pp. 3045–3052, 2013.

[50] A. L. Miettinen, M. Nevius, W. Ko, M Kolmer, A.-P. Li, M. Nair, B Kierren, L Moreau, E. H. Conrad, and A Tejeda, "Edge states and ballistic transport in zigzag graphene ribbons: The role of sic polytypes," *Physical Review B*, vol. 100, no. 4, p. 045 425, 2019.

[51] D. B. Torrance, "Growth and electronic properties of nanostructured epitaxial graphene on silicon carbide," PhD thesis, Georgia Institute of Technology, 2013.

[52] J Baringhaus, J Aprojanz, J Wiegand, D Laube, M Halbauer, J Hübner, M Oestreich, and C Tegenkamp, "Growth and characterization of sidewall graphene nanoribbons," *Applied Physics Letters*, vol. 106, no. 4, p. 043 109, 2015.

[53] S. Datta, *Electronic transport in mesoscopic systems*. Cambridge university press, 1997.

[54] J. Li, Y.-M. Niquet, and C. Delerue, "Magnetic-phase dependence of the spin carrier mean free path in graphene nanoribbons," *Physical review letters*, vol. 116, no. 23, p. 236 602, 2016.

[55] A. C. Ferrari and D. M. Basko, "Raman spectroscopy as a versatile tool for studying the properties of graphene," *Nature nanotechnology*, vol. 8, no. 4, pp. 235–246, 2013.

[56] L. Cançado, K Takai, T Enoki, M Endo, Y. Kim, H Mizusaki, A Jorio, L. Coelho, R Magalhaes-Paniago, and M. Pimenta, "General equation for the determination of the crystallite size l a of nanographite by raman spectroscopy," *Applied Physics Letters*, vol. 88, no. 16, p. 163 106, 2006.

[57] S Piscanec, M Lazzeri, F. Mauri, A. Ferrari, and J Robertson, "Kohn anomalies and electron-phonon interactions in graphite," *Physical review letters*, vol. 93, no. 18, p. 185 503, 2004.

[58] J. Kunc, Y. Hu, J. Palmer, C. Berger, and W. A. De Heer, "A method to extract pure raman spectrum of epitaxial graphene on sic," *Applied Physics Letters*, vol. 103, no. 20, p. 201 911, 2013.

[59] T. Filleter, J. L. McChesney, A. Bostwick, E. Rotenberg, K. V. Emtsev, T. Seyller, K. Horn, and R. Bennewitz, "Friction and dissipation in epitaxial graphene films," *Physical review letters*, vol. 102, no. 8, p. 086 102, 2009.

[60] M. P. Seah and W. Dench, "Quantitative electron spectroscopy of surfaces: A standard data base for electron inelastic mean free paths in solids," *Surface and interface analysis*, vol. 1, no. 1, pp. 2–11, 1979.

[61] A. Zangwill, *Physics at surfaces*. Cambridge university press, 1988, pp. 15–18.

[62] N. W. Ashcroft and N. D. Mermin, *Solid State Physics*. Holt-Saunders, 1976.

[63] P. Mallet, F. Varchon, C. Naud, L. Magaud, C. Berger, and J.-Y. Veuillen, "Electron states of mono-and bilayer graphene on sic probed by scanning-tunneling microscopy," *Physical Review B*, vol. 76, no. 4, p. 041 403, 2007.

[64] C Riedl, U Starke, J Bernhardt, M Franke, and K Heinz, "Structural properties of the graphene-sic (0001) interface as a key for the preparation of homogeneous large-terrace graphene surfaces," *Physical Review B*, vol. 76, no. 24, p. 245 406, 2007.

[65] Y. Zhou, D. S. Fox, P. Maguire, R. O'Connell, R. Masters, C. Rodenburg, H. Wu, M. Dapor, Y. Chen, and H. Zhang, "Quantitative secondary electron imaging for work function extraction at atomic level and layer identification of graphene," *Scientific reports*, vol. 6, p. 21 045, 2016.

[66] S. A. Campbell, *Fabrication Engineering at the Micro and Nanoscale*. Oxford University Press, 2013.

[67] C.-J. Shih, G. L. Paulus, Q. H. Wang, Z. Jin, D. Blankschtein, and M. S. Strano, "Understanding surfactant/graphene interactions using a graphene field effect transistor: Relating molecular structure to hysteresis and carrier mobility," *Langmuir*, vol. 28, no. 22, pp. 8579–8586, 2012.

[68] H. Wang, Y. Wu, C. Cong, J. Shang, and T. Yu, "Hysteresis of electronic transport in graphene transistors," *ACS nano*, vol. 4, no. 12, pp. 7221–7228, 2010.

[69] A. A. Sagade, D. Neumaier, D. Schall, M. Otto, A. Pesquera, A. Centeno, A. Z. Elorzab, and H. Kurza, "Highly air stable passivation of graphene based field effect devices," *Nanoscale*, vol. 7, no. 8, pp. 3558–3564, 2015.

[70] J. Gigliotti, "Integrated dielectrics for protection and gating of epitaxial graphene devices," PhD thesis, Georgia Institute of Technology, 2017.

[71] K. R. Williams, K. Gupta, and M. Wasilik, "Etch rates for micromachining processing-part ii," *Journal of microelectromechanical systems*, vol. 12, no. 6, pp. 761–778, 2003.

[72] L. Wang, I Meric, P. Huang, Q Gao, Y Gao, H Tran, T Taniguchi, K. Watanabe, L. Campos, D. Muller, *et al.*, "One-dimensional electrical contact to a two-dimensional material," *Science*, vol. 342, no. 6158, pp. 614–617, 2013.

[73] V Ramachandran, M. Brady, A. Smith, R. Feenstra, and D. Greve, "Preparation of atomically flat surfaces on silicon carbide using hydrogen etching," *Journal of Electronic Materials*, vol. 27, no. 4, pp. 308–312, 1998.

[74] J. Palmer, J. Kunc, Y. Hu, J. Hankinson, Z. Guo, C. Berger, and W. A. de Heer, "Controlled epitaxial graphene growth within removable amorphous carbon corrals," *Applied Physics Letters*, vol. 105, no. 2, p. 023 106, 2014.

[75] N Nordell, S Karlsson, and A. Konstantinov, "Equilibrium crystal shapes for 6h and 4h sic grown on non-planar substrates," *Materials Science and Engineering: B*, vol. 61, pp. 130–134, 1999.

[76] I. Childres, L. A. Jauregui, W. Park, H. Cao, and Y. P. Chen, "Raman spectroscopy of graphene and related materials," *New developments in photon and materials research*, vol. 1, 2013.

[77] S. Kim and S. Ryu, "Thickness-dependent native strain in graphene membranes visualized by raman spectroscopy," *Carbon*, vol. 100, pp. 283–290, 2016.

[78] J. A. Robinson, C. P. Puls, N. E. Staley, J. P. Stitt, M. A. Fanton, K. V. Emtsev, T. Seyller, and Y. Liu, "Raman topography and strain uniformity of large-area epitaxial graphene," *Nano letters*, vol. 9, no. 3, pp. 964–968, 2009.

[79] C. Casiraghi, A. Hartschuh, E. Lidorikis, H. Qian, H. Harutyunyan, T. Gokus, K. S. Novoselov, and A. Ferrari, "Rayleigh imaging of graphene and graphene layers," *Nano letters*, vol. 7, no. 9, pp. 2711–2717, 2007.

[80] C. Riedl, C Coletti, T Iwasaki, A. Zakharov, and U Starke, "Quasi-free-standing epitaxial graphene on sic obtained by hydrogen intercalation," *Physical review letters*, vol. 103, no. 24, p. 246 804, 2009.

[81] G. Nicotra, Q. M. Ramasse, I. Deretzis, A. La Magna, C. Spinella, and F. Giannazzo, "Delaminated graphene at silicon carbide facets: Atomic scale imaging and spectroscopy," *ACS nano*, vol. 7, no. 4, pp. 3045–3052, 2013.

[82] M. Y. Han, J. C. Brant, and P. Kim, "Electron transport in disordered graphene nanoribbons," *Physical review letters*, vol. 104, no. 5, p. 056 801, 2010.

[83] C. Schoenenberger, A Bachtold, Strunk, C, J.-P. Salvetat, and L Forro, "Interference and interaction in multi-wall carbon nanotubes," *Applied Physics A*, vol. 69, no. 3, pp. 283–295, 1999.

[84] Y. Hu, *Epitaxial Graphene Nanoribbons on SiC*, PhD Thesis Proposal, 2018.

[85] E. McCann, K Kechedzhi, V. I. Fal'ko, H Suzuura, T Ando, and B. Altshuler, "Weak-localization magnetoresistance and valley symmetry in graphene," *Physical review letters*, vol. 97, no. 14, p. 146 805, 2006.

[86] X. Wu, X. Li, Z. Song, C. Berger, and W. A. de Heer, "Weak antilocalization in epitaxial graphene: Evidence for chiral electrons," *Physical review letters*, vol. 98, no. 13, p. 136 801, 2007.

[87] N. F. Mott, "Conduction in non-crystalline materials: Iii. localized states in a pseudogap and near extremities of conduction and valence bands," *Philosophical Magazine*, vol. 19, no. 160, pp. 835–852, 1969.

[88] Y. Zhang, Y.-W. Tan, H. L. Stormer, and P. Kim, "Experimental observation of the quantum hall effect and berry's phase in graphene," *nature*, vol. 438, no. 7065, pp. 201–204, 2005.

[89] A. Das, S. Pisana, B. Chakraborty, S. Piscanec, S. K. Saha, U. V. Waghmare, K. S. Novoselov, H. R. Krishnamurthy, A. K. Geim, A. C. Ferrari, *et al.*, "Monitoring dopants by raman scattering in an electrochemically top-gated graphene transistor," *Nature nanotechnology*, vol. 3, no. 4, pp. 210–215, 2008.

[90] J.-H. Chen, C. Jang, S. Xiao, M. Ishigami, and M. S. Fuhrer, "Intrinsic and extrinsic performance limits of graphene devices on sio 2," *Nature nanotechnology*, vol. 3, no. 4, p. 206, 2008.

[91] C. Berger, Z. Song, X. Li, X. Wu, N. Brown, C. Naud, D. Mayou, T. Li, J. Hass, A. N. Marchenkov, *et al.*, "Electronic confinement and coherence in patterned epitaxial graphene," *Science*, vol. 312, no. 5777, pp. 1191–1196, 2006.

[92] A. De Cecco, V. Prudkovskiy, D. Wander, R. Ganguly, C. Berger, W. de Heer, H. Courtois, and C. B. Winkelmann, "Non-invasive nanoscale potentiometry and ballistic transport in epigraphene nanoribbons," *Nano Letters*, 2020.

[93] C.-M. Zetterling, *Process technology for silicon carbide devices*, 2. IET, 2002.